Search for Supersymmetry Using Acoplanar Lepton Pair Events at OPAL

David Futyan

THE UNIVERSITY of MANCHESTER

High Energy Physics Group
Department of Physics and Astronomy

A thesis submitted to The University of Manchester for the degree of Doctor of Philosophy in the Faculty of Science and Engineering

December 22, 1999

Contents

List of Figures

List of Tables

Abstract

A selection of di-lepton events with significant missing transverse momentum has been performed using a total data sample of 237.4 pb^{-1} at e$^+$e$^-$ centre-of-mass energies of 183 GeV and 189 GeV. The observed numbers of events — 78 at 183 GeV and 301 at 189 GeV — are consistent with the numbers expected from Standard Model processes, which arise predominantly from W$^+$W$^-$ production with each W decaying leptonically. This topology is also an experimental signature for the pair production of new particles that decay to a charged lepton accompanied by one or more invisible particles. Discrimination techniques are described that optimize the sensitivity to particular new physics channels. No evidence for new phenomena is apparent and model independent limits are presented on the production cross-section times branching ratio squared for sleptons and for leptonically decaying charginos and charged Higgs. For a 100% branching ratio for the decay $\tilde{\ell}^\pm_R \rightarrow \ell^\pm \tilde{\chi}^0_1$, where $\tilde{\chi}^0_1$ is the lightest neutralino, the following are excluded at 95% CL: right-handed smuons with masses below 82.3 GeV for $m_{\tilde{\mu}^-} - m_{\tilde{\chi}^0_1} > 3$ GeV and right-handed staus with masses below 81.0 GeV for $m_{\tilde{\tau}^-} - m_{\tilde{\chi}^0_1} > 8$ GeV. Right-handed selectrons are excluded at 95% CL for masses below 87.1 GeV for $m_{\tilde{\mathrm{e}}^-} - m_{\tilde{\chi}^0_1} > 5$ GeV, within the framework of the Minimal Supersymmetric Standard Model for $\mu < -100$ GeV and $\tan\beta = 1.5$. Charged Higgs bosons, H$^\pm$, are excluded at 95% CL for masses below 82.8 GeV, for a 100% branching ratio for the decay $\mathrm{H}^\pm \rightarrow \tau^\pm \nu_\tau$.

Declaration

No portion of the work referred to in this thesis has been submitted in support of an application for another degree or qualification of this or any other university or other institute of learning.

The Author

The author was educated at Rydal School, Colwyn Bay before joining the Department of Physics and Astronomy at the University of Manchester. The work presented here was undertaken at Manchester and CERN, Geneva.

Acknowledgements

First and foremost, I would like to thank my supervisor, Terry Wyatt for all his guidance, help and advice over the last three years. Thanks also to Graham Wilson for coming up with so many useful ideas and providing me with so much help and advice while I was at CERN. This thesis owes a lot to both of them. Thanks also to Vakhtang Kartvelishvili for his patient explanations in answer to my theoretical questions, and thanks to PPARC for funding my research.

I would like to thank all my friends both in Manchester and in Geneva for making the last three years of my life so enjoyable, whether in Geneva, 4000m up some mountain, or somewhere in between on a pair of skis.

Finally, a special thankyou goes to my family for all their love and support over the years, and to Helen for providing me with at least seven uses.

Chapter 1

Introduction

The Standard Model of Particle Physics has proved extremely successful in describing all observations made at present day particle accelerators. However, there are strong theoretical reasons for believing that there is physics beyond the Standard Model and that the current theory is simply the low energy approximation of a more fundamental theory. Searches for new physics therefore form an important part of modern particle physics research. This thesis describes a search conducted at the LEP e^+e^- collider at CERN, Geneva, for new physics processes which result in a final state consisting of two oppositely charged leptons plus significant missing transverse momentum. The topology is referred to as an acoplanar di-lepton topology[1]. An example of such an event is shown in figure 1.1.

This experimental topology is produced by a number of Standard Model processes, in particular the pair production of W bosons, $e^+e^- \rightarrow W^+W^-$, in which both W bosons decay leptonically: $W^- \rightarrow \ell^-\overline{\nu}_\ell$. However, by looking for inconsistencies between the experimental data and the Standard Model prediction, both in terms of the numbers of events observed and the properties of those events (e.g. kine-

[1]The acoplanarity of an event is defined as the supplement of the angle between the two lepton candidates in the plane transverse to the beam direction.

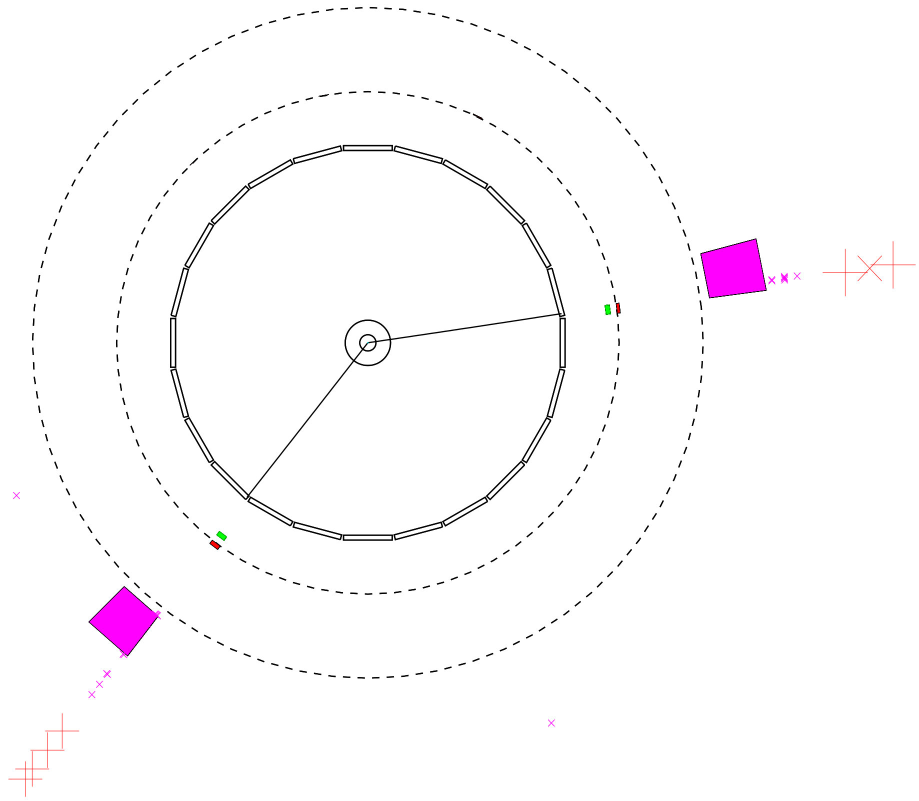

Figure 1.1: *Acoplanar di-lepton candidate at 189 GeV. This event is consistent with* $\mathrm{W}^+\mathrm{W}^-$ *production and (for example) smuon pair production.*

matics, angular distributions, types of leptons), the study of this topology provides a general search for any new physics process giving this experimental signature.

Experimental topologies containing significant missing transverse momentum are of particular interest to new particle searches because this missing momentum signature is one of the most important predicted signatures for the production of supersymmetric particles. Supersymmetry is a strongly theoretically motivated extension to the Standard Model which is generally considered to be an essential component of a truly fundamental theory of high energy physics. Supersymmetry predicts the existence of a supersymmetric partner to every Standard Model particle which differs in spin by $\hbar/2$ to its Standard Model counterpart. In the simplest version of the theory, the Minimal Supersymmetric Standard Model (MSSM), all supersymmetric particles must decay to the lightest supersymmetric particle (LSP), which is predicted to be stable and (for cosmological reasons) weakly interacting. It therefore escapes the detector unseen, thus giving rise to the missing momentum signature.

The structure of this thesis is as follows: The OPAL detector, used to collect the experimental data for the analysis is described in Chapter 2. The Standard Model of particle physics is then introduced in Chapter 3, and the motivation for supersymmetry and the phenomenology of supersymmetry are discussed in Chapter 4. This is followed in Chapter 5 by a brief description of the general selection of acoplanar di-lepton events. The bulk of the work performed by the author is described in Chapters 6, 7 and 8. Chapters 6 and 7 describe the analysis of the selected events with the aim of distinguishing between Standard Model sources of the events and some specific new physics signals. The following new particle decays are searched for:

charged scalar leptons (sleptons): $\tilde{\ell}^{\pm} \to \ell^{\pm}\tilde{\chi}^0_1$ (or $\tilde{\ell}^{\pm} \to \ell^{\pm}\tilde{G}$), where $\tilde{\ell}^{\pm}$ may be a selectron ($\tilde{\mathrm{e}}$), smuon ($\tilde{\mu}$) or stau ($\tilde{\tau}$) and $\ell^{\pm}$ is the corresponding charged lepton. $\tilde{\chi}^0_1$ and $\tilde{G}$ are the lightest neutralino and the gravitino, respectively (see Chapter 4), one of which is expected to be the LSP.

charged Higgs bosons: $\mathrm{H}^{\pm} \to \tau^{\pm}\nu_{\tau}$.

charginos: $\tilde{\chi}^{\pm}_1 \to \ell^{\pm}\tilde{\nu}$ ("2-body" decays) or $\tilde{\chi}^{\pm}_1 \to \ell^{\pm}\nu\tilde{\chi}^0_1$ ("3-body" decays).

The distinction between these new physics signals and the Standard Model background is made by combining the information from a number of discriminating variables to form a "relative likelihood", L_R, whose value tends to be close to one for signal events and close to zero for background events. The search for new physics is then performed by considering the likelihood that the L_R distribution for the observed data is consistent with the expected distribution for background plus a signal with a given cross-section.

The results of the searches in the form of upper limits on the cross-section times branching ratio squared for the production of the new particles, and the excluded masses for the new particles, are presented in Chapter 8.

Chapter 2

The OPAL Detector

2.1 The LEP accelerator

The Large Electron Positron (LEP) Accelerator [1] is the largest particle collider in the world, with a circumference of 26.7 km. It is located in a tunnel at a depth of about 100 m, at the CERN laboratory on the French-Swiss border near Geneva.

Electrons produced by thermionic emission are accelerated to 200 MeV in the LEP Injector Linac (LIL) and directed onto a tungsten target where e^+e^- pairs are produced from bremsstrahlung photons. These are accelerated further to 600 MeV and stored in the Electron Positron Accumulator (EPA), prior to injection into the 200 m diameter Proton Synchrotron (PS). Here the particles are accelerated to 3.5 GeV, before being transfered into the 2.2 km circumference Super Proton Synchrotron (SPS) which accelerates the particles to 22 GeV. Finally, the particles are injected into the LEP accelerator in eight bunches (four electron and four positron), each of which contains about 10^{11} particles, and accelerated to a collision energy of up to about 200 GeV in the centre of mass frame. The electron and positron bunches circulate in opposite directions and are made to collide at the four interaction points where the detectors ALEPH [2], DELPHI [3], L3 [4] and OPAL [5] are located.

The analysis described in this document uses data collected by the OPAL detector in 1997 and 1998.

2.2 The OPAL Detector

The OPAL (Omni-Purpose Apparatus for LEP) detector is a multipurpose apparatus designed to reconstruct efficiently and identify all types of events occurring in e^+e^- collisions. A full description of the detector is given in [5]. The general layout of the detector is shown in figure 2.1. A system of central tracking chambers is contained inside a solenoid which provides a uniform magnetic field of 0.435 T. The solenoidal coil is surrounded by a time-of-flight counter array, a lead glass electromagnetic calorimeter with a presampler, an instrumented magnet return yoke serving as a hadron calorimeter and four outer layers of muon chambers. The most important parts of the detector for the acoplanar di-lepton analysis are the central tracking chamber and the electromagnetic calorimeter as they are crucial for the identification of electrons and muons.

The coordinate system used in OPAL is a right-handed Cartesian system with the origin at the nominal interaction point. The z axis is along the electron beam direction. The x axis is horizontal and directed towards the centre of the LEP ring. The y axis is slightly away from the vertical as the LEP ring is slightly inclined. Cylindrical polar coordinates (r, θ, ϕ) are also used.

2.2.1 The Central Tracking System

The central tracking system consists of a Silicon Microvertex detector and three drift chamber devices: a precision vertex detector, a large volume jet chamber, and Z-chambers, situated inside a pressure vessel holding a pressure of 4 bar.

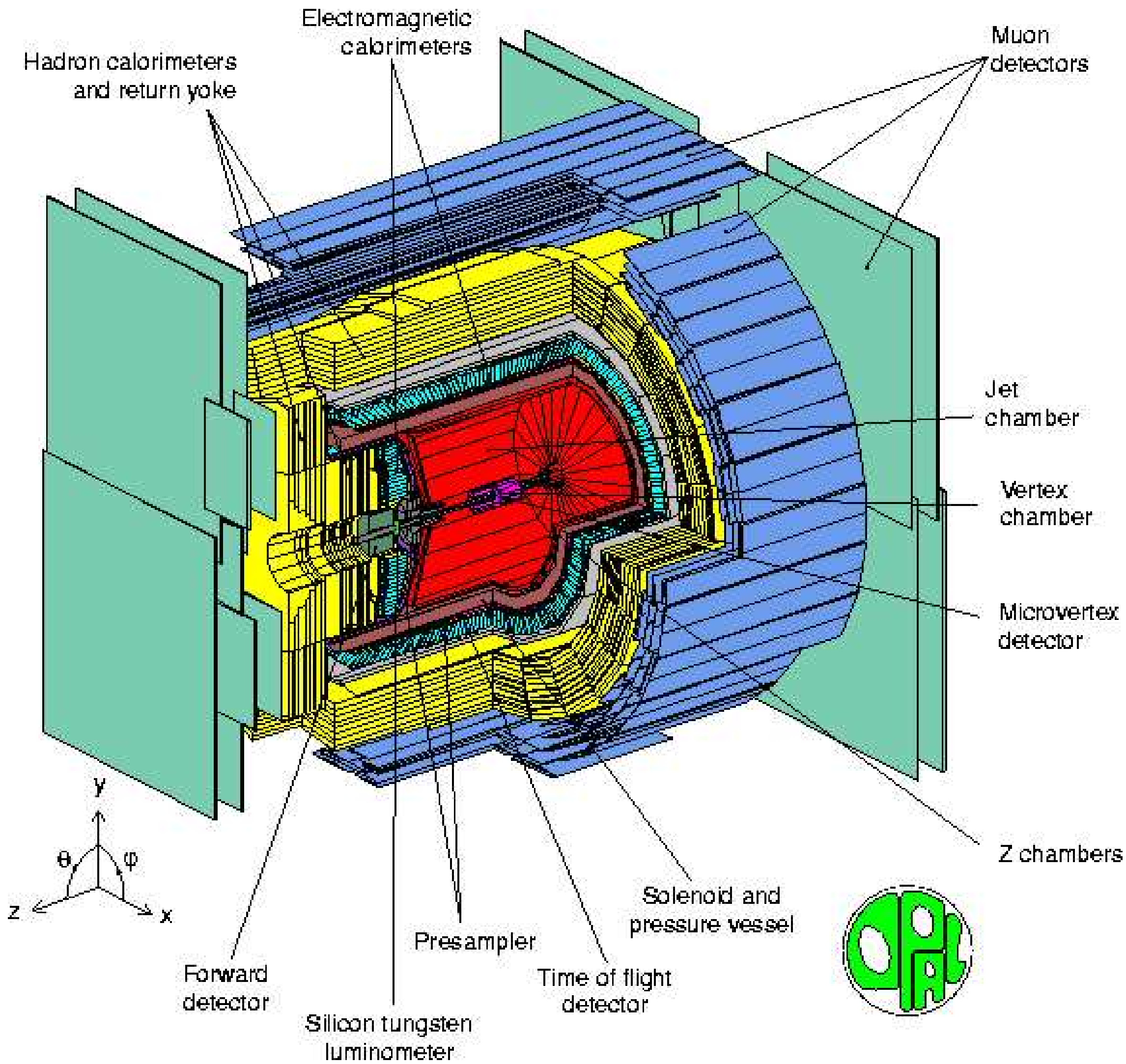

Figure 2.1: *A cut away diagram of the OPAL detector*

The Silicon Microvertex Detector

The Silicon Microvertex Detector (SI) [6] consists of two barrels of Silicon Microstrip Detectors at radii of 6 and 7.5 cm. Each layer consists of 18cm long ladders made up of 5 pairs of single sided silicon wafers, with readout strips at 50 μm pitch. Each pair of wafers consists of an $r-\phi$ wafer and an $r-z$ wafer, glued back to back. The inner and outer layers consist of 12 and 15 ladders, respectively. The high spatial resolution allows SI to locate decay vertices of short lived particles, in particular

B-mesons.

The Vertex Detector

The vertex detector (CV) is a 1 m long, cylindrical high resolution drift chamber of radius 23.5 cm. It is divided into two layers. The inner layer, lying between r=8.8 cm and r=17.5 cm, consists of 36 axial cells each containing 12 wires with a spacing of 0.583 cm, strung parallel to the beam direction. The outer layer lies between r=17.5 cm and r=23.5 cm and consists of 36 stereo cells each containing 6 wires with a spacing of 0.5 cm, inclined at an angle of 4° to the beam direction. The axial cells provide a precise measurement of the position in the $r - \phi$ plane ($\sigma = 50$ μm). The combination of the information from the axial and stereo cells provides a good z measurement ($\sigma_z \approx 700 \mu m$) for charged particles close to the interaction region.

The Jet Chamber

The jet chamber (CJ) has an inner radius of 25 cm and an outer radius of 185 cm. It is subdivided into 24 identical sectors, each containing 159 sense wires, strung parallel to the beam direction in a radial plane. The wires in each plane are staggered by ± 100 μm in order to resolve the left-right ambiguities. The cathode wires form the boundaries between the sectors. The maximum drift distance varies from 3 cm at the innermost sense wire to 25 cm at the outermost wire. In the region $|\cos\theta| > 0.73$, 159 points are measured along each track and at least 8 points on a track are obtained over a solid angle of 98% of 4π. For each point the coordinates in the $r - \phi$ plane are determined from the measurement drift time, and the z coordinate is determined from the charge measurement at each end of the wires. The summation of the charges received at each end allows the energy loss, $\mathrm{d}E/\mathrm{d}x$ of the particle in the chamber gas to be measured. The average spatial resolution in $r - \phi$ is 135 μm at the mean drift distance of 7 cm, but varying between 120 and 250 μm for other drift distances. The average resolution in z is 6 cm. The transverse momentum with respect to the beam axis, p_{T}, is measured with resolution $\sigma_{p_{\mathrm{T}}}/p_{\mathrm{T}} = \sqrt{(0.02)^2 + 0.0015 p_{\mathrm{T}})^2}$ where p_{T} is measured in GeV.

The Z-Chambers

The Z-chambers (CZ) provide a precise measurement of the z coordinate of tracks as they leave the jet chamber. They consist of a cylindrical layer of 24 drift chambers 400 cm long, 50 cm wide and 5.9 cm thick covering 94% of the azimuthal angle and the polar angle range $|\cos\theta| > 0.72$. Each chamber is divided in z into 8 cells of 50 cm $\times$ 50 cm so that the maximum drift distance is 25 cm in the z direction. Each cell contains 6 sense wires with a 4 mm radial spacing, and a stagger of ± 250 μm to resolve the left-right ambiguity. The z resolution is approximately 300 μm. The ϕ coordinate is determined by charge division.

2.2.2 The Time-of-flight system

The Time-of-flight (TB) system consists of 160 scintillation counters forming a barrel 684 cm long with mean radius 236 cm, positioned outside the magnet coil, covering the region $|\cos\theta| > 0.82$. It generates trigger signals, and by measuring the time of flight from the interaction region, provides charged particle identification in the range 0.6 to 2.5 GeV and an effective rejection of cosmic rays. The time resolution is approximately 350 ps.

In 1996 the Tile Endcap (TE) system was added to enhance the triggering information available in the forward region. It consists of a 10 mm thick scintillator layer divided into tiles and situated between the endcap presampler and the endcap electromagnetic calorimeter.

2.2.3 Electromagnetic Calorimetry

The electromagnetic calorimeter detects and measures the energies and positions of electrons, positrons and photons ranging from tens of MeV to 100 GeV. It is positioned between the coil and the iron yoke of the magnet and consists of three large overlapping assemblies of lead glass blocks (the barrel (EB) and two endcaps (EE)), together covering 98% of the solid angle.

There are approximately two radiation lengths of material in front of the calorimeter, (mostly due to the coil and the central detector pressure vessel), resulting in the majority of electromagnetic showers being initiated before the lead glass. Presampling devices are therefore installed immediately in front of the lead glass to measure the positions and energies of these showers. However, due to reliability problems, the presampler is in general not used in OPAL analyses and indeed is not used in this analysis.

Complete electromagnetic hermetic coverage is of crucial importance for the identification of the missing transverse momentum signature. The forward and silicon tungsten detectors extend the angular coverage provided by the lead glass calorimeter down to θ=25 mrad.

The Lead Glass Calorimeter

The barrel lead glass calorimeter consists of a 662 cm long cylindrical array of 9440 lead glass blocks located at a radius of 246 cm, covering the region $|\cos\theta| > 0.81$. The longitudinal axes of the blocks point towards the interaction region to minimize the probability of a particle traversing more than one block, but the blocks are tilted slightly from a perfectly pointing geometry to prevent particles escaping through the gaps between them. Each block is $\sim$ 10×10 cm in cross section and 37 cm in depth, corresponding to 24.6 radiation lengths. High energy electrons and photons interact in the lead glass through bremsstrahlung and pair creation, respectively, to produce electromagnetic showers. The number of secondary electrons produced in a shower is proportional to the incident energy. The Cherenkov light from the secondary electrons is detected by 3 inch diameter magnetic field tolerant phototubes at the base of each block. Test beam studies have shown that the typical energy resolution without any material in front of the calorimeter is $\sigma_E/E = 0.2\% + 6.3\%/\sqrt{E}$, where E is the electromagnetic energy in GeV. This resolution is degraded by a factor $\sim$2 by the 2.08 radiation lengths in front of the calorimeter. The spatial resolution is $\sim$1 cm for electromagnetic showers.

The endcap lead glass calorimeter consists of two dome-shaped arrays of 1132 blocks, covering all ϕ and the polar angle range $0.81 < |\cos\theta| < 0.98$. As opposed to the barrel calorimeter, the endcap blocks are mounted coaxial to the beam line due to tight geometrical constraints. The blocks come in three lengths (38, 42 and 52 cm), and typically provide 22 radiation lengths of material. The blocks are read out using Vacuum Photo Triodes (VPTs) which are single stage multipliers capable of operating in the full axial field of the magnet. The energy resolution is $\sigma_E/E = 5\%/\sqrt{E}$ at low energy.

The Forward Detector

The forward detector (FD) consists of two calorimeters located between 2 m and 3 m on either side of the interaction point. Each calorimeter consists of 35 sampling layers of lead-scintillator sandwich divided into a presampler of 4 radiation lengths and the main calorimeter of 20 radiation lengths. Three layers of proportional tube chambers are located between the presampler and the main calorimeter, which give the position of a shower centroid to an accuracy of 0.3 cm.

The gap in calorimetric acceptance between FD and EE (142 to 200 mrad) is plugged by the gamma catcher, a ring of lead-scintillator sandwich modules 7 radiation lengths thick.

There is also a far forward luminosity monitor, used to detect electrons deflected in the range 5 to 10 mrad by the LEP quadrupoles. These are small lead-scintillator modules, 20 radiation lengths thick, mounted on either side of the beam pipe 7.85 m from the interaction region.

The Silicon Tungsten Detector

The silicon tungsten detector (SW) was installed in 1993. As is the case for the forward detector, its principal design purpose is to detect low angle Bhabha events in order to measure luminosity. It covers the angular range 25 mrad to 59 mrad and consists of two calorimeters situated 240 cm on either side of the interaction point. Each calorimeter consists of 19 layers of silicon detectors and 18 layers of tungsten. The first layer of silicon detects preshowering. The next 14 layers are behind one radiation length plates of tungsten and the final 4 layers are behind two radiation length plates of tungsten. Each layer of silicon consists of 16 wedge shaped detectors forming a ring between r=6.2 cm and r=14.2 cm. Each wedge is divided into 64 pads which can be read out individually.

2.2.4 The Hadron Calorimeter

The hadron calorimeter is designed to measure the energy of hadrons emerging from the electromagnetic calorimeter and to assist with the identification of muons. It covers a solid angle of 97% of 4π and is divided into three sections: the barrel (HB) covers $|\cos\theta| > 0.81$, the endcaps (HE) cover $0.81 < |\cos\theta| < 0.91$ and the pole tips (HP) extend the coverage to $|\cos\theta| > 0.99$.

The barrel and endcap calorimeters consist of the iron of the magnet return yoke, which is segmented into layers 10 cm thick, between which planes of detectors are positioned. The barrel consists of 9 layers of chambers alternating with 8 iron slabs, between r=339 cm and r=439 cm. The toroidal endcaps consist of 8 layers of chambers and 7 layers of iron. The chambers are limited streamer tube devices strung with anode wires 1 cm apart. The energy of hadronic showers is estimated using the sum of the signals from pads located on the outer surfaces of each chamber, which divide the calorimeter into 48 bins in ϕ and 21 bins in θ. Hits on 0.4 cm wide aluminium strips located on the inner surface of each chamber, running parallel to the anode wires, provide muon tracking information.

The pole tip calorimeters consist of ten 8 cm thick layers of iron sandwiching multiwire proportional chambers, giving improved energy resolution in the forward direction where the momentum resolution from the central detector is falling off.

2.2.5 The Muon Detector

Particles incident on the muon detector have traversed the equivalent of 1.3 m of iron. The probability of a pion not interacting in this material (corresponding to seven interaction lengths) is less than 0.001, so in general only muons reach this outermost detector. The detector is divided into the barrel, which covers $|\cos\theta| > 0.68$ with four layers of chambers and $|\cos\theta| > 0.72$ with at least one layer, and the endcaps, which cover $0.67 < |\cos\theta| < 0.98$. 7% of the total solid angle is not covered due to the beam pipe (see MIP plug, section 2.2.6), support legs and cables.

The barrel muon detector (MB) consists of 110 large area drift chambers. The chambers are 120 cm wide and 9 cm thick and come in three possible lengths (10.4 m, 8.4 m and 6 m), the shorter ones being needed to fit between the magnet support legs. Each chamber is split into two adjoining cells, each containing an anode signal wire running the full length of the cell, parallel to the beam line. The drift field is defined by 0.75 cm wide cathode strips etched onto the inner surfaces of each cell. The spatial position in the ϕ plane is determined from the drift time onto the anode with an accuracy of better than 0.15 cm.

The z coordinate is determined by combining the information from three measurements. The fine z measurement uses induced signals on diamond shaped cathode pads etched onto the inner surfaces of the cells opposite the anode wire. These pads have a repeat distance of 17.1 cm and determine the z coordinate to 2 mm, but modulo 17.1 cm. This ambiguity is reduced by factor 10 by the analogous medium z measurement, which uses pads with a repeat distance of 171 cm, and is resolved by the coarse z measurement, obtained from the time and pulse height differences at the two ends of the wire.

The endcap muon detector (ME) consists of two layers of chambers in the plane perpendicular to the beam direction, divided into four quadrants, each of size 6 m $\times$ 6 m. Two double layered patch chambers fill in the gaps above and below the beam pipe. Each layer of chambers contains two planes of limited streamer tubes, one plane having horizontal wires and the other vertical wires. The streamers produced in the tubes by the passage of a charged particle are detected by the charge induced on planes of 0.8 cm wide aluminium strips, located on either side of each plane of tubes, parallel to the tubes on one side and perpendicular on the other. The parallel strips measure the streamer position to an accuracy of around 3 mm, and by using a weighted average of the recorded pulse heights on adjacent strips, the perpendicular strips measure the position to an accuracy to around 1 mm.

2.2.6 The Minimum Ionizing Particle (MIP) plug

The MIP plug [7] was installed in 1997 to detect minimum ionizing particles such as muons at low angle (45 to 160 mrad), filling the gap in MIP acceptance between ME/HP and SW. This sub-detector is important in the analysis for vetoing $e^+e^-\mu^+\mu^-$ events as described in Section 5.4.1. It consists of four layers of 1 cm thick scintillator tiles located at each end of the detector. The first two layers are situated immediately behind the gamma catcher and are separated from each other by 5 mm of lead which reduces the background from synchrotron radiation. The tiles are divided into quadrants in ϕ and cover the polar angular range 126 to 220 mrad. The third layer, located just behind these is also divided into quadrants and covers the region 45 to 160 mrad. The fourth layer is situated between the SW and FD subdetectors. This layer is divided into octants and covers the angular range 43 to 130 mrad.

2.3 The Trigger, Event Reconstruction and Detector Simulation

2.3.1 The OPAL Trigger

When LEP is operating with four electron bunches and four positron bunches, the bunch crossing frequency is about 45 kHz (22 μs between crossings). The trigger [8] identifies the small fraction of bunch crossings in which an interaction has occurred so that it can decide whether or not to read out and store an event, a process which takes about 20 ms. It is designed to reject non-physics events such as cosmic rays and interactions with the beam pipe. The trigger makes its decision by combining signals from the subdetectors. There are two types of trigger signal which are analysed in parallel. The first type are 'stand-alone' signals such as high track multiplicities and energy sums. Secondly, the full solid angle is divided into 144 overlapping bins (6 bins in θ and 24 bins in ϕ), and the trigger looks for correlations in space for lower threshold signals from the different subdetectors.

2.3.2 Event Reconstruction

When a beam crossing is selected by the trigger as containing a good physics event, each subdetector is read out into its local system crate. The subevent structures from the different subdetectors are then assembled by the event builder. The complete events are then passed to the filter, which performs a low level analysis of the events, classifying them, before the data are compressed and written to disk.

The events are then passed on to ROPE [9] (Reconstruction of OPAL events), a piece of software which converts the data into fully reconstructed events, by reconstructing the tracks and calorimeter clusters in each subdetector. This is done when the subdetector calibration constants are available, usually within one hour of the event being recorded. Finally, the information is stored on Data Summary Tapes (DST) ready for analysis.

2.3.3 Event Simulation

The analysis described in this thesis relies heavily upon Monte Carlo simulations of Standard Model and potential new physics signal events. For a given physics process, a Monte Carlo event generator is used to simulate events by creating a list of the particles produced in an interaction and their decay products, together with the four-vectors associated with each particle. The four-vectors are then processed through GOPAL [10], a piece of software based on the GEANT3 [11] modeling package, which provides a full simulation of the OPAL detector. GOPAL models the output of each subdetector by tracking the passage of each particle though the detector, taking into account the probability of interaction at each point, noise, resolution, etc. The output of the simulation is in the same form as the real data, so that the same event reconstruction software, ROPE, can be used.

Chapter 3

The Standard Model

3.1 The Fundamental Particles and their interactions

The Standard Model [12] forms the theoretical framework on which modern particle physics is based. It is a gauge theory based on the gauge group $SU(3) \otimes SU(2) \otimes U(1)$. Up to now, this theory has proved to be very successful in providing a description of the interactions of the fundamental particles which is in excellent agreement with experiment.

Experiment has observed that the universe is made up of a set of 12 fundamental spin-$\frac{1}{2}$ fermions whose interactions with each other are mediated by a set of gauge bosons, in a manner described by the Standard Model. In addition, each matter particle has a corresponding anti-particle, which has the values of all internal quantum numbers such as charge reversed but is otherwise identical to its matter counterpart.

The fundamental fermions can interact in four possible ways. The strong interaction couples to those particles which carry colour charge, a quantum number which has three possible values (red, green or blue). This divides the fermions into two categories: 6 quarks, which carry colour charge, and 6 leptons which are colour neutral. The strong interaction is mediated by 8 gluons which themselves carry colour charge, and is described by the theory of Quantum Chromodynamics (QCD) (section 3.3). The electromagnetic interaction couples to particles which carry electric charge (all the quarks and three of the leptons). It is mediated by the photon and is described to a very high level of accuracy by the theory of Quantum Electrodynamics (QED). The weak interaction couples to all particles and is mediated by the $W^{\pm}$ and Z^{0} bosons. It has been shown by Glashow, Salam and Weinberg that the weak interaction and the electromagnetic interaction are different aspects of a single interaction, described by the the electroweak theory (section 3.2). The fourth interaction is the gravitational interaction, mediated by the as yet hypothetical graviton. This interaction is negligible on the microscopic scales considered in particle physics and is not described by the Standard Model.

The quarks and leptons are observed to exist in three generations with a lepton doublet and a quark doublet in each generation. Only the first generation fermions are stable. The other generations contain particles which are unstable and more massive, but apart from the internal quantum numbers that define them, they are otherwise almost identical to the first generation particles. The Standard Model makes no prediction about the number of generations but experiment has ruled out any further generations containing light fermions.

3.2 The Electroweak Sector

The electroweak theory is a gauge theory based on the group $SU(2) \otimes U(1)$ which describes the electromagnetic and weak interactions of the fundamental particles.

In this theory, the left-handed fermions form $SU(2)$ isospin doublets and the right-handed fermions form isospin singlets. This difference in the treatment of left and right-handed fermions is needed in order to accommodate the empirical fact that the weak interaction is parity violating. The three generations of leptonic final states can be written as

$$\begin{array}{lcccccc} & & & & & \text{electric charge} & \text{weak isospin} \\ \psi_1(x) = & \begin{pmatrix} \nu_{\rm e} \\ {\rm e} \end{pmatrix}_L, & \begin{pmatrix} \nu_\mu \\ \mu \end{pmatrix}_L, & \begin{pmatrix} \nu_\tau \\ \tau \end{pmatrix}_L & & \begin{array}{c} 0 \\ -1 \end{array} & \begin{array}{c} \frac{1}{2} \\ -\frac{1}{2} \end{array} \\ \psi_2(x) = & {\rm e}_R, & \mu_R, & \tau_R & & -1 & 0 \end{array}$$

Similarly, the quark states are given by

$$\begin{array}{lcccccc} & & & & & \text{electric charge} & \text{weak isospin} \\ \psi_1(x) = & \begin{pmatrix} u \\ d' \end{pmatrix}_L, & \begin{pmatrix} c \\ s' \end{pmatrix}_L, & \begin{pmatrix} t \\ b' \end{pmatrix}_L & & \begin{array}{c} +\frac{2}{3} \\ -\frac{1}{3} \end{array} & \begin{array}{c} \frac{1}{2} \\ -\frac{1}{2} \end{array} \\ \psi_2(x) = & u_R, & c_R, & t_R & & +\frac{2}{3} & 0 \\ \psi_3(x) = & d'_R, & s'_R, & b'_R & & -\frac{1}{3} & 0 \end{array}$$

For quarks, the electroweak eigenstates are not the same as the mass eigenstates. The quark states d', s' and b' shown above are linear combinations of the physically observed states d, s and b, given by the Cabibbo-Kobayashi-Maskawa matrix:

$$\begin{pmatrix} d' \\ s' \\ b' \end{pmatrix} = \begin{pmatrix} V_{ud} & V_{us} & V_{ub} \\ V_{cd} & V_{cs} & V_{cb} \\ V_{td} & V_{ts} & V_{tb} \end{pmatrix} \begin{pmatrix} d \\ s \\ b \end{pmatrix} \tag{3.1}$$

The matrix is almost diagonal but the fact that the off diagonal elements are non-zero allows mixing between the quark generations. This in turn allows b and s quarks, which would otherwise be stable, to decay.

3.2.1 The Gauge Bosons

In quantum field theories the propagation and interaction of the fermion fields are described by a Lagrangian density (referred to subsequently simply as the Lagrangian) which satisfies the Euler-Lagrange equation of motion:

$$\partial_\mu \left(\frac{\partial \mathcal{L}}{\partial(\partial_\mu \psi)} \right) = \frac{\partial \mathcal{L}}{\partial \psi} \tag{3.2}$$

The relativistic wave equation for the field is obtained by substituting the Lagrangian into Equation 3.2. For example, substitution of the Lagrangian for a free fermion field, $\mathcal{L} = \bar{\psi}(i\partial\gamma_\mu - m)\psi$, where m is the mass of the field, into Equation 3.2 gives the Dirac equation.

The interactions of the Standard Model can be described by requiring the Lagrangian to be invariant under global and local phase transformations of the fermion fields referred to as gauge transformations. This requirement is implemented by observing gauge transformations under which the Lagrangian is not invariant, and introducing new "gauge fields" into the Lagrangian which have transformation properties such that the invariance is restored. It is seen that these fields correspond to the gauge bosons.

The transformation of the left-handed fermion doublet fields under $SU(2)_L \otimes U(1)_Y$ can be written

$$\psi_L(x) \to \psi'_L(x) = e^{i\boldsymbol{\alpha}(x).\boldsymbol{\sigma}} e^{i\beta(x)Y} \psi_L(x) \tag{3.3}$$

where the operators $\boldsymbol{\sigma}$ and Y are the generators of the gauge groups $SU(2)_L$ and $U(1)_Y$ respectively: $\boldsymbol{\sigma}$ are the Pauli spin matrices and Y is the fermion hypercharge, defined by $Q = I_3 + Y/2$ where Q is the charge and I_3 the third component of the weak isospin. The vector function $\boldsymbol{\alpha}$ and the scalar function β are arbitrary real functions defining the transformation. They are functions of position, and the transformation is therefore local.

The singlets transform under $U(1)_Y$ only:

$$\psi_R(x) \rightarrow \psi'_R(x) = e^{i\beta(x)Y}\psi_R(x) \tag{3.4}$$

The free fermion Lagrangian is not gauge invariant under the $SU(2)_L \otimes U(1)_Y$ transformation. Four fields must be introduced into the Lagrangian in order to make it gauge invariant: $W^1_\mu, W^2_\mu, W^3_\mu$, which couple to the weak isospin, and B_μ, which couples to the weak hypercharge. The observable fields corresponding to the vector bosons of the electroweak interaction are linear combinations of these fields. The fields of the $\mathrm{W}^\pm$ bosons are:

$$\mathrm{W}^\pm = \frac{1}{\sqrt{2}}(W^1_\mu \mp iW^2_\mu) \tag{3.5}$$

The fields of the γ and Z^0 bosons are mixed states of the W^3_μ and B_μ fields:

$$\begin{pmatrix} A_\mu \\ Z_\mu \end{pmatrix} = \begin{pmatrix} \cos\theta_W & \sin\theta_W \\ -\sin\theta_W & \cos\theta_W \end{pmatrix} \begin{pmatrix} B_\mu \\ W^3_\mu \end{pmatrix} \tag{3.6}$$

where θ_W is the weak mixing angle, a free parameter of the Standard Model which determines the relative strengths of the electromagnetic and weak interactions.

3.3 Quantum Chromodynamics

Quantum Chromodynamics (QCD) is a gauge theory based on the group $SU(3)$ which describes the strong interaction experienced by the quarks. The generators of this group are any set of 8 linearly independent traceless hermitian 3×3 matrices. The structure of QCD is inferred by requiring the free quark Lagrangian to be invariant under the phase transformations of this group, of the form

$$q(x) \to q'(x) = e^{i\alpha_a(x)T_a} q(x) \tag{3.7}$$

where $q(x)$ represents the quark colour field, T_a are the 8 generator matrices of the $SU(3)$ group and $\alpha_a(x)$ are the group parameters. A summation over the repeated index a is implied.

Gauge invariance under these transformations is restored by introducing 8 gauge fields corresponding to the 8 gluons which mediate the strong interaction. The gauge invariance only holds if a further term is added to the Lagrangian which corresponds to a self interaction between the gauge bosons, and therefore the existence of triple and quadruple gluon vertices.

The strength of the strong interaction is determined by the value of the strong coupling constant, $\alpha_s(Q^2)$, which decreases with the square of the characteristic momentum transfer, Q^2, of the interaction. As the separation between two quarks increases, (decreasing Q^2), α_s becomes large and eventually, the potential energy stored in the colour field between the quarks becomes large enough to create a new $\mathrm{q\bar{q}}$ pair. Thus quarks can never exist in isolation but only in colour neutral bound states of type $\mathrm{q\bar{q}}$ (mesons) or qqq (baryons), collectively known as hadrons. QCD calculations using perturbation theory become inapplicable at large α_s, as complex higher order diagrams become important. For this reason, the formation of hadronic jets in the decays of particles produced in $\mathrm{e^+e^-}$ collisions can only be modeled empirically.

3.4 The Higgs Mechanism

Together, the electroweak theory and QCD describe all the interactions of the Standard Model. However, the question of fermion and gauge boson masses still needs to be addressed. If mass terms are added to the Lagrangian, then it is no longer invariant under the $SU(2)_L \otimes U(1)_Y$ gauge transformations. Such a theory is not renormalisable and therefore cannot make predictions above first order. It is possible however to construct a theory of interacting massive particles which is gauge invariant and renormalisable by using spontaneous symmetry breaking.

If a complex scalar field $\phi(x) = 1/\sqrt{2}(\phi_1 + i\phi_2)$ is introduced into the theory, new kinetic and potential terms will appear:

$$\mathcal{L} = (\partial_\mu \phi)(\partial^\mu \phi^*) - V(\phi, \phi^*) \tag{3.8}$$

Consider a potential of the form

$$V(\phi, \phi^*) = \mu^2 \phi\phi^* + \frac{1}{4}\lambda(\phi\phi^*)^2 \tag{3.9}$$

with $\mu^2 < 0$ and $\lambda > 0$. The potential has the form shown in figure 3.1. Rather than having a unique minimum at $|\phi| = 0$, this potential has an infinite set of minima lying on a circle of radius $\nu = |\phi|^2 = -2\mu^2/\lambda$. The ground state, which corresponds to the minimum of the potential, is therefore not unique. Because all of the possible degenerate states are related to one another by a $U(1)$ gauge transformation, gauge invariance allows the ground state to be arbitrarily chosen, without loss of generality, to be at any point on the circle. The chosen ground state no longer has the symmetry of the Lagrangian, and the symmetry is said to be spontaneously broken.

As perturbative calculations are calculated around the ground state, the field $\phi(x)$ should be translated to a minimum point, which can be chosen to be at $\phi_1 = \nu, \phi_2 = 0$. This is done by re-writing $\phi(x)$ in terms of $\theta_1 = \phi_1 - \nu$ and $\theta_2 = \phi_2$:

$$\phi(x) = \frac{1}{\sqrt{2}}(\nu + \theta_1 + i\theta_2) \tag{3.10}$$

If this expression for $\phi(x)$ is inserted into equation 3.8, a mass term $-\mu^2\theta_1^2$

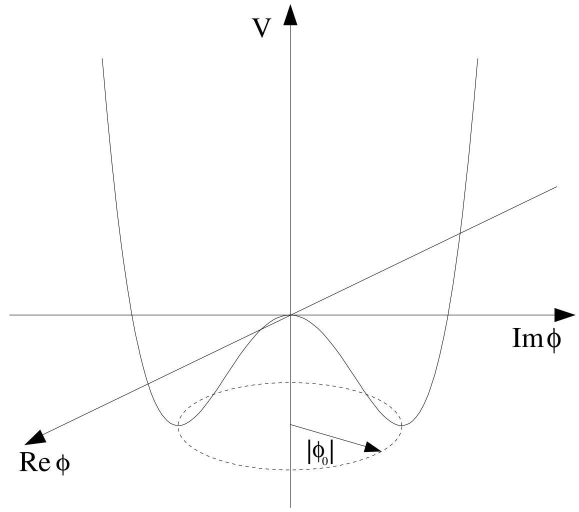

Figure 3.1: *The potential* $V(\phi, \phi^*)$.

appears, implying that the θ_1 field corresponds to a boson with mass $\sqrt{-2\mu^2}$. The other field corresponds to a massless "Goldstone boson".

This illustrates the spontaneous symmetry breaking of a $U(1)$ gauge symmetry. In order to generate masses for the $W^{\pm}$ and Z^0 bosons whilst keeping the photon massless, the form of $\phi(x)$ must be chosen to be an $SU(2)_L$ doublet of complex scalar fields:

$$\phi(x) = \frac{1}{\sqrt{2}} \begin{pmatrix} \phi_1 + i\phi_2 \\ \phi_3 + i\phi_4 \end{pmatrix} \tag{3.11}$$

The ground state is chosen to be at $\phi_1 = \phi_2 = \phi_4 = 0, \phi_3 = \nu$, and the resulting Lagrangian contains one massive scalar field (the Higgs boson), and three unphysical Goldstone bosons, which are absorbed as extra degrees of freedom by the $W^{\pm}$ and Z^0 bosons, which gain masses [12].

The Higgs boson is the only particle in the Standard Model yet to be observed. The lower limit on its mass at 95% CL is currently set at 95.2 GeV [13].

Chapter 4

The Minimal Supersymmetric Standard Model (MSSM)

4.1 The Need for Physics Beyond the Standard Model

The Standard Model provides an extremely successful description of all particle physics phenomena accessible to present day accelerators. However, although there is not yet any experimental evidence, there are strong theoretical reasons for believing that there is physics beyond the Standard Model and that the current theory is simply the low energy approximation of a more fundamental theory.

The Standard Model is not a complete theory. It contains at least 19 arbitrary parameters [14]. It also contains unanswered questions such as why the left-handed fermions are in $SU(2)$ doublets and the right-handed ones in singlets, why the fermions come in three generations, why the quarks come in three colours, and why electric charge is quantized the way it is. Recent results [15] from the Super-Kamiokande experiment have been interpreted as evidence for neutrino mixing, which is not described by Standard Model physics. Also, astronomical observations have shown conclusively that the majority of matter in the universe is in the form of non-baryonic "dark matter", which in order to explain large scale structure formation in the universe must consist mostly of stable weakly interacting massive particles (WIMPS) with masses of order 10 to 1000 GeV [16].

Significantly, the Standard Model does not incorporate gravity. Clearly a new framework will be required at the Planck scale, where quantum gravitational effects become important ($M_{Planck} = \sqrt{\hbar c^5/G} = 1.22 \times 10^{19}$ GeV), and it seems unreasonable to assume that there is no other new physics in the 16 orders of magnitude in energy between current accelerator energies and the Planck scale.

In addition to these considerations, there is an important technical problem that arises in any quantum field theory that contains elementary spin zero fields. Consider the one-loop quantum corrections to the mass of the Higgs boson (a spin zero field) due to the loops diagrams shown in figure 4.1. Each diagram is quadratically divergent, giving corrections to the Higgs mass squared of [14, 17, 18]

$$\delta m_{\mathrm{H}}^2 = \mathcal{O}\left(\frac{g^2}{16\pi^2}\right) \int^{\Lambda} d^4k \frac{1}{k^2} = \mathcal{O}\left(\frac{\alpha}{\pi}\right) \Lambda^2 \tag{4.1}$$

where g is a dimensionless coupling constant and Λ represents the scale up to which the Standard Model remains valid, and beyond which new physics sets in. Since we know from the measured masses of the gauge bosons that the vacuum expectation value of the Higgs field is $2M_{\mathrm{W}}/g = 246$ GeV, it must be that m_{H}^2 is of order $(100\text{ GeV})^2$. However, if Λ is taken to be the Planck scale, then the Higgs mass receives enormous quantum corrections from every particle coupling to the Higgs field, such that m_{H}^2 becomes some 30 orders of magnitude larger than this [17, 18]. This is only a problem for the Higgs boson because quantum corrections to the fermions and gauge bosons have logarithmic rather than quadratic sensitivity to Λ.

This problem can be solved because the theory is renormalisable. This means that it is possible to insert counter terms into the Standard Model Lagrangian which

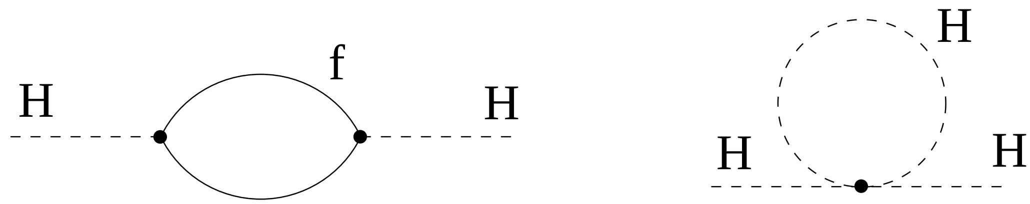

Figure 4.1: *One-loop quantum corrections to m_{H}^2 in the Standard Model.*

cancel the divergent terms. However, the coefficients in the counter terms must be fine tuned to one part in $\sim 10^{30}$ in order for this cancellation to succeed, and this must be achieved for every order of perturbation theory separately. This is referred to as the "naturalness" problem. The related problem of the Higgs mass being much lower than the Planck mass is referred to as the "hierarchy" problem. If it is required as a matter of principle that the theory should not require this incredible fine tuning of parameters, it can be concluded that Λ should be less than $\sim$1 TeV, and therefore that there is new physics below or around the TeV scale.

4.2 Supersymmetry

It is clear from chapter 3 that the role of symmetry in nature is one of fundamental importance. The symmetries observed in nature come in two types. There are symmetries that are internal to the S-matrix, whose generators commute with the Lorentz generators, such as the gauge symmetries $SU(3), SU(2)$ and $U(1)$, and global symmetries such as baryon and lepton number conservation. In addition there is the Lorentz symmetry, which is a space-time symmetry and is therefore external. There is a theorem [19] which states that there is only one possible external symmetry of the S-matrix, beyond the Lorentz symmetry, for which the S-matrix is non-trivial. That symmetry is supersymmetry.

Supersymmetry [20,21] is the extension of the Lorentz symmetry by the addition of a spinorial generator $Q_\alpha (\alpha = 1, 2)$. In the same way that the σ generators of the

$SU(2)_L$ symmetry generate transformations in isospin space, the supersymmetry generator Q_α generates transformations in spin space. Q_α is a 2-component Weyl-spinor which transforms bosons into fermions and vice versa. It therefore carries spin angular momentum 1/2, and the symmetry must therefore be a space-time symmetry with non-trivial algebra with the Lorentz group [17–20]:

$$[P^\mu, Q_\alpha] = 0 \tag{4.2}$$

$$[M^{\mu\nu}, Q_\alpha] = -i(\sigma^{\mu\nu})_\alpha^\beta Q_\beta \tag{4.3}$$

$$\{Q_\alpha, Q_\beta\} = \{Q^\dagger_{\dot\alpha}, Q^\dagger_{\dot\beta}\} = 0 \tag{4.4}$$

$$\{Q_\alpha, Q^\dagger_{\dot\beta}\} = 2\sigma^\mu_{\alpha\dot\beta} P_\mu \tag{4.5}$$

Here $\sigma^{\mu\nu} = 1/4(\sigma^\mu\sigma^{\nu\dagger} - \sigma^\nu\sigma^{\mu\dagger})$, where $\sigma^\mu = (\mathbf{1},\boldsymbol{\sigma})$ and $\sigma^{\mu\dagger} = (\mathbf{1}, -\boldsymbol{\sigma})$, where $\boldsymbol{\sigma}$ are the Pauli matrices. P^μ is the energy-momentum tensor and $M^{\mu\nu}$ is the angular momentum tensor.

It can be shown using the above algebra that Q_α is a raising operator in spin space and $Q^\dagger_{\dot\beta}$ is a lowering operator. The existence of such operators means every Standard Model particle has a corresponding supersymmetric partner which differs in spin by $\hbar/2$, with other internal quantum numbers identical, in the same way that every left-handed fermion has an isospin partner.

The names of the superpartners are constructed by prefixing an "s" (short for scalar) for the partners of the fermions, e.g. selectron, and appending "ino" for the partners of the bosons, e.g. photino. All sfermions are scalar and all gauginos and higgsinos have spin $\frac{1}{2}$, except the gravitino[1] which has spin $\frac{3}{2}$.

From equation 4.2 we have $[P.P, Q_\alpha] = 0$ and thus $[M^2, Q_\alpha] = 0$, where M is the mass of the field. Thus if supersymmetry is an exact symmetry, the superpartners should have the same masses as their Standard Model counterparts. Since this

[1]The gravitino is the supersymmetric partner of the graviton, a particle with spin 2 which must exist in a locally supersymmetric theory of particle physics [22].

is clearly not the case, as none of the superpartners have been observed, then if supersymmetry exists it must be a broken symmetry.

4.2.1 R-Parity

In order to accommodate the experimentally observed conservation of baryon and lepton numbers, the MSSM possesses a multiplicatively conserved quantum number called R-parity[2] [24]. For a particle with baryon number B, lepton number L and spin S, R is defined to be

$$R = (-1)^{3B+L+2S}. \tag{4.6}$$

All ordinary particles have an R = +1, and all supersymmetric particles have R = -1. The conservation of R-parity has three crucial implications for supersymmetric phenomenology:

1. Supersymmetric particles can only be produced in pairs.

2. Supersymmetric particles decay to other (lighter) supersymmetric particles.

3. The lightest supersymmetric particle (LSP) is absolutely stable.

Put together, these three points mean that for laboratory experiments producing supersymmetric particles which decay promptly, the final state must contain at least $2n$ LSPs, where $n \geq 1$.

4.3 Motivation for Supersymmetry

As has already been stated, supersymmetry is the last possible symmetry of the particle scattering matrix and it is important to investigate whether or not it is

[2] Extensions of the MSSM [23], which include 81 new parameters, can accommodate the observed baryon and lepton number conservation and allow for R-parity violation.

realized in nature. Indeed, many would argue that it must inevitably play a role in physics.

The theorem has deeper implications, however. It can be seen from equation 4.5 that a supersymmetric theory relates the generators of local supersymmetric transformations, Q_α, to the generators of space-time transformations, P^μ. If the supersymmetry generators are applied twice to any fermion or boson field, the result is a space-time transformation. Thus the theory provides a link between quantum field theory and general relativity. Because supersymmetry is the last possible space-time symmetry, this link is a unique one, and it is therefore not surprising that current attempts to construct a renormalisable quantum field theory of gravity (e.g. string theory [25]) assume supersymmetry.

However, the most compelling motivation for the existence of supersymmetry is that it offers a solution to the naturalness problem referred to in section 4.1. Fermionic loops give negative contributions to δm_{H}^2, whereas bosonic loops give positive contributions. The size of the contribution from a given loop depends on the size of the coupling of the fermion or boson to the Higgs field, i.e. its mass. By introducing equal mass bosonic partners to all fermions and equal mass fermionic partners to all bosons, supersymmetry results in all of the quadratic corrections canceling exactly, for all orders of perturbation theory [14, 17, 18]. In fact, supersymmetry is *required* if it is demanded that the unrenormalised theory contains no quadratic divergences to all orders of perturbation theory.

We know that supersymmetry must be a broken symmetry because the masses of the superpartners are not equal to those of their Standard Model counterparts. The symmetry is broken by introducing new terms into the supersymmetric Lagrangian which result in a splitting of the masses of the fermions and bosons in each supermultiplet. It is possible, however, to choose the form of these terms such that the quadratic divergences still cancel. This is known as *soft* symmetry breaking (section 4.5). Thus the naturalness problem is still solved. However, as explained in section 4.1, this is on the condition that the scale of supersymmetry and therefore the masses of the supersymmetric particles, are no more than around 1 TeV. These masses are becoming accessible to present particle accelerators, and since one expects the particles to have a range of masses, it is certainly possible that the lightest particles are within the reach of LEP.

In addition to these important motivations, there are aesthetic motivations, such as the fact that supersymmetric theories are mathematically much better behaved than other quantum field theories, and the fact that the spin degree of freedom is integrated into the gauge theory structure, which is not the case in the Standard Model.

Supersymmetry also solves several problems of Grand Unified Theories (GUTs) [26], which attempt to unify the strong and electroweak interactions. The first problem is in the merging of the three coupling constants associated with the gauge groups $SU(3), SU(2)$ and $U(1)$. The strong coupling constant decreases with Q^2 (Section 3.3), whereas the electroweak coupling constants increase with Q^2. The couplings have been accurately measured at $Q^2 = M_Z^2$ and can be extrapolated to higher Q^2. They are found to merge at $\sim 10^{16}$ GeV, suggesting a unification of the strong and electroweak interactions at that scale, but do not quite meet. However, when supersymmetric loops are added to the calculation, the coupling constants meet to within experimental accuracy. Secondly, GUTs predict a proton lifetime in contradiction with experiment, but in supersymmetric GUTs, the lifetime is longer. Finally, GUTs without supersymmetry predict $\sin^2\theta_W \sim 0.21$ to 0.22 [27], whereas supersymmetric GUTs predict $\sin^2\theta_W \sim 0.23$ [28], in much better agreement with experiment.

A final important motivation is the fact that the LSP (see section 4.2.1) is stable in the simplest form of the theory. Since we have not observed it, it must be weakly interacting, and since it would have been copiously produced in the Big Bang, it provides the perfect candidate for the “dark matter” referred to in section 4.1.

4.4 Field Content of the MSSM

The particle spectrum of the Minimal Supersymmetric Standard Model (MSSM) consists of the Standard Model fermions and gauge bosons, together with their supersymmetric partners.

In addition to these particles are the particles of the Higgs sector. The MSSM contains two $Y = \pm 1$ Higgs $SU(2)_L$ doublets, H_1 and H_2, compared to the single Higgs doublet required in the Standard Model. The reason for this difference is that in a supersymmetric theory, some Higgs-fermion interaction terms are not allowed, such that a $Y = +1$ Higgs can only have the Yukawa couplings necessary to give masses to quarks of charge $+2/3$, and a $Y = -1$ Higgs can give masses only to quarks of charge $-1/3$. A supersymmetric Higgs sector with two Higgs doublets is the minimal form required to generate masses for all the particles [18]. The ratio of the vacuum expectation values of the two Higgs doublet fields

$$\tan\beta = \frac{v_1}{v_2} \tag{4.7}$$

is a free parameter of the MSSM (although $v_1^2 + v_2^2$ is fixed at 246 GeV by the W mass). A second free parameter of the MSSM Higgs sector is μ, the supersymmetry conserving Higgs mass parameter. These two parameters (which replace the Standard Model Higgs mass parameter) are the only new parameters introduced by unbroken minimal supersymmetry.

The single-particle states of a supersymmetric theory are represented by "supermultiplets" which contain the fermionic and bosonic states of a given particle. The matter particles form chiral supermultiplets (table 4.1), and the gauge particles form vector supermultiplets (table 4.2). The MSSM Lagrangian is written in terms of these superfields.

Superfield	spin 0 content	spin $\frac{1}{2}$ content
L	$(\tilde{\nu}\ \tilde{\mathrm{e}}_L)$	$(\nu\ \mathrm{e})_L$
E	$\tilde{\mathrm{e}}_R$	e_R
Q	$(\tilde{u}_L\ \tilde{d}_L)$	$(u\ d)_L$
U	$\tilde{u}_R$	u_R
D	$\tilde{d}_R$	d_R
H_1	$(\mathrm{H}_1^0\ \mathrm{H}_1^-)$	$(\tilde{\mathrm{H}}_1^0\ \tilde{\mathrm{H}}_1^-)_L$
H_2	$(\mathrm{H}_2^+\ \mathrm{H}_2^0)$	$(\tilde{\mathrm{H}}_2^+\ \tilde{\mathrm{H}}_2^0)_L$

Table 4.1: *Chiral supermultiplets in the MSSM*

Superfield	spin $\frac{1}{2}$ content	spin 1 content
G	$\tilde{g}_i$	g_i
V	$\tilde{\mathrm{W}}^\pm\ \tilde{\mathrm{W}}^0$	$\mathrm{W}^\pm\ \mathrm{W}^0$
V'	$\tilde{\mathrm{B}}^0$	B^0

Table 4.2: *Vector supermultiplets in the MSSM*

4.5 Supersymmetry Breaking

The breaking of supersymmetry without reintroducing the quadratic divergences described in section 4.3 is referred to as soft supersymmetry breaking. Supersymmetry is broken in the MSSM by introducing into the Lagrangian the most general renormalisable soft supersymmetry breaking terms consistent with the $SU(3) \otimes SU(2) \otimes U(1)$ gauge symmetry and R-parity invariance. These consist of explicit mass terms corresponding to each of the supermultiplets given in tables 4.1 and 4.2, together with three new Higgs-sfermion-sfermion trilinear interaction terms.

It is very difficult (perhaps impossible) to construct a model in which the spontaneous breaking of supersymmetry arises only due to interactions of MSSM particles. It is necessary instead for there to exist a "hidden sector" consisting of particles which are completely neutral with respect to the $SU(3) \otimes SU(2) \otimes U(1)$ gauge group, and a "visible" sector consisting of the MSSM particles. Supersymmetry breaking occurs in the hidden sector and is transmitted to the MSSM by some mechanism, for which there are two theoretical scenarios.

Gravity mediated supersymmetry breaking [29] uses the fact that *all* particles feel the gravitational interaction and therefore particles in the two sectors can interact via the exchange of gravitons. In such a model, the gravitino has a mass of the order of the electroweak scale, and its couplings are gravitational in strength, so it would not be observed in collider experiments. In *gauge mediated* supersymmetry breaking (GMSB) [30], the breaking of the symmetry is transmitted from the hidden sector to the visible sector by the particles of a "messenger" sector consisting of particles with $SU(3) \otimes SU(2) \otimes U(1)$ quantum numbers. In this scenario, the gravitino mass is typically in the eV to keV range and the couplings are significantly stronger than gravitational couplings.

The breaking of supersymmetry introduces many new free parameters. In total the MSSM contains 124 truly independent free parameters [31], including the 19 free parameters of the Standard Model. Three of these parameters which are important for MSSM phenomenology are the three gaugino masses M_1, M_2 and M_3 associated with the subgroups $SU(3), SU(2)$ and $U(1)$, respectively. The parameter space is enormous[3], though the vast majority of it can be ruled out immediately due to predictions which contradict experiment.

4.6 Mass Spectrum of the MSSM

4.6.1 The MSSM Higgs sector

The MSSM Higgs sector consists of two complex scalar Higgs doublets (see Section 4.4), implying the existence of 8 real Higgs fields. Three of these are Goldstone bosons, G^0, $\mathrm{G}^{\pm}$, that are absorbed by the $\mathrm{W}^{\pm}$ and Z^0 bosons, leaving five independent physical states. There is a charged Higgs boson pair ($\mathrm{H}^{\pm}$), two CP-even neutral Higgs bosons (h^0 and H^0, where $m_{\mathrm{h}^0} \leq m_{\mathrm{H}^0}$, by definition) and one CP-odd neutral Higgs boson (A^0). These mass eigenstates are related to the fields H_1 and H_2 of Table 4.1 by [18]

$$\begin{pmatrix} \mathrm{G}^0 \\ A^0 \end{pmatrix} = \sqrt{2} \begin{pmatrix} \sin\beta & -\cos\beta \\ \cos\beta & \sin\beta \end{pmatrix} \begin{pmatrix} \mathrm{Im}[\mathrm{H}_2^0] \\ \mathrm{Im}[\mathrm{H}_1^0] \end{pmatrix}, \tag{4.8}$$

$$\begin{pmatrix} \mathrm{G}^+ \\ \mathrm{H}^+ \end{pmatrix} = \begin{pmatrix} \sin\beta & -\cos\beta \\ \cos\beta & \sin\beta \end{pmatrix} \begin{pmatrix} \mathrm{H}_2^+ \\ \mathrm{H}_1^{-*} \end{pmatrix}, \tag{4.9}$$

with $\mathrm{G}^-=\mathrm{G}^{+*}$ and $\mathrm{H}^-=\mathrm{H}^{+*}$, and

$$\begin{pmatrix} \mathrm{h}^0 \\ \mathrm{H}^0 \end{pmatrix} = \sqrt{2} \begin{pmatrix} \cos\alpha & -\sin\alpha \\ \sin\alpha & \cos\alpha \end{pmatrix} \begin{pmatrix} \mathrm{Re}[\mathrm{H}_2^0] - v_2 \\ \mathrm{Re}[\mathrm{H}_1^0] - v_1 \end{pmatrix} \tag{4.10}$$

[3] Clearly supersymmetry does not solve the parameter problem of the Standard Model. However, it should be remembered that supersymmetry appears to be an essential component of attempts to construct a fundamental unified theory (e.g. string theory), which is where the parameter problem is addressed.

which defines the angle α which can be written in terms of $\tan\beta, m_{\mathrm{A}^0}, m_{\mathrm{H}^0}, m_{\mathrm{h}^0}$ and m_{Z}. It is interesting to note that the mass of h^0 is bounded *from above* in the MSSM to be less than about 130 GeV [32]. This is slightly beyond the reach of LEP, but will be accessible to accelerators in the near future.

4.6.2 Sfermions

It should be noted that sfermions are scalar and therefore the notation $\tilde{f}_L$ and $\tilde{f}_R$ does not denote chirality, but simply identifies the Standard Model particle of which the sfermion is the superpartner. Unlike f_L and f_R which are different chirality states of the same particle, $\tilde{f}_L$ and $\tilde{f}_R$ are distinct particles which in general are not mass degenerate and, because their conserved quantum numbers are identical, can mix. The mass eigenstates are labeled $\tilde{f}_1$ and $\tilde{f}_2$, with $m_{\tilde{f}_1} < m_{\tilde{f}_2}$. The degree of mixing is given by the size of the off-diagonal term of the sfermion squared-mass matrix, which takes the form [33]

$$m^2_{\tilde{f}_{LR}} = \left\{ \begin{array}{ll} m_f(A_f - \mu\tan\beta), & \text{for} f = e, \mu, \tau, d, s, b \\ m_f(A_f - \mu\cot\beta), & \text{for} f = u, c, t \end{array} \right\} \tag{4.11}$$

where A_f is the coefficient of the appropriate trilinear interaction term referred to in Section 4.5.

Mixing is negligible for $\tilde{\mathrm{e}}$ and $\tilde{\mu}$ but is important for $\tilde{t}$, and may be important for $\tilde{b}$ and $\tilde{\tau}$ if $\tan\beta$ is large. For this reason, $\tilde{t}$ is not assumed to be degenerate with the other squark flavours, and $\tilde{t}_1$ could be the lightest squark, perhaps even lighter than the top quark. Similarly, $\tilde{\tau}_1$ may be lighter than the other sleptons.

4.6.3 Charginos

The effects of electroweak symmetry breaking allow the higgsinos and gauginos to mix. The charged higgsinos $\tilde{\mathrm{H}}^{\pm}$ and winos $\tilde{\mathrm{W}}^{\pm}$ mix to form two mass eigenstates with charge ± 1 called *charginos*, denoted by $\tilde{\chi}_i^{\pm}$ (i=1,2), where $m_{\tilde{\chi}_1^{\pm}} < m_{\tilde{\chi}_2^{\pm}}$. The mixing matrix is given by [18]

$$\mathbf{M}^{\pm} = \begin{pmatrix} M_2 & \sqrt{2} m_{\mathrm{W}} \sin\beta \\ \sqrt{2} m_{\mathrm{W}} \cos\beta & \mu \end{pmatrix}. \tag{4.12}$$

The eigenstates are

$$\begin{pmatrix} \tilde{\chi}_1^{+} \\ \tilde{\chi}_2^{+} \end{pmatrix} = \mathbf{V} \begin{pmatrix} \tilde{\mathrm{W}}^{+} \\ \tilde{\mathrm{H}}^{+} \end{pmatrix}; \qquad \begin{pmatrix} \tilde{\chi}_1^{-} \\ \tilde{\chi}_2^{-} \end{pmatrix} = \mathbf{U} \begin{pmatrix} \tilde{\mathrm{W}}^{-} \\ \tilde{\mathrm{H}}^{-} \end{pmatrix}, \tag{4.13}$$

where $\mathbf{V}$ and $\mathbf{U}$ are chosen such that

$$\mathbf{U}^{*}\mathbf{M}^{\pm}\mathbf{V}^{-\mathbf{1}} = \begin{pmatrix} m_{\tilde{\chi}_1^{\pm}} & 0 \\ 0 & m_{\tilde{\chi}_2^{\pm}} \end{pmatrix}. \tag{4.14}$$

The chargino masses are the eigenvalues $m_{\tilde{\chi}_2^{\pm}}$ and $m_{\tilde{\chi}_1^{\pm}}$, which depend on the unknown values of $M_2, \tan\beta$ and μ.

4.6.4 Neutralinos

The neutral higgsinos ($\tilde{\mathrm{H}}_1^0$ and $\tilde{\mathrm{H}}_2^0$) and the neutral gauginos ($\tilde{\mathrm{B}}^0$ and $\tilde{\mathrm{W}}^0$) mix to form four neutral mass eigenstates called *neutralinos*, denoted by $\tilde{\chi}_i^0$ (i=1,...4), where $m_{\tilde{\chi}_1^0} < m_{\tilde{\chi}_2^0} < m_{\tilde{\chi}_3^0} < m_{\tilde{\chi}_4^0}$. In the basis $\psi^0 = (\tilde{\mathrm{B}}^0, \tilde{\mathrm{W}}^0, \tilde{\mathrm{H}}_1^0, \tilde{\mathrm{H}}_2^0)$, the mixing matrix is given by [18]

$$\mathbf{M}^0 = \begin{pmatrix} M_1 & 0 & -c_\beta s_W m_Z & s_\beta s_W m_Z \\ 0 & M_2 & c_\beta c_W m_Z & -s_\beta c_W m_Z \\ -c_\beta s_W m_Z & c_\beta c_W m_Z & 0 & -\mu \\ s_\beta s_W m_Z & -s_\beta c_W m_Z & -\mu & 0 \end{pmatrix}. \tag{4.15}$$

where $s_\beta = \sin\beta, c_W = \cos\theta_W$, etc. The masses of the neutralinos are the four eigenvalues of this matrix, by analogy with the discussion for charginos. The masses (and couplings) depend on the unknown values of $M_1, M_2, \tan\beta$ and μ.

4.6.5 The Lightest Supersymmetric Particle (LSP)

As stated in section 4.2.1, if R-parity is conserved, then the LSP is stable, and is therefore very important to supersymmetric phenomenology. In order to be consistent with cosmological constraints, the LSP must be electrically and colour neutral with only weak interactions [34]. The possible candidates are the sneutrinos, the lightest neutralino, or the gravitino. Of these, $\tilde{\chi}_1^0$ is the lightest over most of the parameter space, and is generally considered to be the LSP. The gravitino is however the LSP in GMSB models (see section 4.5). A neutralino LSP is particularly interesting as a dark matter candidate, as the predicted relic density from the Big Bang is consistent with the astronomically observed dark matter density for large regions of the MSSM parameter space [14].

Since the LSP is only weakly interacting, it will not be observed in detectors. Therefore, since the final state of any event involving the production of supersymmetric particles must contain (at least) two LSPs (section 4.2.1), the canonical signature for supersymmetry is significant missing energy and momentum.

4.7 Production and Leptonic Decays of Sleptons, Charginos and Charged Higgs at LEP

Due to R-parity conservation, all supersymmetric particles are produced in pairs. LEP is an e^+e^- collider which can pair produce supersymmetric particles with mass less than the beam energy. Sleptons, charginos and charged Higgs bosons can all be produced via s-channel γ^* or Z^* exchange, as, for example, in Figure 4.2.

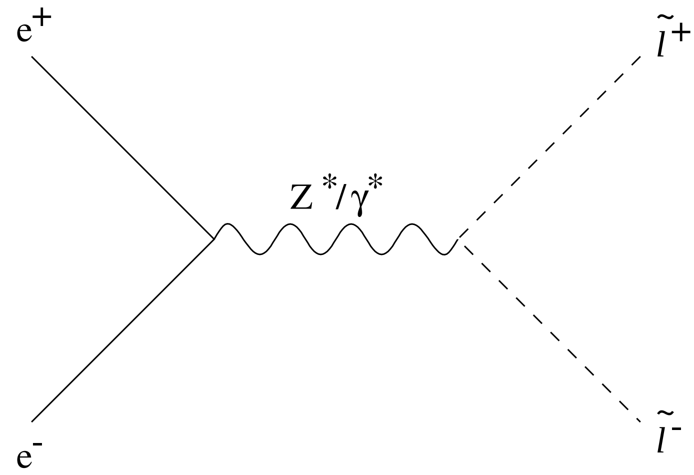

Figure 4.2: *Feynman diagram for slepton pair production at LEP.*

4.7.1 Sleptons

At high energies, the s-channel production cross-section for sleptons is given by [21]

$$\sigma(\mathrm{e}^+\mathrm{e}^- \to \tilde{\ell}^+\tilde{\ell}^-) = (\pi\alpha^2/3s)\beta^3[e^2 + 8re(I_3 - e\sin^2\theta_W)(1 - 4\sin^2\theta_W) + 16r^2(I_3 - e\sin^2\theta_W)^2(1 + (1 - 4\sin^2\theta_W)^2)] \quad (4.16)$$

where e and I_3 are the electric charge and third component of weak isospin, with values $e = -1$, $I_3 = -1/2$ for left-handed charged sleptons, and $e = -1$, $I_3 = 0$ for right-handed charged sleptons. s is the square of the centre-of-mass energy, β is the velocity of the slepton and $r = s/[16(s - m_{\mathrm{Z}}^2)\cos^2\theta_W \sin^2\theta_W]$.

The slepton production cross-section is thus proportional to β^3/s. This leads to a suppression of slepton production close to the kinematic threshold.

In addition, selectrons can be produced by t-channel neutralino exchange (Figure 4.3). This changes the angular distribution substantially, to an extent which depends on the nature of the neutralinos, leading generally to an increased cross-section towards $-q\cos\theta = +1$, where q is the charge of the selectron. It also generally increases the total cross-section substantially.

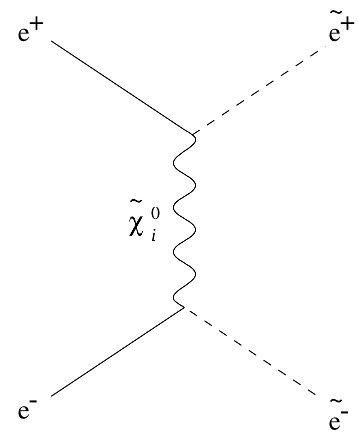

Figure 4.3: *Feynman diagram for t-channel selectron pair production.*

Sleptons decay predominantly via the process $\tilde{\ell}^{\pm} \to \ell^{\pm}\tilde{\chi}^0_1$ (assuming $\tilde{\chi}^0_1$ to be the LSP), leading to an event topology of two leptons plus significant missing transverse momentum. If the slepton is the next to lightest supersymmetric particle, then this is the only possible decay mode. Examples of other possible decay modes are:

- $\tilde{\ell}^{\pm} \to \ell^{\pm}\tilde{\chi}^0_2, \tilde{\chi}^0_2 \to \mathrm{Z}^*\tilde{\chi}^0_1$, with Z^* decaying either hadronically or leptonically, which can occur if $m_{\tilde{\chi}^0_2} < m_{\tilde{\ell}^{\pm}}$.
- $\tilde{\ell}^{\pm} \to \tilde{\chi}^{\pm}_1\nu_{\ell}$, with $\tilde{\chi}^{\pm}_1$ decaying either hadronically or leptonically, which can occur if $m_{\tilde{\chi}^{\pm}_1} < m_{\tilde{\ell}^{\pm}}$ [4].

4.7.2 Charginos

Charginos are produced via s-channel γ^* or Z^* exchange, or by t-channel $\tilde{\nu}$ exchange. The contribution to the total cross-section from the t-channel process depends on the nature of $\tilde{\chi}^{\pm}_1$. As for selectrons, the t-channel contribution leads to an increased cross-section towards $-q\cos\theta = +1$. The chargino production cross-section is generally large ($\sim$ 1-10 pb). It is enhanced when Higgsino components dominate the

[4]This decay mode is possible only for left-handed (or mixed) sleptons.

chargino field content, and suppressed for $m_{\tilde{\nu}}$ less than ~ 100 GeV due to destructive interference between the s- and t-channel processes. The cross-section is proportional to β/s, so chargino production has a less pronounced kinematic suppression close to threshold than that for sleptons.

The possible decay modes for charginos are summarized by the two diagrams shown in figure 4.4. If kinematically allowed, there are many possible cascade decays. The analysis described in this thesis is concerned with the leptonic decay modes, of which there are three possibilities:

- "3-body decay": $\tilde{\chi}_1^\pm \to \tilde{\chi}_1^0 \ell^\pm \nu_\ell$, which occurs via a virtual $W^\pm$
- "2-body decay": $\tilde{\chi}_1^\pm \to \ell^\pm \tilde{\nu}_\ell$, where $\tilde{\nu}_\ell$ decays invisibly to $\tilde{\chi}_1^0 \nu_\ell$, and
- $\tilde{\chi}_1^\pm \to \tilde{\ell}^\pm \nu_\ell, \tilde{\ell}^\pm \to \ell^\pm \tilde{\chi}_1^0$.

The 2-body decay mode is dominant if the sneutrino is lighter than chargino. The third possibility is not considered in the analysis, because the kinematics are determined by three unknown masses, and because of the negative results of the direct search for sleptons presented in this thesis.

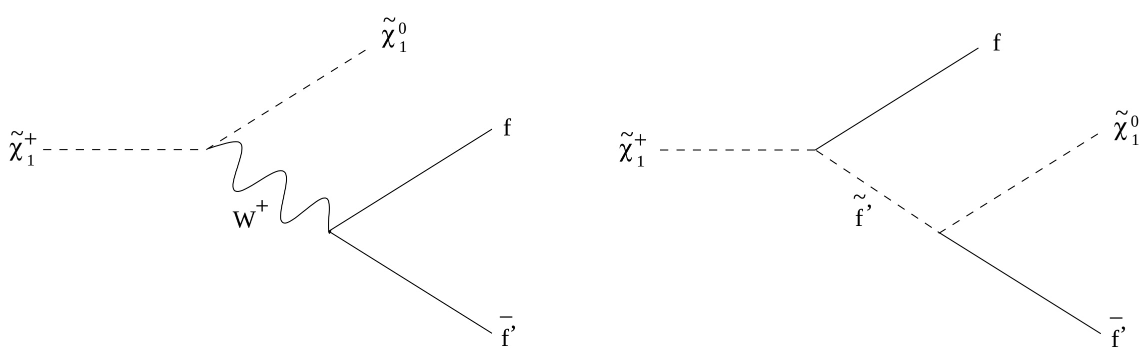

Figure 4.4: *Feynman diagrams for chargino decay.*

4.7.3 Charged Higgs

Like the sleptons, the charged Higgs boson is a scalar particle, produced via s-channel γ^* or a Z^* exchange with production cross-section proportional to β^3/s. Since the coupling of the Higgs field is strongest to particles of high mass, $H^\pm$ decays preferentially to $c\bar{s}$ ($t\bar{b}$ is kinematically inaccessible) or to $\tau^\pm\nu_\tau$.

Chapter 5

General Selection of Di-lepton Events with Significant Missing Momentum

5.1 Introduction

The analysis described in this thesis is performed using data from e^+e^- collisions at LEP collected by the OPAL detector in 1997 and 1998. The high energy data taken in 1997 and 1998 were at luminosity weighted average centre-of-mass energies of 182.7 GeV and 188.7 GeV, respectively, with integrated luminosities corresponding to 56.4 pb^{-1} and 181.0 pb^{-1}, respectively.

The starting point of the analysis described in the proceeding chapters is a set of events selected as being consistent with the acoplanar di-lepton topology. The selection of these events will be referred to subsequently as the "general selection". In the context of this selection any process that produces an event containing two oppositely charged leptons and genuine prompt missing transverse momentum is considered as signal. Such events could be produced by Standard Model processes with the final state $\ell^+\nu\,\ell^-\overline{\nu}$, or by a new physics process with weakly interacting particles (e.g. $\tilde{\chi}^0_1, \tilde{G}, \nu$) in the final state. All Standard Model processes that do not lead to $\ell^+\nu\,\ell^-\overline{\nu}$ final states are considered as background and the purpose of the general selection is to reduce this background as far as possible.

5.2 Monte Carlo Simulation of Standard Model processess

Standard Model processes with the final state $\ell^+\nu\,\ell^-\overline{\nu}$ are considered as signal in the context of the general selection. By far the dominant source of such events is the pair production of W bosons, $e^+e^- \rightarrow W^+W^-$, in which both W bosons decay leptonically: $W^- \rightarrow \ell^-\overline{\nu}_\ell$. W^+W^- production can occur in the s-channel via a Z^* or a γ^* (Figure 5.1(a)) or in the t-channel via an electron-neutrino (Figure 5.1(b)). Other processes giving the $\ell^+\nu\,\ell^-\overline{\nu}$ final state are $(Z^*/\gamma^*)(Z^*/\gamma^*)$ (Figure 5.1(c)), (Z^*/γ^*)ee (Figure 5.1(d)) and Weν (Figure 5.1(e)).

At $\sqrt{s}$ = 183 GeV, these four-fermion processes are simulated using the grc4f [35] generator, which calculates the cross-sections including interference effects. At $\sqrt{s}$ = 189 GeV, a new version of the KORALW [36] generator is used, which uses the grc4f matrix elements to calculate the cross-sections but also includes a detailed description of hard radiation from initial, intermediate and final state charged particles.

There are a number of sources of Standard Model background in which a missing momentum signature can be faked by, for example, particles that escape down the beam pipe or strike regions of the detector where they are poorly measured, or by secondary neutrinos from tau decays. The most important sources of background are two-photon processes (Figure 5.2), in which the electron and positron escape

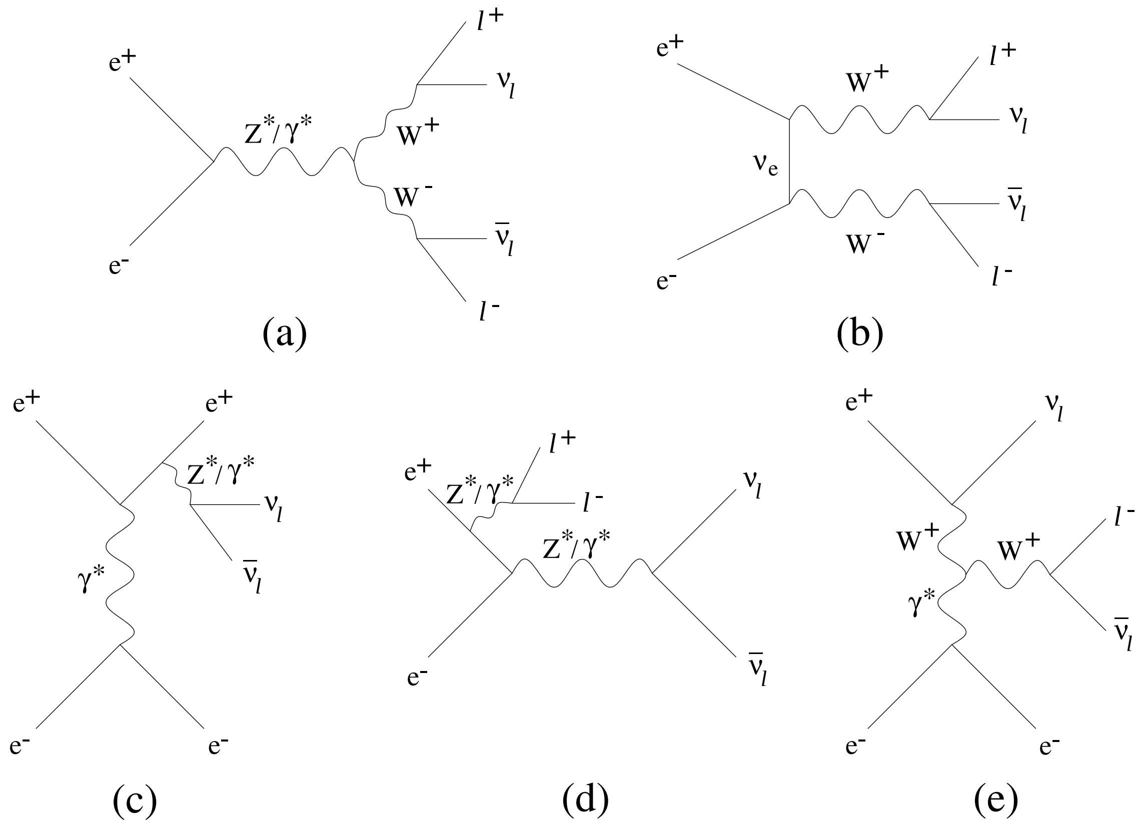

Figure 5.1: *Feynman diagrams for Standard Model processess with the final state* $\ell^+\nu\,\ell^-\overline{\nu}$*: (a) s-channel* $\mathrm{W^+W^-}$ *production, (b) t-channel* $\mathrm{W^+W^-}$ *production, (c)* $(Z^*/\gamma^*)(Z^*/\gamma^*)$*, (d)* $(Z^*/\gamma^*)ee$ *and (e)* $We\nu$*.*

undetected down the beam pipe. These processes are simulated using the program of Vermaseren [37] and grc4f for $\mathrm{e^+e^-}\ell^+\ell^-$, and using PHOJET [38], HERWIG [39] and grc4f for $\mathrm{e^+e^-q\overline{q}}$. Because of the large total cross-section for $\mathrm{e^+e^-e^+e^-}$, $\mathrm{e^+e^-}\mu^+\mu^-$ and $\mathrm{e^+e^-q\overline{q}}$, soft cuts are applied at the generator level to preselect events that might possibly lead to background in the selection of $\ell^+\nu\,\ell^-\overline{\nu}$ final states. No generator level cuts are applied to the $\mathrm{e^+e^-}\tau^+\tau^-$ generation.

Another important source of background is lepton pair production, particularly $\tau^+\tau^-$ production, in which the missing momentum is carried by the neutrinos produced in the decay of the tau, but also electron and muon pair production in which there is initial or final state radiation of a photon. The production of lepton pairs is

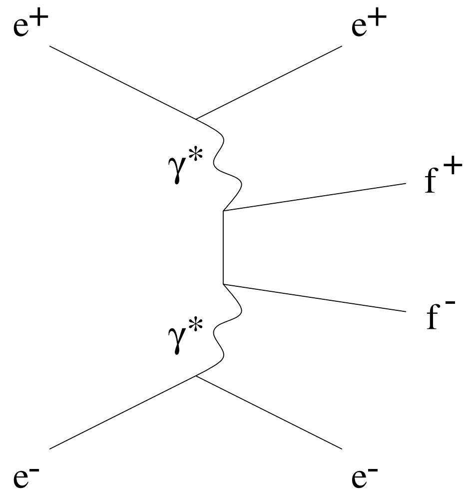

Figure 5.2: *Feynman diagram for two-photon processes.*

generated using BHWIDE [40] and TEEGG [41] for $e^+e^-(\gamma)$, and using KORALZ [42] for $\mu^+\mu^-(\gamma)$ and $\tau^+\tau^-(\gamma)$. To complete the Standard Model background simulation, the production of quark pairs, $q\overline{q}(g)$, is generated using PYTHIA [43] and the final state $\nu\bar{\nu}\gamma\gamma$ is generated using NUNUGPV98 [44] and KORALZ.

5.3 Monte Carlo Simulation of New Physics Processes

Slepton pair production is generated using SUSYGEN [45]. As discussed in Section 4.7, selectrons can be produced by t-channel neutralino exchange, and the production cross-section and angular distribution depends on the nature of the neutralino, which in turn depends on μ and $\tan\beta$. Selectron samples were generated with μ = -200 GeV and $\tan\beta = 1.5$ as this was shown, by varying μ and $\tan\beta$, to give a conservative estimate of the selection efficiency for selectrons [46]. Monte Carlo samples were generated at both $\sqrt{s} = 183$ GeV and $\sqrt{s} = 189$ GeV, for a grid of points in the $(m, \Delta m)$ plane, where m is the slepton mass and Δm is the slepton-neutralino mass difference. Values of m range from 45 GeV [1] to the beam energy in 5 GeV steps (the highest mass at $\sqrt{s} = 189$ GeV is an exception at 94 GeV), and nine values of Δm are used: 2 GeV, 2.5 GeV, 5 GeV, 10 GeV, 20 GeV, $m/2$, $m-10$, $m-20$ and m. Chargino pair production is generated using DFGT [47] for three-body decays, and SUSYGEN for two-body decays. Δm for the chargino analyses is the mass difference $m_{\chi_1^\pm} - m_{\tilde{\chi}_1^0}$ for three-body decays and $m_{\chi_1^\pm} - m_{\tilde{\nu}}$ for two-body decays. The mass grids used are given in Tables 8.4 and 8.5 for two- and three-body chargino generation, respectively[2]. Charged Higgs boson pair production is generated using HZHA [48] and PYTHIA, for charged Higgs masses between 45 GeV and the beam energy, in 5 GeV steps.

5.4 Overview of the Event Selection

The general selection of acoplanar di-lepton events was developed by Terry Wyatt and Graham Wilson and does not form part of the analysis performed by the author. However, a brief description of the event selection is included in this thesis for completeness.

The essence of the general selection is the selection of events containing low multiplicity jets with significant missing transverse momentum. A detailed description of the event selection is given in the appendices of [49], a paper detailing the analysis of the data taken in 1996. Subsequent improvements to the selection are described in [50] and [46]. There are two independently developed selections. In Selection I, particular emphasis is placed on retaining efficiency for events with very low visible energy, but nevertheless significant missing transverse momentum. This is important for providing sensitivity to new physics processes at low Δm. Selection II is

[1]Particle masses less than 45 GeV are not considered because these masses were accessible at LEP1 and because radiative return to the Z^0 means that the event topology can be different.

[2]The full grid also includes $m\chi_1^\pm$=85 GeV, not shown in the tables.

optimized to select high visible energy events such as those from W^+W^- production. The general selection is defined as the logical ".OR." of these two selections.

In both selections, the most important cuts are those which require evidence for the production of an invisible system that carries away significant missing energy and momentum. The most important source of background is from processes giving rise to missing momentum along the beam axis due to high energy particles travelling down the beam pipe (e.g. two-photon processes). Therefore events are required to have significant missing momentum in the plane perpendicular to the beam axis (p_t^{miss}) and the total missing momentum vector is required to point away from the beam axis. The scale of the cut on (p_t^{miss}) is set by the location of the inner edge of the SW detector at approximately 0.025 rad to the beam direction, which allows a beam energy scattered electron or photon to carry away a p_t^{miss} of $0.025E_{\mathrm{beam}}$.

Background events containing neutrinos (in particular from tau decay) or poorly measured particles can, however, have a large value of p_t^{miss} and a missing momentum vector pointing at a large angle to the beam axis. However, the majority of background events contain leptons which are approximately back-to-back in the plane perpendicular to the beam axis (coplanar). For coplanar events, a cut on the component of p_t^{miss} that is perpendicular to the event thrust axis in the transverse plane, a_t^{miss}, performs better than a cut on either p_t^{miss} or on the acoplanarity angle, ϕ_{acop}. This can be seen by considering, for example, electrons produced in tau decay. Low momentum electrons from this source may be produced at very large angles to the original tau direction (thus causing a large ϕ_{acop}), but their momentum transverse to the original tau direction (and thus their contribution to a_t^{miss}) is small. In events that are relatively coplanar a cut on a_t^{miss} is applied and the direction of the missing momentum vector is calculated using a_t^{miss} rather than p_t^{miss}. At large acoplanarity cuts using a_t^{miss} no longer discriminate sufficiently between signal and background and a hard cut on p_t^{miss} and a conventional cut on the direction of the missing momentum are made.

5.4.1 Selection I

The first group of cuts requires evidence that the event contains two leptons[3] and no other particles. Events are required to contain at least one isolated[4] lepton candidate with $p_t > 1.5$ GeV. If the event contains a second isolated lepton candidate then there must be no charged tracks other than those associated to the two lepton candidates. If the event contains only one isolated lepton candidate, the event is not rejected, provided that the lepton is identified as an electron or muon, and the tracks and clusters not associated to the lepton satisfy the following requirements: there is at least one additional charged track, at least one track has $p_t > 0.3$ GeV, the total number of additional tracks and clusters does not exceed 4, and the invariant mass of the additional tracks and clusters does not exceed the tau mass. In this case the remaining tracks and clusters are considered to be the second lepton which is classified as "unidentified".

The second group of cuts are those requiring evidence for the production of an invisible system that carries away significant missing energy and momentum:

small acoplanarity $\phi^{\mathrm{acop}} < 1.2$ rad:

1. $p_t^{\mathrm{miss}}/E_{\mathrm{beam}} > 0.035$.
2. $a_t^{\mathrm{miss}}/E_{\mathrm{beam}} > 0.025$.
3. $|\cos\theta_{\mathrm{a}}^{\mathrm{miss}}| < 0.99$, where the direction of the missing momentum vector is calculated using the missing momentum perpendicular to the event axis in the transverse plane, $\theta_{\mathrm{a}}^{\mathrm{miss}} = \tan^{-1}(a_t^{\mathrm{miss}}/p_{\mathrm{z}}^{\mathrm{miss}})$ and $p_{\mathrm{z}}^{\mathrm{miss}}$ is the total momentum of the observed particles in the z direction.

[3] Lepton identification is discussed in Section 5.5.

[4] The isolation of electron and muon candidates is defined by considering tracks and clusters within a cone of half opening angle 20° around the lepton direction. The isolation of hadronic tau candidates is defined by considering tracks and clusters within a cone of half opening angle 60°, but outside a cone of half opening angle 35°. Details are given in [49].

large acoplanarity $\phi^{\rm acop} > 1.2$ rad:

1. $p_t^{\rm miss}/E_{\rm beam} > 0.045$.
2. $|\cos\theta_{\rm p}^{\rm miss}| < 0.90$, where the direction of the missing momentum vector is given by $\theta_{\rm p}^{\rm miss} = \tan^{-1}(p_t^{\rm miss}/p_{\rm z}^{\rm miss})$.

$p_t^{\rm miss}$ is required to exceed the above cut values by at least one standard deviation of the measurement uncertainty on $p_t^{\rm miss}$. Loose cuts are also applied to $\phi_{\rm acop}$ and the acolinearity $\theta_{\rm acol}$ [5].

The majority of the remaining cuts are designed to reject events in which missing transverse momentum is faked, in particular, by two-photon events in which particles strike the detector in regions where they are undetected or poorly measured. All events with an FD or SW cluster energy $E/E_{\rm beam} > 0.8$ or an SW cluster consistent with a minimum ion-ising particle are rejected. Other two-photon vetoes are applied only to events that are likely to have originated from two-photon processes ($a_t^{\rm miss}/E_{\rm beam} < 0.20$ for $\phi_{\rm acop} < 1.2$ rad and $p_t^{\rm miss}/E_{\rm beam} < 0.25$ for $\phi_{\rm acop} > 1.2$ rad). The most important of these are:

- Events with an FD or SW cluster energy $E/E_{\rm beam} > 0.15$ are rejected and events with lower energy clusters are rejected if they are back-to-back within 1.2 rad with the total momentum vector of the event.
- Events are rejected if both lepton candidates satisfy $|\cos\theta| > 0.95$.
- The MIP plug is used to reject events of type $e^+e^-\mu^+\mu^-$, by vetoing events that contain coincident hits in two or more scintillator layers at the same ϕ and at the same end of OPAL, satisfying cuts on pulse height and timing.

[5] The acolinearity angle is defined as the supplement of the three dimensional angle between the two leptons.

5.4.2 Selection II

A cone algorithm is used with a cone half-opening angle of 20° to define low multiplicity [6] "jets" with minimum energy 2.5 GeV, corresponding to each lepton candidate. A separate selection is defined for events containing one, two and three jets. 90% of events fall into the 2-jet category, with 4% and 6% in the single-jet and 3-jet categories, respectively.

2-jet Selection

The most important cuts are those requiring missing energy:

1. $\phi^{\mathrm{acop}} > 5°$.
2. (a) The net transverse momentum of the two-jet system divided by the beam energy, x_T, must exceed 0.05. (b) It is further required that the significance of x_T exceeding 0.05 is greater than 1 standard deviation.
3. For events with $\phi^{\mathrm{acop}} > 90°$ it is required that the direction of the missing momentum satisfies $|\cos\theta_{\mathrm{p}}^{\mathrm{miss}}| < 0.95$. For events with $\phi^{\mathrm{acop}} < 90°$ it is required that $a_t^{\mathrm{miss}}/E_{\mathrm{beam}} > 0.022$, and that $\sin\theta_{\mathrm{a}}^{\mathrm{miss}} > 0.060$.

Other important cuts are as follows:

1. For events with $\phi^{\mathrm{acop}} < 30°$ or $\theta_{\mathrm{acol}} < 15°$, the event is rejected if the most energetic jet with no associated charged tracks has energy exceeding 80% of the beam energy.

The following cuts are are applied only if the event is classified as being "low x_T" or "medium x_T". Low x_T events are defined as those where the x_T significance

[6] Events are required to contain between 1 and 8 charged tracks, and no more than 15 charged tracks and electromagnetic calorimeter clusters.

of the x_T exceeding 0.15 is less than one standard deviation. If the event is not classified as low x_T, it will be called medium x_T if the x_T significance of the x_T exceeding 0.23 is less than one standard deviation.

2. The event is rejected if there is a coincidence in the MIP-PLUG at the same end and azimuth which is within $60°$ of the missing transverse momentum direction. MIP-PLUG hits are considered for coincidence making if the ADC charge is at least 50 counts.

3. Events with evidence for significant activity in the gamma-catcher region are rejected if either: (a) there is a MIP-PLUG coincidence with maximum charge exceeding 2500 ADC counts, or (b) there is a gamma-catcher cluster with energy exceeding 5 GeV.

3-jet Selection

The cuts are similar to those used in the 2-jet selection, but a third, neutral jet is allowed. Vetoes are made against radiative lepton pair events. The cuts requiring missing momentum are: (a) the sum of the opening angles among the three 2-jet pairings should be less than $359°$, (b) the x_T of the 3-jet system should exceed 0.05 and have x_T significance exceeding 1 standard deviation, and (c) $|\cos\theta_{\mathrm{p}}^{\mathrm{miss}}| < 0.95$.

Single-jet Selection

Cuts are made on x_T and $\cos\theta$, the cut value depending on the nature of the jet. The jet must be associated with an ECAL cluster and the most energetic charged track in the jet must be identified as an electron or muon or have ECAL energy exceeding 5 GeV. Additional cuts depend on the nature of the jet and involve vetoes on activity in the forward region back to back to the jet, in order to remove background from lepton pair and leptonic two photon events.

5.5 The Event Set Passing the General Selection

The numbers of events passing the general selection at each centre-of-mass energy in the data are compared to the Standard Model Monte Carlo predictions in Table 5.1. The total number of events predicted by the Standard Model is given, together with a breakdown into the contributions from individual processes. The number of observed candidates is consistent with the expectation from Standard Model sources, which is dominated by the $\ell^+\nu\,\ell^-\overline{\nu}$ final state arising mostly from $\mathrm{W^+W^-}$ production.

$\sqrt{s}$ (GeV)	data	SM	$\ell^+\nu\,\ell^-\overline{\nu}$	$\mathrm{e^+e^-}\ell^+\ell^-$	$\ell^+\ell^-\mathrm{q\overline{q}}$	$\ell\ell(\gamma)$	$\nu\bar{\nu}\gamma\gamma$
183	78	81.4±0.8	77.5±0.7	3.4±0.5	0.07±0.03	0.31±0.04	0.06±0.03
189	301	303.3±1.9	292.5±1.6	4.4±0.8	1.3±0.1	4.6±0.4	0.46±0.04

Table 5.1: *Comparison between data and Monte Carlo of the number of events passing the general selection at each centre-of-mass energy. The total number of events predicted by the Standard Model is given, together with a breakdown into the contributions from individual processes. The Monte Carlo statistical errors are shown.*

Discrimination between Standard Model and new physics sources of lepton pair events with missing momentum, described in Section 6, is provided by information on the lepton identification, the acolinearity of the event, and the momentum and $-q\cos\theta$ of the observed lepton candidates, where q and θ are the charge and polar production angle of the lepton. The degree to which these quantities are described by the Standard Model Monte Carlo at the level of the general selection is checked here. The lepton identification information in the event sample produced by the general selection at each centre-of-mass energy is compared with the Standard Model Monte Carlo in Table 5.2. Leptons are identified as electrons or muons according to the criteria given in Appendix I.2 of [49]. A leptonically decaying tau is usually identified as $\mathrm{e}^{\pm}$ or $\mu^{\pm}$. A lepton is identified as a hadronically decaying tau (given the symbol "h") if there are no more than three tracks within a cone of half opening

Lepton identification	$\sqrt{s}=189$ GeV		$\sqrt{s}=183$ GeV	
	data	SM	data	SM
e^+e^-	49	45.2±0.7	14	12.1±0.3
$\mu^+\mu^-$	49	47.0±0.7	13	13.7±0.3
$h^\pm h^\mp$	16	11.0±0.5	1	2.5±0.2
$e^\pm\mu^\mp$	79	83.4±0.9	20	25.6±0.4
$e^\pm h^\mp$	26	36.6±0.6	8	9.8±0.3
$\mu^\pm h^\mp$	40	35.4±0.6	8	9.2±0.2
$e^\pm$, unidentified	20	19.6±0.7	5	3.8±0.2
$\mu^\pm$, unidentified	14	17.8±0.5	7	3.7±0.2
$h^\pm$, unidentified	8	7.3±0.3	2	0.9±0.1

Table 5.2: *The lepton identification information in the events passing the general selection compared with the Standard Model Monte Carlo at each centre-of-mass energy. The symbol 'h" is defined in the text. "Unidentified" means that only one isolated lepton has been positively identified in the event (see Section 5.4.1).*

angle 35° and the invariant mass of the tracks and clusters within the cone is less than the tau mass (assuming the pion mass for each track). For the event sample at $\sqrt{s} = 189$ GeV, Figure 5.3 shows the distributions of (a) the momentum scaled by the beam energy of each charged lepton candidate, (b) the value of $-q\cos\theta$ of each charged lepton candidate, (c) the acolinearity of the event, (d) the invariant mass of the invisible particles, m_{recoil}, (e) the invariant mass of the lepton pair, $m_{\ell\ell}$ and (f) the value of $a_t^{\rm miss}/E_{\rm beam}$ (defined in section 5.4). The data are compared with the Standard Model Monte Carlo predictions, which are dominated by the final state $\ell^+\nu\,\ell^-\overline{\nu}$.

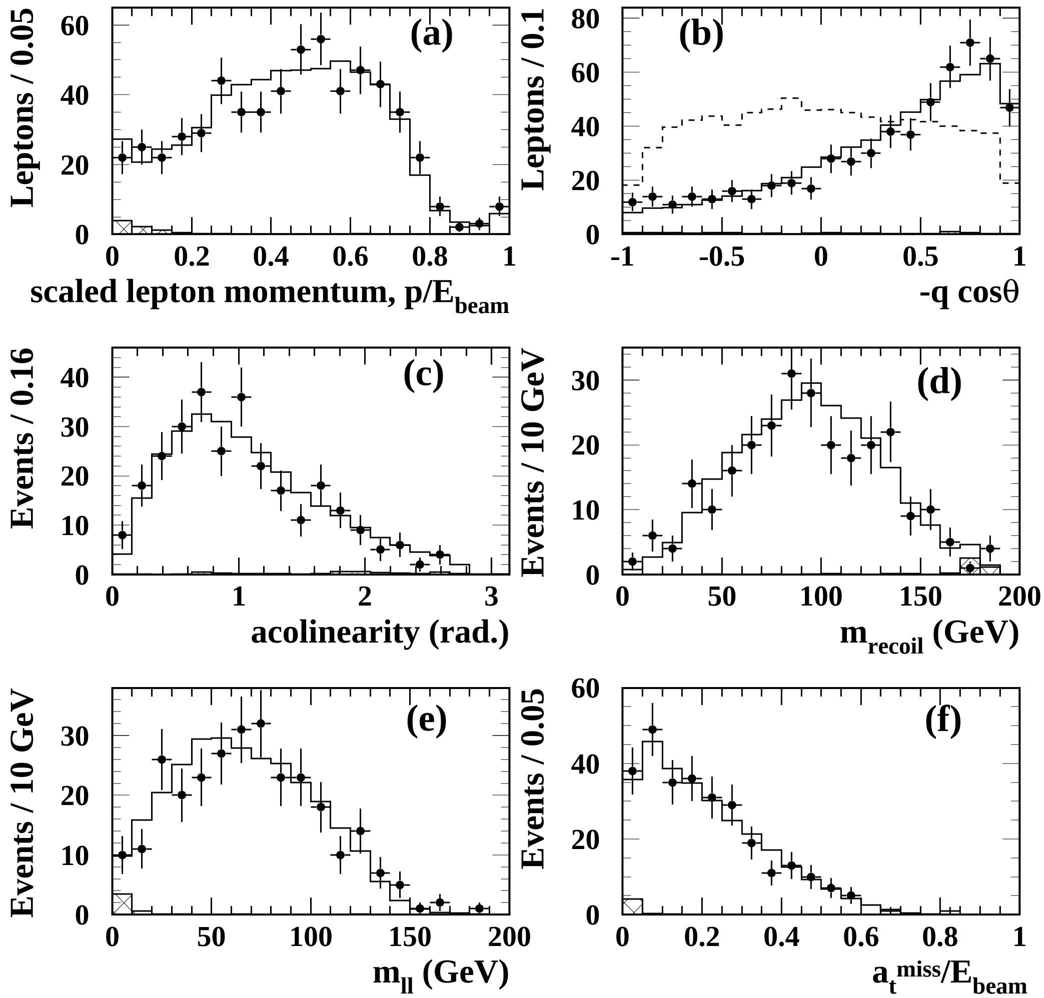

Figure 5.3: *Distributions of (a) the lepton momentum divided by the beam energy, (b) $-q\cos\theta$ and (c) acolinearity (in radians), (d) m_{recoil}, (e) $m_{\ell\ell}$, and (f) $a_t^{\rm miss}/E_{\rm beam}$, for the event sample produced by the general selection at $\sqrt{s}$ = 189 GeV. The data are shown as the points with error bars. The Monte Carlo prediction for 4-fermion processes with genuine prompt missing energy and momentum ($\ell^+\nu\,\ell^-\overline{\nu}$) is shown as the open histogram and the background, arising mainly from processes with four charged leptons in the final state, is shown as the shaded histogram. In (b) the dashed histogram corresponds to the distribution expected from smuon pair production, with arbitrary normalization. In (a) and (b) there are two entries per event for events containing two identified leptons.*

Chapter 6

Likelihood Method to Distinguish Signal and Background

6.1 Introduction

The aim of this analysis is to use the set of data passing the general selection of acoplanar di-lepton events to search for the new physics processes listed in Section 1. There are a number of variables which can be used to distinguish between Standard Model sources of such events (mainly $\ell^+\nu\,\ell^-\overline{\nu}$ from leptonically decaying W pairs, now considered as background) and the new physics signals from the production and leptonic decay of sleptons, charginos and charged Higgs bosons. A likelihood technique is used to combine the information from these variables in order to make the distinction.

The expected distributions of each of the discriminating variables (in particular, the lepton momenta) for a given new physics process vary considerably with the mass, m, of the particle searched for, and with the mass difference, Δm, between the parent particle and the invisible daughter particle (e.g. neutralino) to which it decays. For this reason an essentially independent analysis must be performed for every value of m and Δm considered, for each new physics search channel. Subsequent references to "signal" imply the signal for a particular m, Δm and search channel.

6.2 The Relative Likelihood, L_R

Discrimination between new particle pair production and the Standard Model background is performed by considering the likelihood that an event is consistent with being either signal or background. Given an event, for which the values of a set of variables x_i are known, the likelihood, L_S, of the event being consistent with the signal hypothesis is calculated as the product of the probabilities, $P_S(x_i)$, that the signal hypothesis would produce an event with variable i having value x_i:

$$L_S = \prod_i P_S(x_i). \tag{6.1}$$

Similarly, the likelihood of an event being consistent with the background hypothesis is:

$$L_B = \prod_i P_B(x_i). \tag{6.2}$$

The combined discriminating quantity is the relative likelihood, L_R, defined by:

$$L_R = \frac{L_S}{L_S + L_B}. \tag{6.3}$$

An event with high L_R is signal-like and an event with low L_R is background-like.

The following quantities are used as likelihood variables (x_i) in the analysis:

(i) Scaled momentum, p/E_{beam}, of each lepton,

(ii) Acolinearity of the event,

(iii) $-q\cos\theta$ for each lepton (smuons, staus and charged Higgs bosons only),

(iv) Lepton type variable (defined in Section 6.6).

Sections 6.3 to 6.6 describe the properties of each of these variables for signal and background.

6.3 The Momentum Likelihood Variable

The dominant Standard Model process leading to the acoplanar di-lepton signature arises from leptonically decaying W pairs, and the momentum distribution is highly populated between about 0.25 and 0.7 (Figure 5.3(a)). The kinematics for the signal vary considerably with Δm ($m_{\tilde{\ell}^\pm} - m_{\tilde{\chi}_1^0}$ for sleptons, $m_{\tilde{\chi}_1^\pm} - m_{\tilde{\nu}}$ and $m_{\tilde{\chi}_1^\pm} - m_{\tilde{\chi}_1^0}$ for charginos undergoing two- and three-body decay, respectively), as this determines how much energy is available to the leptons. When Δm is small, the lepton momenta are small, and the signal is similar to the background from two-photon events, whereas at high Δm, the visible energy is high and the events look similar to the W^+W^- background. The kinematics also vary to a lesser extent with the mass m of the parent particle. For low values of m, the momentum distribution is spread out due to Lorentz boost effects, whereas close to the kinematic threshold for production, the parent particles are approximately at rest and the range of lepton momenta is small.

Additional discriminating power can be obtained from the lepton momenta by using the fact that for a given m and Δm, the lepton momentum distribution varies according to the acolinearity of the event. Since the parent particles (e.g. sleptons) are produced back to back, then if an event has high acolinearity, one of the leptons will typically be travelling in a direction at an angle greater than $\pi/2$ to that of the parent particle (in the lab. frame). In this case, the lepton momentum in the lab. frame is reduced relative to its value in the rest frame of the parent particle and the lepton is therefore soft. An event with low acolinearity will in general have both leptons travelling in similar directions to the parent particles and the Lorentz boost results in both leptons having high momenta, provided that the parent particle mass is not close to the kinematic limit. Since the Lorentz boost is greater for low parent particle mass, these effects are stronger when m is small.

Figure 6.1 shows momentum distributions in the (x_{max}, x_{min}) plane, where x_{max} and x_{min} are the scaled momenta of the higher and lower momentum leptons, respectively, for a smuon signal with m=45 GeV, Δm=45 GeV, for 3 different ranges of acolinearity. The corresponding plots for background are also shown.

Signal and Standard Model Monte Carlos are used to construct one dimensional reference histograms for momentum. The signal histograms are constructed for the grid of points in the (m, Δm) plane for which signal Monte Carlo has been generated, as defined in section 5.3. Each of the signal momentum distributions and the background distribution is subdivided into the following 3 ranges of acolinearity (in radians): $0 \leq \theta_{acol} < 0.8, 0.8 \leq \theta_{acol} < 1.6$ and $1.6 \leq \theta_{acol} < \pi$. Each of these distributions is then further subdivided according to whether the observed lepton is the higher or lower momentum lepton in the event.

For the searches in which the final state particles can be the decay products of taus (staus, charginos and charged Higgs bosons), each momentum probability distribution must be further subdivided, as the momentum spectrum depends on the lepton identification. One momentum probability distribution is constructed for the case in which the observed lepton is identified as e or μ, and another for the case in which the observed lepton is identified as a hadronically decaying tau, or is unidentified.

There are thus a total of 6 momentum reference histograms for a given m and Δm in the selectron and smuon analyses, and 12 such histograms in the stau, chargino and charged Higgs boson analyses. Probabilities $P_S(x_i)$ and $P_B(x_i)$ for a given event are found by reading from the appropriate reference histograms.

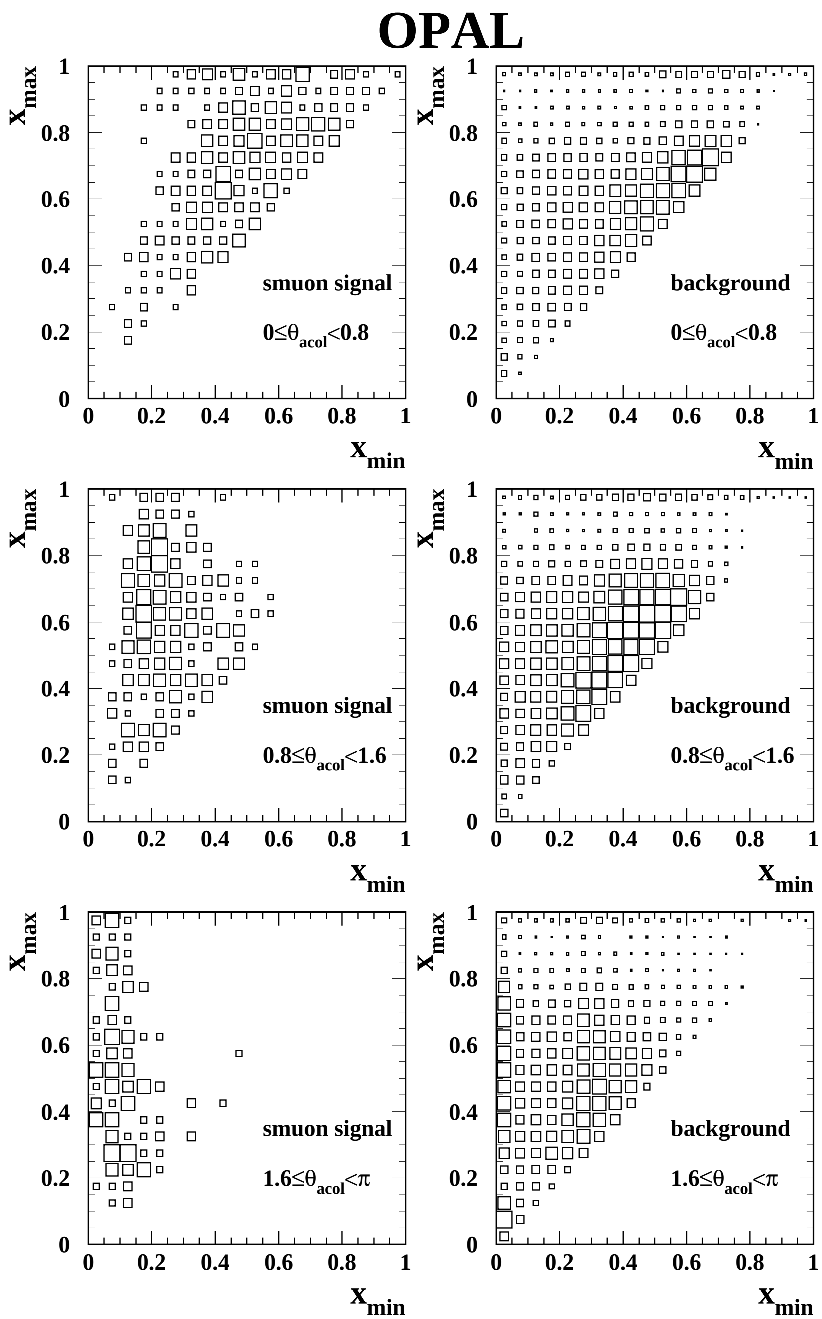

Figure 6.1: *Distributions in the (x_{min}, x_{max}) plane, where x_{min} and x_{max} are the momenta of the higher and lower momentum lepton, respectively, scaled by the beam energy, for three ranges of acolinearity (shown in radians). The distributions are shown for a smuon signal with m=45 GeV, Δm=45 GeV (left), and for Standard Model Monte Carlo (right).*

6.4 The Acolinearity Likelihood Variable

For signal, the distribution of the acolinearity angle varies with m and Δm. For low parent particle mass, the Lorentz boost results in a tendency for the leptons to be in the directions of the parent particles, resulting in the acolinearity being peaked towards low values, whereas for high mass, the parent particles are produced close to being at rest, and the leptons have no preferred direction. For background, the V-A nature of W decay leads to a forward peaking of the lepton decay angle in the W rest frame, and as a result, the acolinearity distribution is peaked towards low values.

Figure 6.2 shows some examples of acolinearity distributions for signal, which can be compared to the distributions for background and data shown in Figure 5.3(c).

The use of the acolinearity as a likelihood variable is complementary to its use in defining the momentum probability, in that the masses for which it offers the greatest discrimination as a likelihood variable are the masses where the gain in distinguishing power described in Section 6.3 is small, and vice versa.

6.5 The $-q\cos\theta$ Likelihood Variable

The production angle of the W^- in W^+W^- production is strongly forward peaked due to the dominance of the neutrino exchange amplitude (Figure 5.1(b)). This effect, combined with the forward peaking of the lepton in the W rest frame referred to in Section 6.4, leads to the distribution of the quantity $-q\cos\theta$, where q and θ are the charge and production angle of an observed lepton, being forward peaked.

Smuons, staus and charged Higgs bosons on the other hand are scalar particles produced in the s-channel, and the production angle is symmetric about $|\cos\theta| = 0$. Also the decay lepton is isotropic in the parent particle rest frame. The $-q\cos\theta$

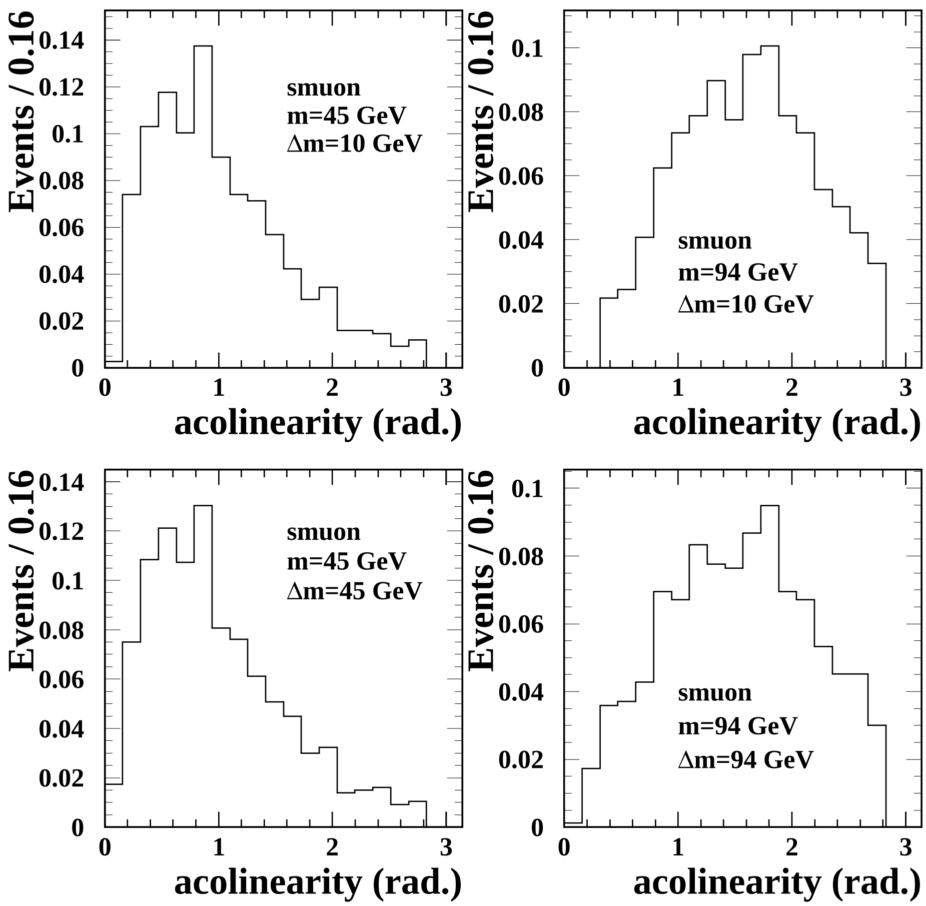

Figure 6.2: *Distributions of acolinearity (in radians) for four example smuon signals.*

distribution is therefore symmetric about and peaked towards $|\cos\theta| = 0$.

The distribution of $-q\cos\theta$ for the Standard Model background and data at $\sqrt{s} = 189$ GeV is compared to the distribution for a smuon signal (averaged over all m and Δm [1]) in figure 5.3(b).

This variable is not used in the likelihood calculation for selectrons or charginos because these particles can be produced via t-channel neutralino exchange and sneu-

[1] The dependence of this distribution on m and Δm is small

trino exchange, respectively, in addition to s-channel production. This results in the expected $-q\cos\theta$ distribution of selectrons and charginos being model-dependent and, for regions of parameter space in which the t-channel exchange is dominant, similar to that of the $\mathrm{W}^+\mathrm{W}^-$ background.

6.6 The Lepton Type Likelihood Variable

A value is assigned to the lepton type variable according to which types of lepton are identified in the event. There are nine possible values, corresponding to the nine event types listed in table 5.2.

Distributions of the lepton type variable for example stau signals at $\sqrt{s} = 189$ GeV are compared with background and data in figure 6.3. It can be seen from these plots that a fairly large amount of discrimination is possible. The most probable value for the background is 4, corresponding to an event of type $\mathrm{e}^{\pm}\mu^{\mp}$. This value has low probability for the signal. Conversely, a signal event has a high probability of having value 3, 5 or 6, corresponding to event types $h^{\pm}h^{\mp}$, $\mathrm{e}^{\pm}h^{\mp}$ and $\mu^{\pm}h^{\mp}$, whereas these (particularly $h^{\pm}h^{\mp}$) are less dominant for background.

For the selectron (smuon) analysis a cut is applied at the same time as the general selection, requiring at least one electron (muon) and no muons (electrons), reducing the background by about 2/3 (depending on slepton type and $\sqrt{s}$) with negligible loss of efficiency. With this cut applied, there are only three possible values of the lepton type variable.

6.7 L_R and L_B Distributions

For each search channel, reference histograms are constructed for each of the likelihood variables at each point in m and Δm for which signal Monte Carlo has been

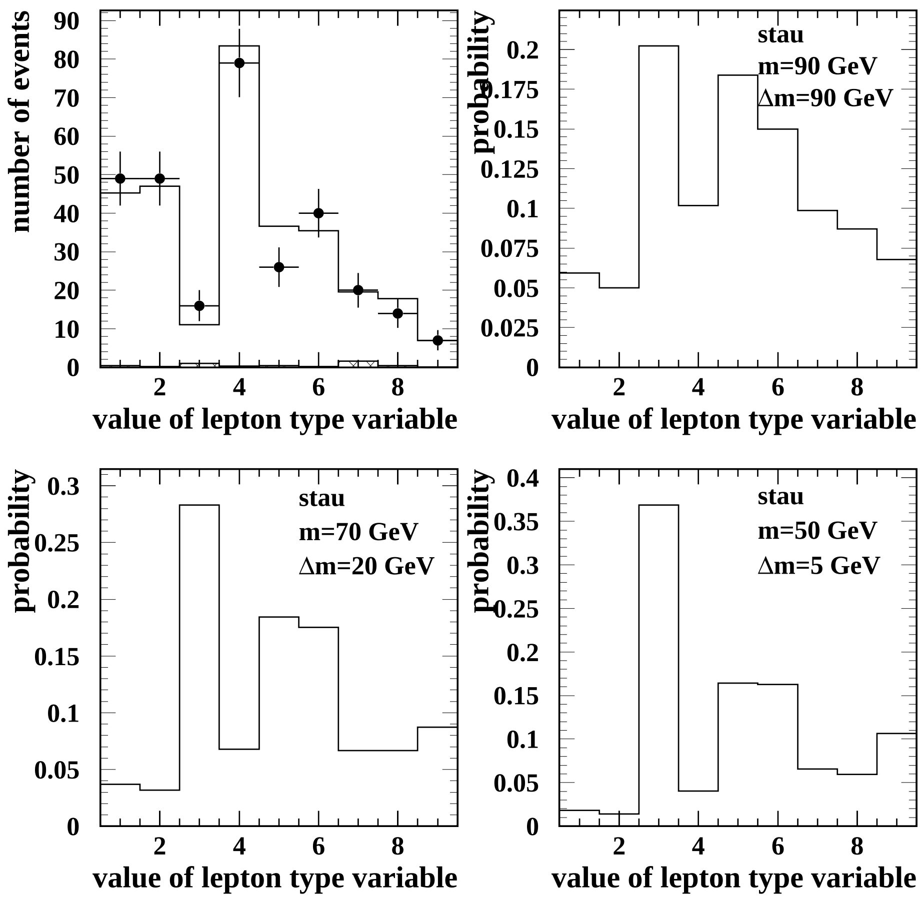

Figure 6.3: *Distribution of the lepton type variable for Standard Model Monte Carlo and data (top left). The values 1 to 9 correspond to the nine event types listed in table 5.2. The data are shown as the points with error bars. The Monte Carlo prediction for 4-fermion processes with genuine prompt missing energy and momentum ($\ell^+\nu\,\ell^-\overline{\nu}$) is shown as the open histogram and the background, arising mainly from processes with four charged leptons in the final state, is shown as the shaded histogram. Three examples of expected signal distributions for staus are also shown.*

generated. A smoothing algorithm [51] is applied to the histograms to reduce the effects of statistical fluctuations. This is important because statistical fluctuations in the reference histograms can lead to a degradation of the actual search sensitivity (because the signal being searched for is not being accurately represented), as well as the possibility of overestimating the expected search sensitivity (by possibly indicating a greater amount of discrimination between the signal and background distributions than there actually is). An input parameter of the smoothing algorithm is the sensitivity to statistical fluctuations. The value chosen for this parameter is the highest value for which the smoothed distribution is single peaked. Because the background distributions are composed of different Standard Model processes, two peaks are allowed in these distributions.

For a particular point in m and Δm for a given search channel, L_R can be calculated for a given event according to equations 6.1 to 6.3, using the background reference histograms and the appropriate signal reference histograms to obtain the values of $P_B(x_i)$ and $P_S(x_i)$ for each variable. Distributions of L_R are constructed at each (m, Δm) point considered, for signal Monte Carlo, Standard Model Monte Carlo and data.

Some example L_R distributions for signal Monte Carlo, Standard Model Monte Carlo and data are shown in Figure 6.4. It can be seen that the data is in good agreement with the Standard Model expectation. The plots shown in Figure 6.4 do not include events with $L_R = 0$. The fractions of Standard Model events with $L_R = 0$ in the analyses corresponding to plots (a), (b), (c) and (d) are 49%, 8%, 55% and 0.3%, respectively. There is considerable variation in the shapes of the L_R distributions with m and Δm.

A check of consistency between data and the Standard Model can be performed without reference to a particular signal by comparing the L_B distributions for data and Standard Model. Figure 6.5(a) shows the L_B distributions for the Standard Model (histogram) and data (points) for events passing the general selection. All

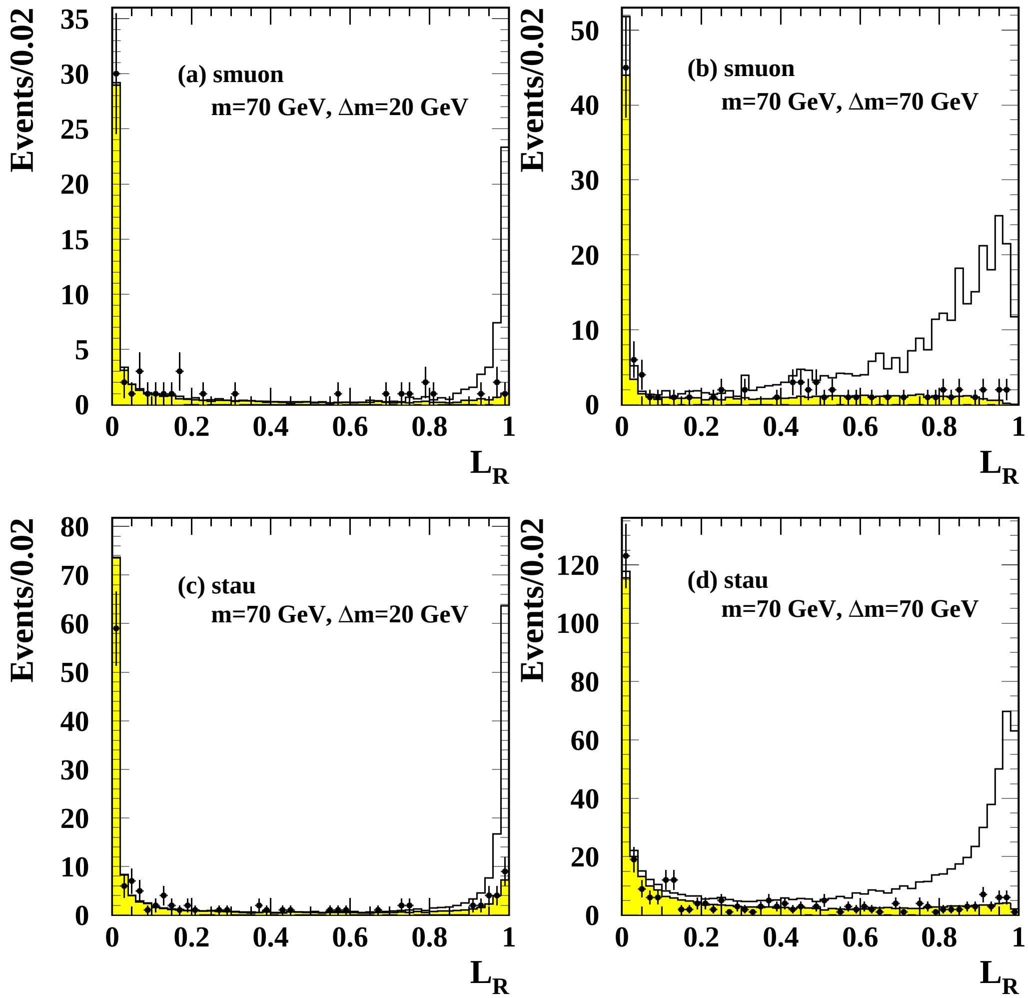

Figure 6.4: *Example distributions of the relative likelihood, L_R, for data (points with error bars), Standard Model Monte Carlo (shaded histogram), and Standard Model Monte Carlo plus signal Monte Carlo with arbitrary normalization (open histogram), for two example points in the (m, Δm) plane for the smuon and stau analyses at $\sqrt{s}$ = 189 GeV.*

the likelihood variables are used. Figures 6.5(b) and (c) show the same information after making the initial lepton identification requirements given in Section 6.6 for the selectron and smuon searches, respectively. In Figure 6.5(b), only the variables used in the selectron analysis are used. In each of the plots, the secondary peak at high L_B corresponds to events which have only one identified lepton and therefore fewer variables entering the likelihood[2]. In all three plots, the data is in good agreement with the Standard Model.

[2]This effect cancels when the likelihood ratio L_R is calculated because the events will have high L_S for the same reason.

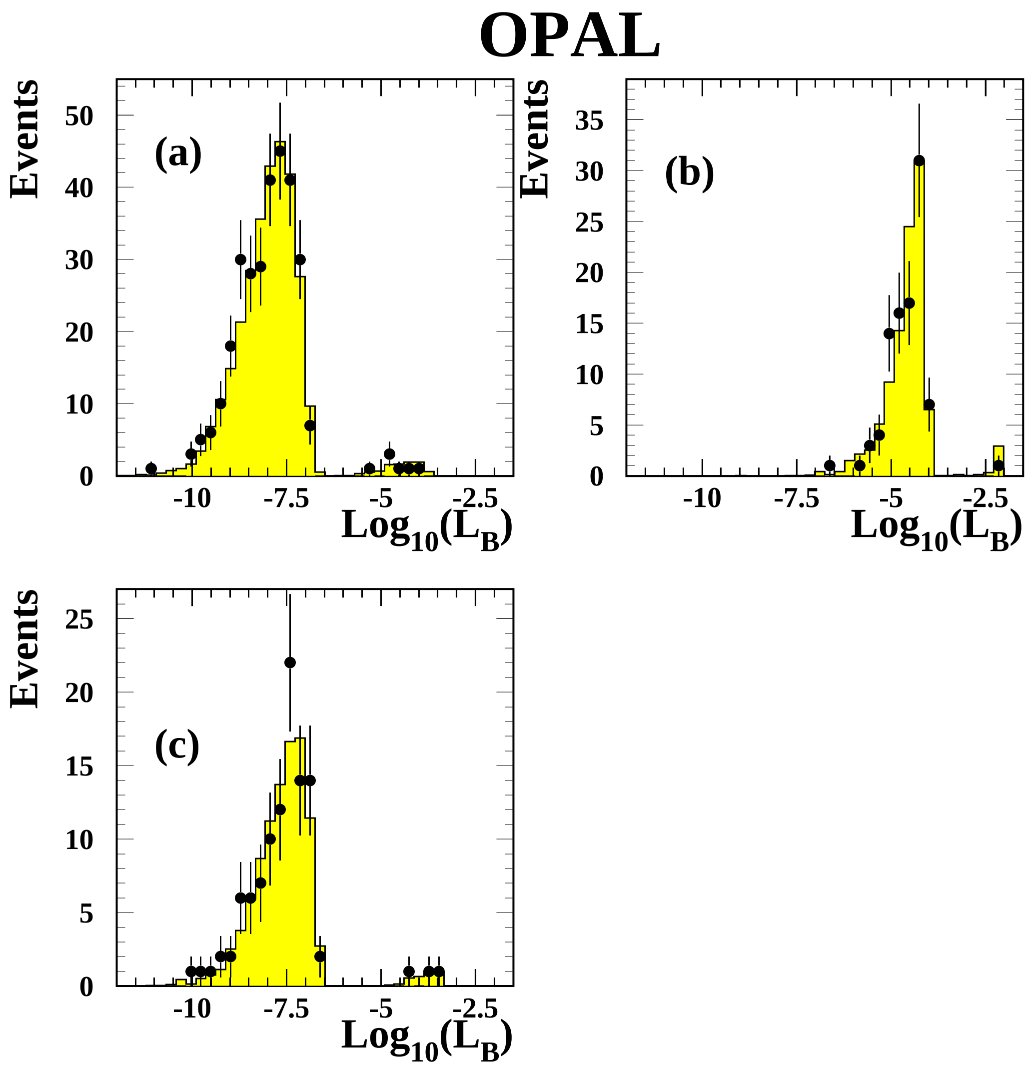

Figure 6.5: *(a) Distribution of the background likelihood, L_B, for Standard Model Monte Carlo (shaded histogram) and data (points with error bars) for events passing the general selection at $\sqrt{s}$ = 189 GeV, using all the likelihood variables. (b) and (c) show the same information after making the initial lepton identification requirements given in Section 6.6 for the selectron and smuon searches respectively. In (b), only the variables used in the selectron analysis are used.*

Chapter 7

Calculation of Cross-Section Limits for New Particle Production

7.1 Introduction

It can be concluded from Chapters 5 and 6 that the numbers and global properties of the observed events are in good agreement with the Standard Model. However, in order to be sensitive to the presence of specific signals which may have small cross-sections and therefore not be apparent in figure 6.5, it is necessary to scan through all kinematically accessible values of m and Δm for each search channel, quantifying the extent to which the observed data is in agreement with the Standard Model in each case.

For a given point in the (m, Δm) plane for a given search channel, the upper limit at 95% confidence level, σ_{95}, on the product of the cross-section for the pair production of a new particle times the branching ratio squared for the decay mode searched for, $\sigma.BR^2$, is calculated. Consistency with the Standard Model is verified by comparing the value of σ_{95} for the observed data with that expected from the Standard Model, as described in Section 8.3. The present chapter describes the method for calculating σ_{95} at any point in the $(m, \Delta m)$ plane.

In our paper publishing the results of the analysis of the data collected at $\sqrt{s} =$ 161, 172 and 183 GeV [50], the value of σ_{95} for a particular point in the $(m, \Delta m)$ plane was calculated by finding an optimized cut on the value of L_R for each centre-of-mass energy, and applying this cut to signal Monte Carlo, Standard Model Monte Carlo and data. The resulting signal efficiencies, expected backgrounds and numbers of candidates were then used to calculate cross-section limits, using a method based on Poisson statistics to combine the information. Details of this cut based method, together with tables of signal efficiencies, expected backgrounds and numbers of candidates for the $\sqrt{s} = 189$ GeV data, are given in appendix A.

In this analysis, an extended maximum likelihood calculation is used as an alternative way to determine the cross-section limits. In this method, no cut is applied on L_R. Information contained in the L_R values of each individual candidate event, and in the shapes of the L_R distributions for signal and background are used as input to the limit calculation, rather than the numbers of events passing a cut. In this way, considerably more of the available information is used.

The advantage of a cut free method can be seen by considering, for example, a case where there is an excess of candidates passing a cut on L_R. The information about whether the events all lie close to the cut, or whether they are clustered towards L_R=1 (suggesting the presence of a signal) is not used. The use of the additional information makes the analysis more sensitive for discovery, and at the same time is able to set more stringent limits in the absence of signal. The expected sensitivity (i.e. the expected upper limit on $\sigma.BR^2$) is improved by as much as 20%, depending on m and Δm, using this technique.

7.2 Extended Maximum Likelihood Technique

The upper limit on $\sigma.BR^2$ at 95% confidence level, σ_{95}, is calculated by forming a likelihood, $L(\sigma_s)$, of the set of L_R values for the data being consistent with the expected L_R distribution for Standard Model plus a signal produced with $\sigma.BR^2{=}\sigma_s$. σ_{95} is the value of σ_s below which 95% of the area under the likelihood function lies (Figure 7.1).

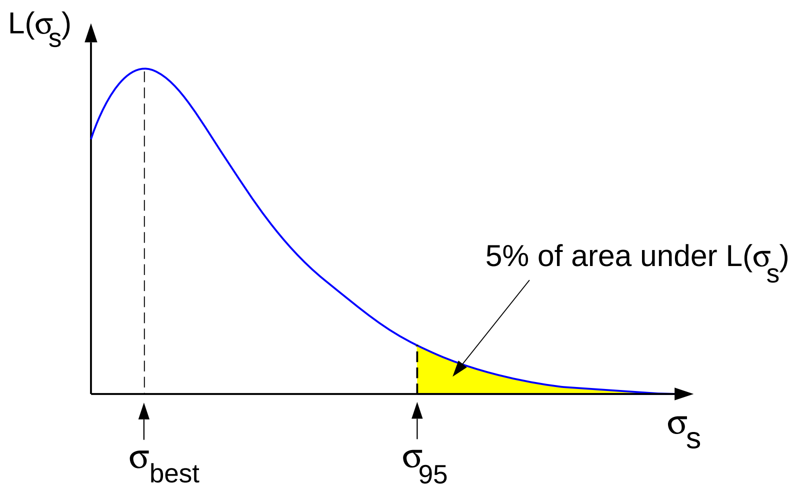

Figure 7.1: *Definition of σ_{95} in terms of the likelihood function.*

7.3 The Likelihood Function

Extended maximum likelihood combines standard maximum likelihood with the Poisson probability of observing N candidate events when ν are expected:

$$L = \frac{e^{-\nu}\nu^N}{N!}\prod_{i=1}^{N} P(L_{R_i}; B, S), \tag{7.1}$$

where $P(L_{R_i}; B, S)$ is the probability of event i having $L_R = L_{R_i}$, given L_R distributions B and S for background and signal.

Dropping the constant $N!$, this can be re-written:

$$\ln L = -\nu + N \ln \nu + \sum_{i=1}^{N} \ln P(L_{R_i}; B, S) \tag{7.2}$$

$$\ln L = -\nu + \sum_{i=1}^{N} \ln[Q(L_{R_i}; B, S)] \tag{7.3}$$

where Q is identical to P but normalized to ν instead of 1 ($Q = \nu P$).

The expected number of candidates ν is given by:

$$\nu = \mu_B + \epsilon \mathcal{L} \omega \sigma_s, \tag{7.4}$$

where μ_B is the expected number of Standard Model events with non-zero L_R passing the general selection (similarly, N is the number of data candidates with $L_R \neq 0$ [1]), ϵ is the signal selection efficiency of the general selection, $\mathcal{L}$ is the experimental luminosity and ω is a weight factor which takes into account that the expected production cross-section varies with $\sqrt{s}$, but the limit on the observed cross-section is quoted at $\sqrt{s} = 189$ GeV.

$$\omega_i = \frac{\sigma_i}{\sigma_{189}}, \tag{7.5}$$

where σ_{189} is the expected cross-section for $\sqrt{s} = 189$ GeV and σ_i is the expected cross-section for the i^{th} value of $\sqrt{s}$. For scalar particles, for example sleptons, we assume that the expected cross-section varies as β^3/s. For spin $\frac{1}{2}$ particles, for example charginos, we assume that the expected cross-section varies as β/s.

The function Q is the probability of event i having $L_R = L_{R_i}$, given L_R distributions B and S for background and signal, normalized to ν. This is given by:

$$Q = \mu_B B(L_{R_i}) + \epsilon \mathcal{L} \omega \sigma_s S(L_{R_i}), \tag{7.6}$$

[1] For simplicity, only candidate events with $L_R \neq 0$ are considered in the calculation, because $S(L_R = 0) = 0$, and therefore, from equation 7.7, the inclusion of events with $L_R = 0$ affects only the normalisation of L(σ_s) and does not therefore affect the value of σ_{95}.

where the functions B and S, formed using background and signal Monte Carlo respectively, are normalized to 1.

Hence the likelihood function is given by:

$$\ln L(\sigma_s) = -(\mu_B + \epsilon\mathcal{L}\omega\sigma_s) + \sum_{i=1}^{N} \ln[\mu_B B(L_{R_i}) + \epsilon\mathcal{L}\omega\sigma_s S(L_{R_i})]. \tag{7.7}$$

7.4 Limit Calculation

For data at a single centre-of-mass energy, the upper limit on $\sigma.BR^2$ at 95% confidence level is the value of σ_{95} which satisfies:

$$0.95 = \frac{\int_0^{\sigma_{95}} L(\sigma_s)\mathrm{d}\sigma_s}{\int_0^{\infty} L(\sigma_s)\mathrm{d}\sigma_s}. \tag{7.8}$$

The generalization to N_{ECM} values of $\sqrt{s}$ is:

$$0.95 = \frac{\int_0^{\sigma_{95}^{189}} \prod_{i=1}^{N_{ECM}} L_i(\sigma_s^{189})\mathrm{d}\sigma_s^{189}}{\int_0^{\infty} \prod_{i=1}^{N_{ECM}} L_i(\sigma_s^{189})\mathrm{d}\sigma_s^{189}}. \tag{7.9}$$

where σ_s^{189} is the cross-section at $\sqrt{s} = 189$ GeV.

7.5 Verification of the Method

The technique used to calculate limits was tested using a toy Monte Carlo to simulate data sets for an ensemble of simulated experiments in which a signal is present with cross-section σ_s. The total number of candidates was drawn from a Poisson distribution with mean ν and for each candidate, a value of L_R was assigned, chosen randomly according to the sum of the expected L_R distributions for background and signal with cross-section σ_s.

σ_{95} was calculated for 500 simulated experiments. This was done using smuon signals at all m and Δm for which Monte Carlo has been generated, for 189 GeV separately and for 183 GeV and 189 GeV combined, and for a number of values of σ_s. In all cases, 95% of the 500 σ_{95} values were found to be greater than the true cross-section σ_s, to within the statistical error expected from the finite number of simulated experiments.

As a further test, the best estimate of the signal cross-section, σ_{best}, was calculated for each simulated experiment. This is the value of σ_s at which the likelihood function $L_i(\sigma_s)$ peaks (see Figure 7.1). The σ_{best} distribution from the 500 simulated experiments was in all cases found to peak at the true cross-section.

7.6 Limit Calculation at an Arbitrary Point in m and Δm

Monte Carlo signal events are available only at certain particular values of m and Δm, with a typical spacing of about 5 GeV. The signal Monte Carlo mass grids for the different search channels are defined in Section 5.3. In order to calculate σ_{95} at an intermediate point in m and Δm, it is necessary to be able to calculate L_R at that point for a given event, which requires the existence of reference histograms for the likelihood variables for any m and Δm.

7.6.1 Interpolation of the Reference Histograms

In regions of the $(m, \Delta m)$ plane in which the momentum distributions change slowly with m and Δm, it is sufficient to perform a bin by bin 2-dimensional linear interpolation of the momentum reference histograms at the four nearest signal Monte Carlo grid points in order to construct the histogram at an intermediate point. However, this does not work if the distributions between which the interpolation is performed do not overlap to a large degree. This is true for the momentum reference histograms at low Δm, particularly for high m, when the distributions are very narrow. It is important that the interpolation is done correctly, otherwise the analysis is not sensitive to signals which have momentum distributions significantly different to the distributions at the grid points. A more sophisticated algorithm, described in Appendix B, has therefore been developed which constructs reference histograms at any intermediate value of m and Δm, given the histograms at the four nearest signal Monte Carlo grid points, assuming a linear variation in the shape of the histograms with m and Δm. The procedure has been tested by reconstructing histograms at gridpoints using the histograms at adjacent gridpoints. Some examples of such a test are shown in Figure 7.2. It is important to note that these tests represent worse than worst case scenarios because the interpolations shown are performed between points which are separated by twice the grid spacing. Interpolations between adjacent gridpoints can be expected to give a much better result, and indeed the spikes seen in the interpolated histograms of Figure 7.2 do not, in general, occur in actual interpolations.

The same interpolation algorithm is applied to the acolinearity reference histograms. The lepton type variable histograms are interpolated by applying a 2-dimensional linear interpolation to each bin. The dependence of the $-q\cos\theta$ distribution on m and Δm is very small, and the signal reference histogram for this variable at any m and Δm is taken to be the normalized sum of the distributions for all m and Δm [2].

7.6.2 Construction of L_R distributions at any m and Δm

The L_R distributions do not have the simple single peaked structure of the smoothed reference histograms and can contain substructures due to the discreet nature of the

[2] It was decided that this approximation provides a more accurate description of the signal than the histograms at the individual gridpoints, since these can have unacceptably low statistics (particularly at low Δm) for such a broad distribution.

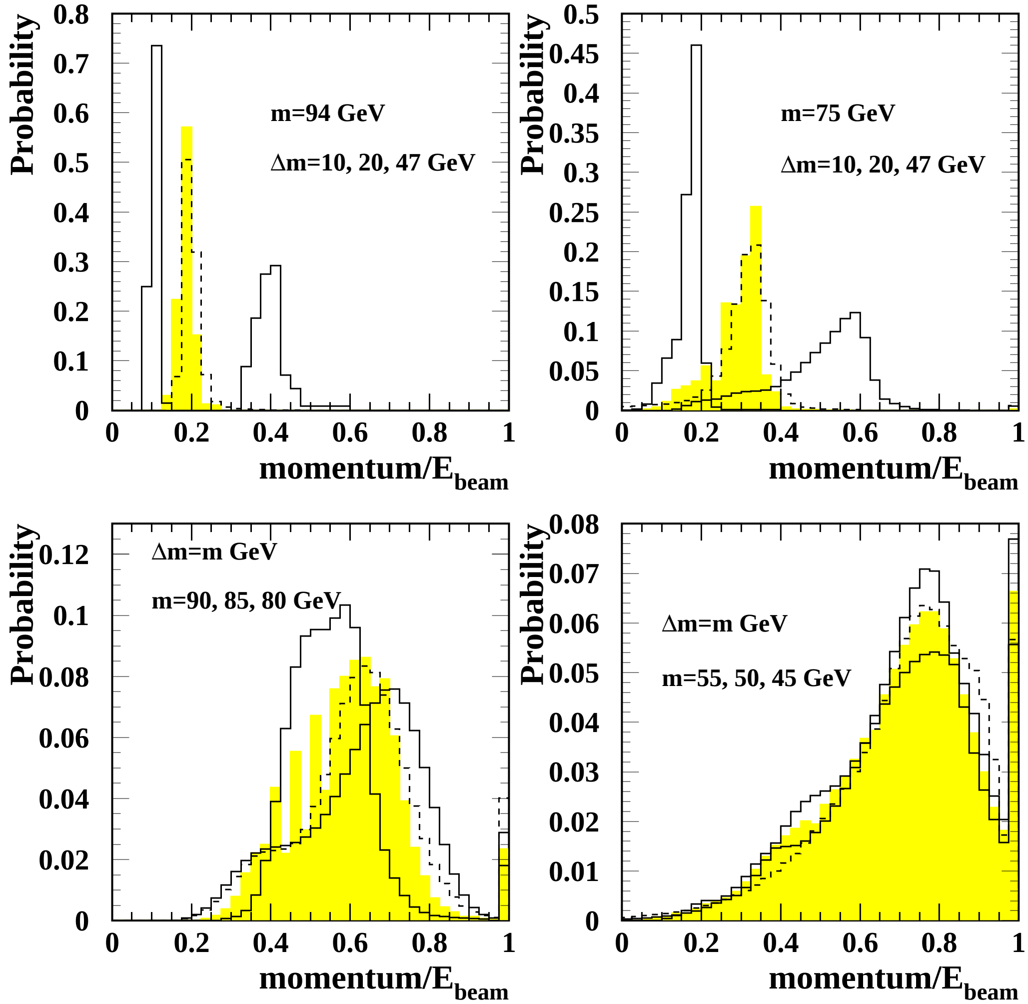

Figure 7.2: *Tests of the interpolation of momentum reference histograms. In each plot, the shaded histogram is the result of an interpolation between the two solid histograms. The dashed histogram is the actual Monte Carlo distribution for the intermediate point. The solid and dashed histograms have had the smoothing algorithm applied (Section 6.7). All plots show smuon momentum reference histograms for the higher momentum lepton, for* $\theta_{acol} < 0.8$ *rad, at* $\sqrt{s} = 189$ *GeV. The values of* m *and* Δm *for the histograms are shown.*

lepton type likelihood variable. As a result, the simple interpolation technique used for the reference histograms cannot be applied, and the L_R distributions must be constructed using Monte Carlo, for all m and Δm for which σ_{95} is to be calculated.

For a given point in m and Δm, the L_R distributions for signal and background Monte Carlo and the data L_R values are calculated using the interpolated reference histograms. The construction of the signal L_R distributions is complicated by the fact that signal Monte Carlo is available only at the grid points. Signal Monte Carlo at an arbitrary point (m, Δm) is simulated using signal Monte Carlo events at the nearest grid point, using the interpolated reference histograms, as described in Appendix C. The resulting signal L_R distributions are observed to vary smoothly as a function of m and Δm, between the Monte Carlo grid points.

7.6.3 Smoothing of the L_R Distributions

The effects of statistical fluctuations in the L_R distributions are reduced using the same smoothing algorithm as applied to the reference histograms (Section 6.7). An optimal value for the sensitivity to statistical fluctuations is chosen by considering the number of peaks in the smoothed distribution and the χ^2 of the fit. The effect of smoothing is illustrated in Figure 7.3 for an example background and an example signal L_R distribution. The fact that the statistical fluctuations are smoothed out presents the option of using narrow bins. The use of fine binning in the distributions in Figure 7.3 allows the structure in the distributions at very high and very low L_R to be retained.

The sensitivity of the value of σ_{95} to the precise shapes of the smoothed L_R distributions was investigated by setting the value of the sensitivity parameter of the smoothing algorithm to a value slightly higher than and slightly lower than the value chosen to be optimal. This results in smoothed histograms that are slightly different in shape to the optimally smoothed histogram. In each case, the values of

σ_{95} were calculated, and this was done for a range of points in the $(m, \Delta m)$ plane. The values of σ_{95} were generally found to vary very little and the variation was always less than about 5%.

7.6.4 Efficiency Interpolation

The remaining input to the limit calculation is the signal efficiency of the general selection, obtained at intermediate values of m and Δm by 2-dimensional linear interpolation.

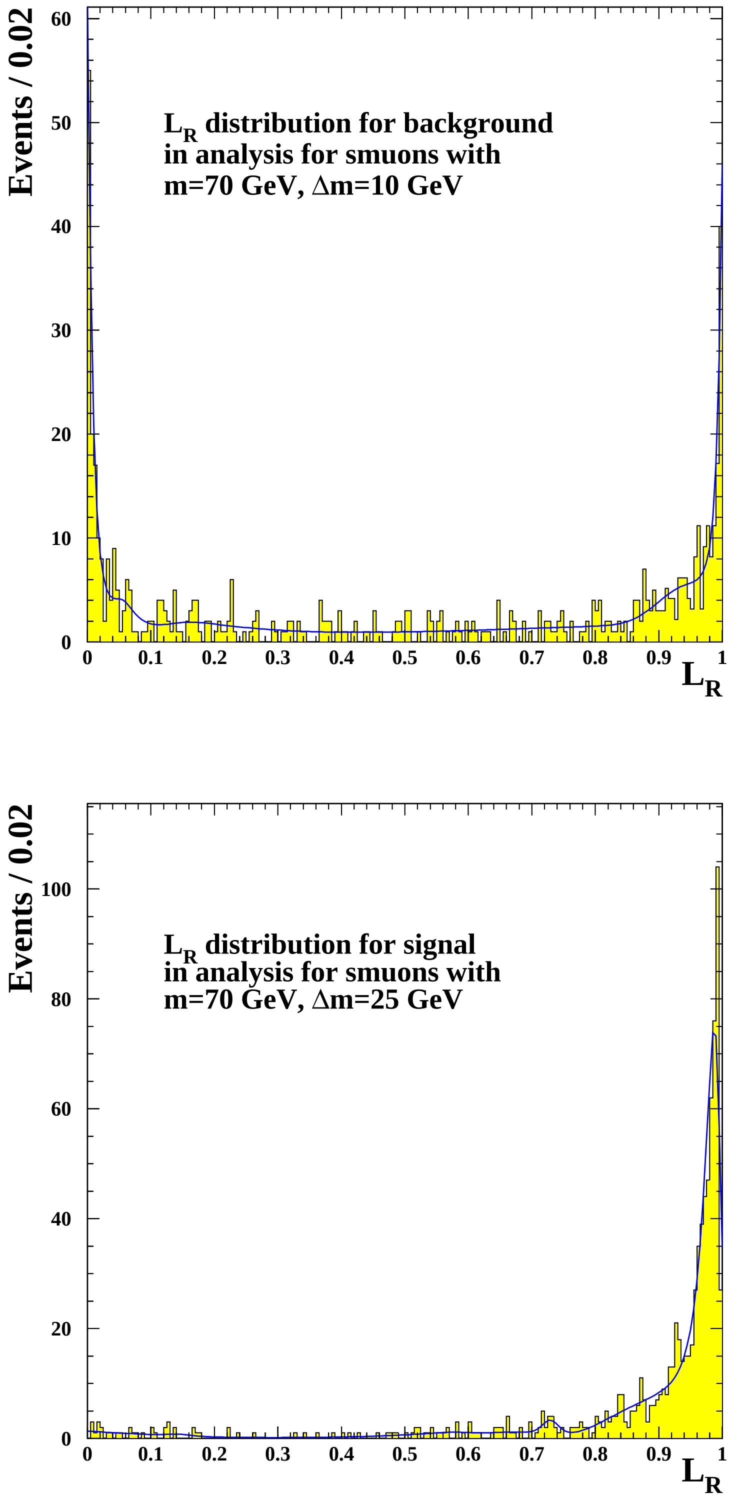

Figure 7.3: *Illustration of the smoothing of L_R distributions. The histogram shows the unsmoothed distribution and the line shows the smoothed function.*

Chapter 8

New Particle Search Results

In this chapter, limits are presented on the pair production of charged scalar leptons, leptonically decaying charged Higgs bosons and charginos that decay to produce a charged lepton and invisible particles.

8.1 Systematic Uncertainties

In setting limits the Monte Carlo statistical errors and other systematics are taken into account according to the method described in [52].

In addition to the Monte Carlo statistical error on the signal efficiency, a 10% systematic error on the estimated selection efficiency is assigned to take into account uncertainties in trigger efficiency (less than 1%), detector occupancy (less than 1%), lepton identification efficiency ($\sim 1\%$), luminosity measurement (0.21% [53]), the interpolation procedure (less than 5%, see section 7.6.3), and deficiencies in the Monte Carlo generators (5%) and the detector simulation. In this analysis, detailed checks of data quality have been performed and good agreement between data and Standard Model Monte Carlo has been observed. Other Standard Model analyses have also shown excellent agreement [53, 54]. The value of the systematic error is chosen to be conservative, as the cross-section limits are not sensitive to the size of the error.

An additional systematic error in the stau analysis is the effect of tau polarization in the modeling of the stau signal. It is possible for the tau produced in stau decay to have any polarization value, $P(\tau)$, in the range [-1,1], depending on the stau mixing angle and the nature of $\tilde{\chi}_1^0$ [55]. Since the tau polarization has a strong effect on the pion momentum spectrum in the tau rest frame, it is important to investigate whether or not there is a significant effect on the stau cross-section limits. SUSYGEN was used to generate stau Monte Carlo for $P(\tau)$=+1, 0 and -1. The full set of reference histograms were generated in each case and comparisons show only a small shifting of the distributions. Figure 8.1 shows lepton momentum distributions for leptons identified as hadronically decaying taus, at four example points in the (m, Δm) plane, for the three different values of $P(\tau)$. The expected limit on $\sigma.BR^2$ was calculated for all m and Δm at which signal Monte Carlo was generated, for each of the three tau polarizations, but using the reference histograms for $P(\tau)$=0. In this way, one can determine the amount by which the expected limit is overestimated or underestimated if a polarization of zero is assumed when the true polarization is $+1$ or -1. The size of this effect was found to vary with m and Δm, but to be always less than about 5% , and so is included in the 10% systematic error.

At high values of Δm the dominant background to the searches for new physics results from W^+W^- production. High statistics Monte Carlo samples for this process are available that describe well the OPAL data [54]. In addition to the Monte Carlo statistical error, a 10% systematic error on the estimated background is assigned to take into account uncertainties in the shapes of the L_R distributions and reference histograms, and in the interpolation procedure, and deficiencies in the Monte Carlo detector simulation. At low values of Δm the dominant background results from

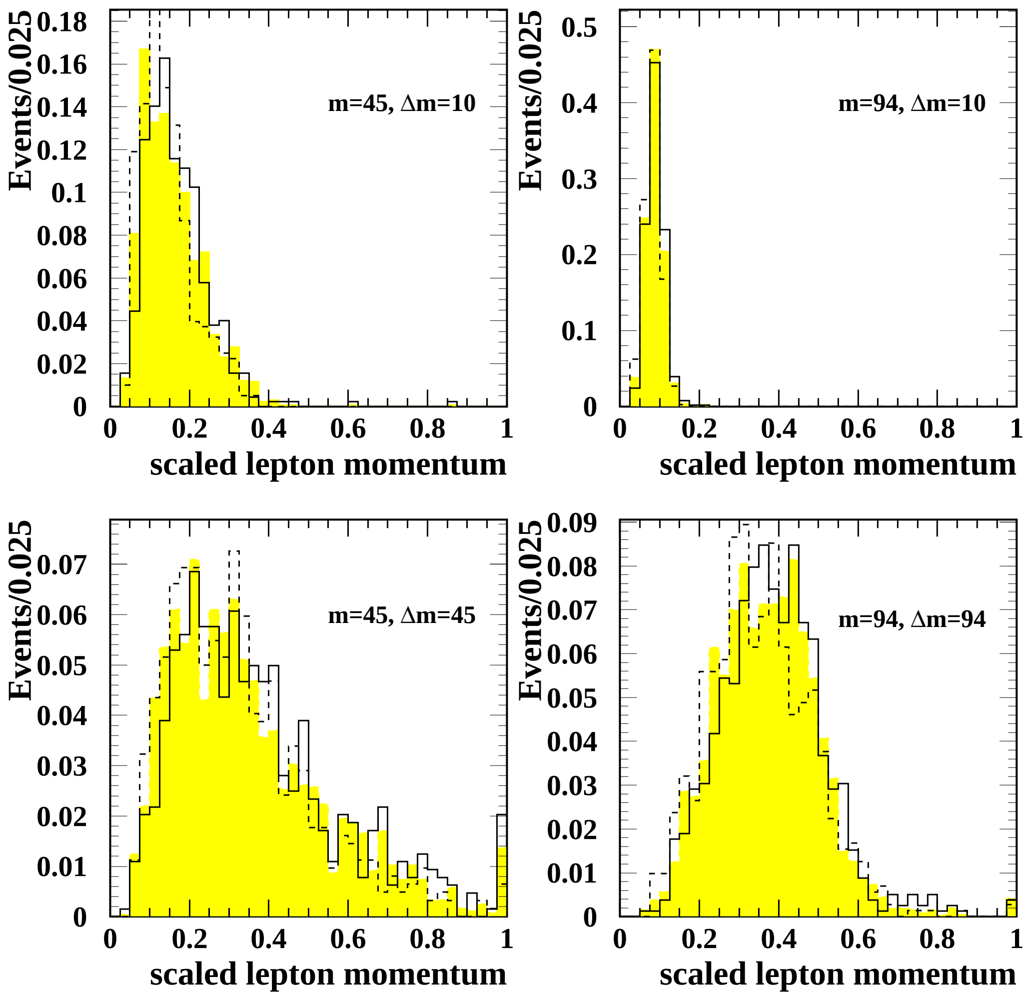

Figure 8.1: *Lepton momentum distributions for stau Monte Carlo with tau polarizations of +1 (solid line), -1 (dashed line) and zero (shaded histogram) for four points in the $(m, \Delta m)$ plane . All plots show momentum reference histograms for the higher momentum lepton, for $0.8 < \theta_{acol} < 1.6$ rad, for leptons identified as hadronically decaying taus, at $\sqrt{s} = 189$ GeV.*

$e^+e^-\ell^+\ell^-$ events. The background uncertainty at low Δm is dominated by the limited Monte Carlo statistics; the uncertainty is typically 20–80% at low Δm.

8.2 Limits on Production Cross-section Times Branching Ratio Squared

Limits on the production cross-section times branching ratio squared for new physics processes are now presented in a manner intended to minimize the number of model assumptions. The 95% CL upper limit on new particle production at $\sqrt{s} = 189$ GeV, obtained by combining the data at $\sqrt{s} = 189$ GeV and $\sqrt{s} = 183$ GeV is calculated at each kinematically allowed point on a 0.5 GeV by 0.5 GeV grid of m and Δm, using the L_R distributions for signal and background, the L_R values of the data events, and the efficiency of the general selection at that point as input. The data at the two centre-of-mass energies 183 and 189 GeV are combined using the assumption that the cross-section varies as β^3/s for sleptons and β/s for charginos. The chosen functional forms are used for simplicity in presenting the data and represent an approximation, particularly for processes in which t-channel exchange may be important, that is, selectron pair and chargino pair production. In these cases the cross-section dependence on centre-of-mass energy is model dependent, depending on the mass of the exchanged particles and the couplings of the neutralinos and charginos.

Upper limits at 95% CL on the selectron pair cross-section at $\sqrt{s} = 189$ GeV times branching ratio squared for the decay $\tilde{e}^- \rightarrow e^- \tilde{\chi}^0_1$ are shown in Figure 8.2 as a function of selectron mass and lightest neutralino mass. These limits are applicable to $\tilde{e}^+_L\tilde{e}^-_L$ and $\tilde{e}^+_R\tilde{e}^-_R$ production. The corresponding plots for the smuon and stau pair searches are shown in Figures 8.3 and 8.4, respectively. The limit is typically of order 70 fb, which is consistent with the approximate calculation $\sigma_{95} = N^{95}/\epsilon\mathcal{L}$, where the upper limit on the number of signal events at 95% CL, N^{95}, calculated as described in Appendix A, has a value of at least 3 but more typically 10, the efficiency, ϵ, is typically 70% , and the total integrated luminosity, $\mathcal{L}$, is 237.4 pb^{-1}. The limit increases sharply as Δm approaches zero because the efficiency decreases to zero at very low Δm. The limit tends also to increase as Δm increases due to the increasing background from Standard Model $\ell^+\nu\,\ell^-\overline{\nu}$ events from W pairs.

Note that if the LSP is an effectively massless gravitino, $\tilde{G}$, as would be consistent with the gauge mediated supersymmetry breaking scenario (see Section 4.5), then for prompt slepton decays to a lepton and a gravitino the experimental signature would be the same as that for $\tilde{\ell}^-\!\rightarrow\!\ell^-\tilde{\chi}^0_1$ with a massless neutralino. In this case the limits given in Figures 8.2 – 8.4 for $m_{\tilde{\chi}^0_1} = 0$ may be interpreted as limits on the decay $\tilde{\ell}^- \rightarrow \ell^-\tilde{G}$.

The upper limit at 95% CL on the chargino pair production cross-section times branching ratio squared for the decay $\tilde{\chi}^\pm_1 \rightarrow \ell^\pm\tilde{\nu}_\ell$ (2-body decay) is shown in Figure 8.5. The limit has been calculated for the case where either the three sneutrino generations are mass degenerate, or only one flavour is kinematically allowed. The upper limit at 95% CL on the chargino pair production cross-section times branching ratio squared for the decay $\tilde{\chi}^\pm_1 \rightarrow \mathrm{W}^\pm\tilde{\chi}^0_1 \rightarrow \ell^\pm\nu\tilde{\chi}^0_1$ (3-body decay) is shown in Figure 8.6.

The upper limit at 95% CL on the charged Higgs boson pair production cross-section times branching ratio squared for the decay $\mathrm{H}^\pm \rightarrow \tau^\pm\nu_\tau$ is shown as a function of m_{H^+} as the solid line in Figure 8.7. The limit is obtained by combining the 183 and 189 GeV data-sets assuming the m_{H^+} and $\sqrt{s}$ dependence of the cross-section predicted by PYTHIA, which takes into account the effect of initial state radiation. The dashed line in Figure 8.7 shows the prediction from PYTHIA at $\sqrt{s} = 189$ GeV for a 100% branching ratio for the decay $\mathrm{H}^\pm \rightarrow \tau^\pm\nu_\tau$. With this assumption a lower limit is set at 95% CL on m_{H^+} of 82.8 GeV.

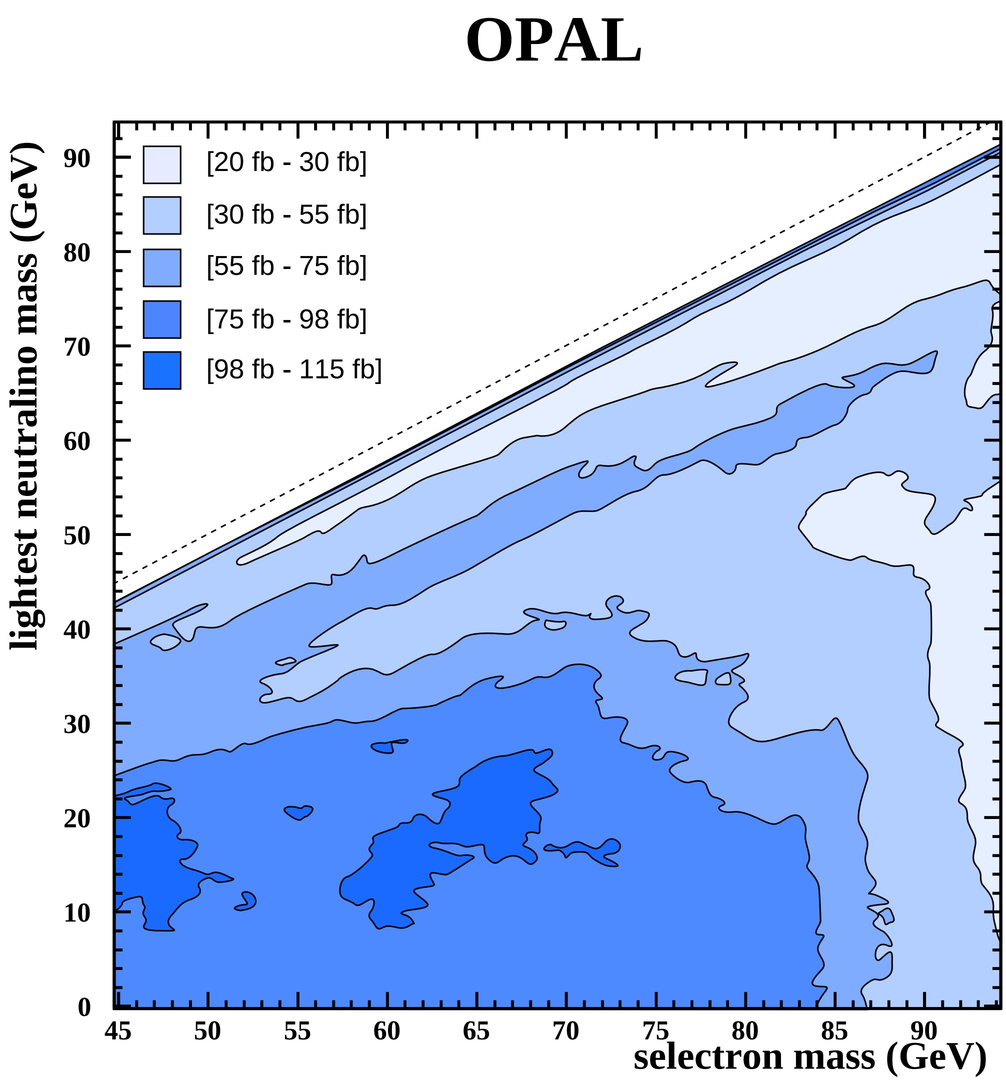

Figure 8.2: *Contours of the 95% CL upper limits on the selectron pair cross-section times* $BR^2(\tilde{e} \rightarrow e\tilde{\chi}_1^0)$ *at* $\sqrt{s}$ *= 189 GeV based on combining the 183 and 189 GeV data-sets assuming a* β^3/s *dependence of the cross-section. The kinematically allowed region is indicated by the dashed line. The unshaded region at very low* Δm *is experimentally inaccessible in this search.*

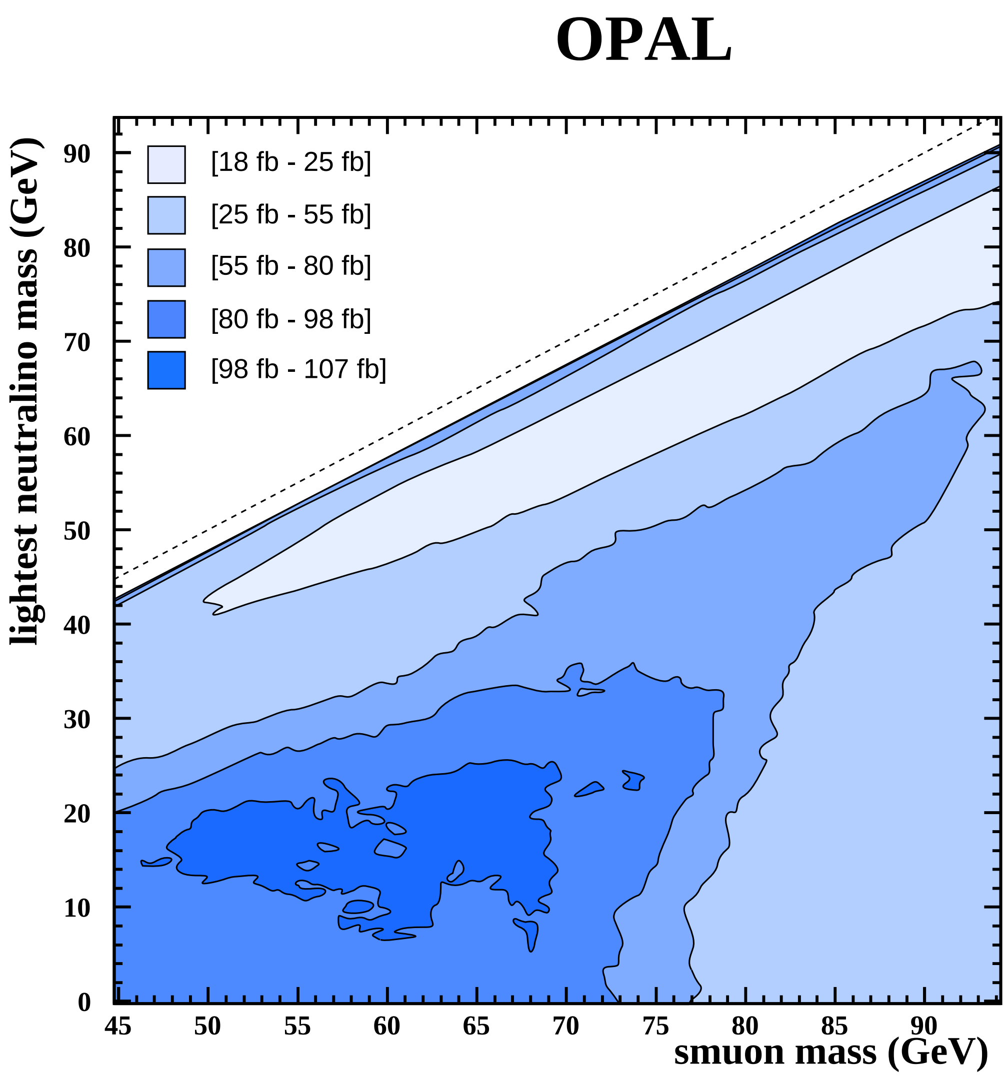

Figure 8.3: *Contours of the 95% CL upper limits on the smuon pair cross-section times* $BR^2(\tilde{\mu} \to \mu\tilde{\chi}_1^0)$ *at* $\sqrt{s}$ *= 189 GeV based on combining the 183 and 189 GeV data-sets assuming a* β^3/s *dependence of the cross-section. The kinematically allowed region is indicated by the dashed line. The unshaded region at very low* Δm *is experimentally inaccessible in this search.*

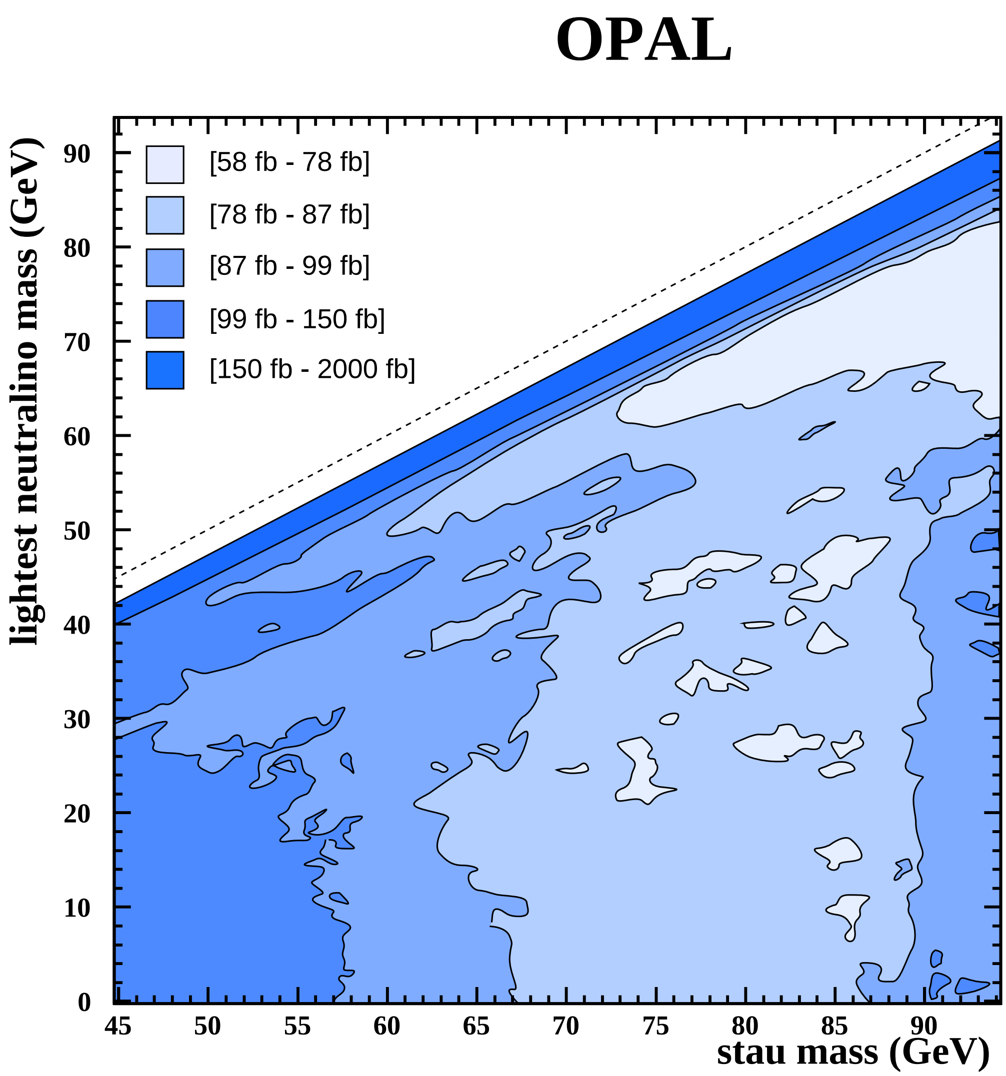

Figure 8.4: *Contours of the 95% CL upper limits on the stau pair cross-section times* $BR^2(\tilde{\tau} \rightarrow \tau\tilde{\chi}_1^0)$ *at* $\sqrt{s}$ = *189 GeV based on combining the 183 and 189 GeV data-sets assuming a* β^3/s *dependence of the cross-section. The kinematically allowed region is indicated by the dashed line. The unshaded region at very low* Δm *is experimentally inaccessible in this search.*

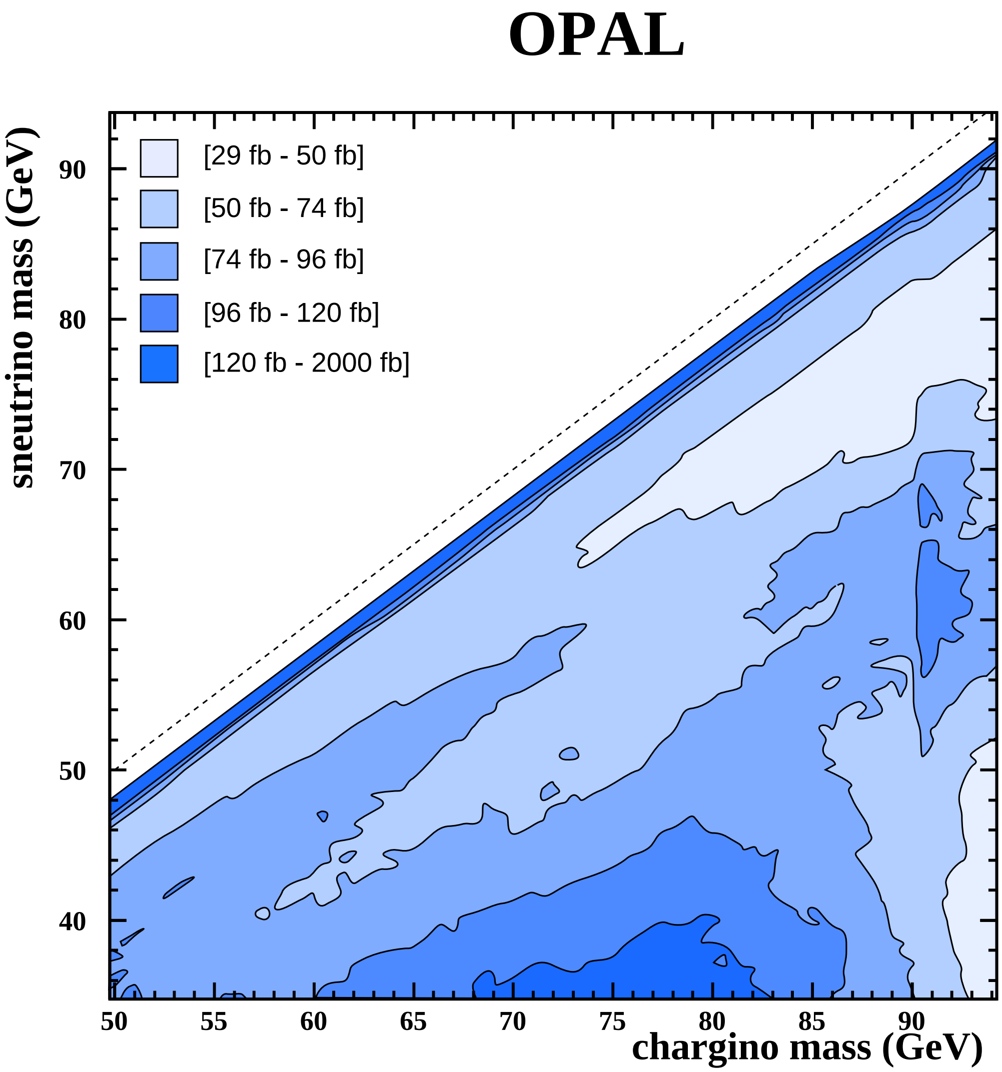

Figure 8.5: *Contours of the 95% CL upper limits on the chargino pair cross-section times* $BR^2(\tilde{\chi}_1^{\pm} \to \ell^{\pm}\tilde{\nu})$ *(2-body decay) at* $\sqrt{s} = 189$ *GeV. The limits have been calculated for the case where either the three sneutrino generations are mass degenerate, or only one flavour is kinematically allowed. The limit is obtained by combining the 183 and 189 GeV data-sets assuming a* β/s *dependence of the cross-section. The kinematically allowed region is indicated by the dashed line. The unshaded region at very low* Δm *is experimentally inaccessible in this search.*

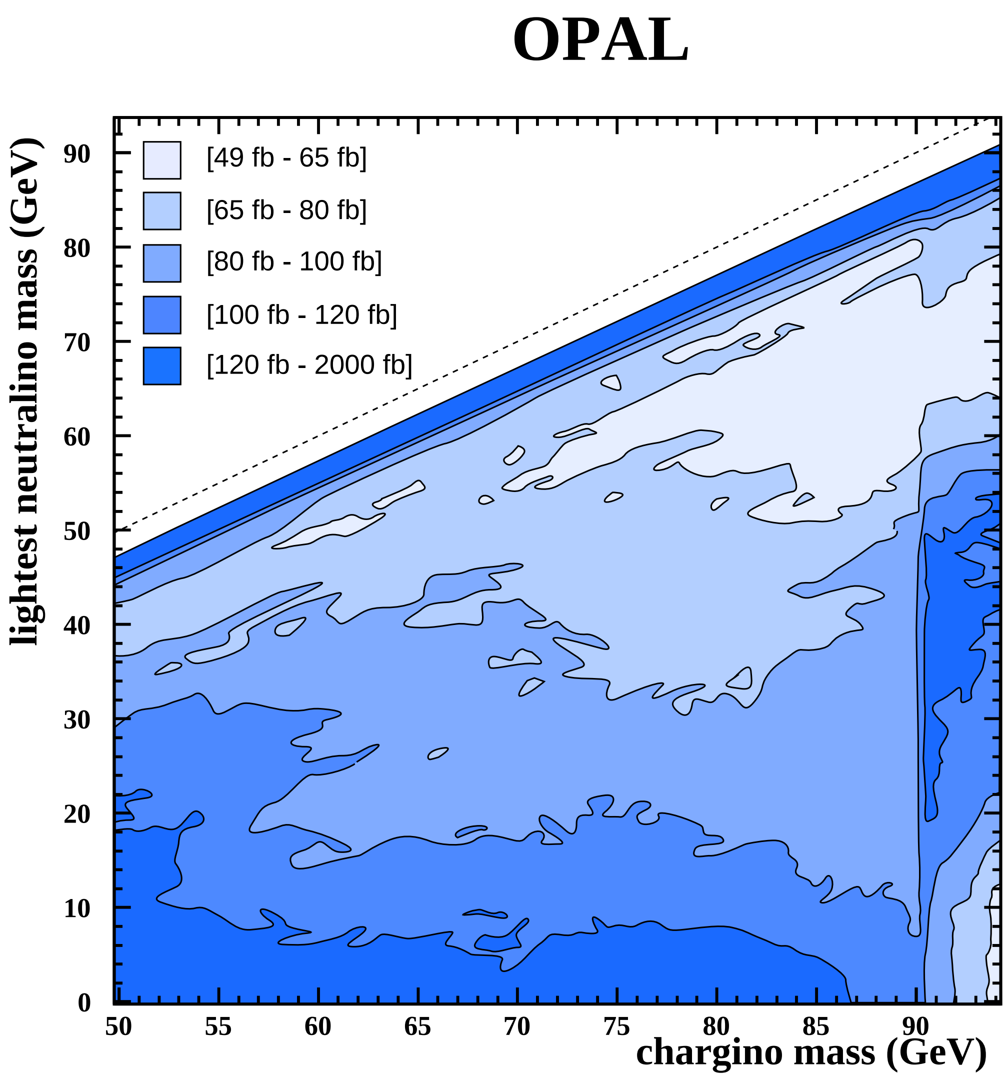

Figure 8.6: *Contours of the 95% CL upper limits on the chargino pair cross-section times* $BR^2(\tilde{\chi}_1^\pm \to \ell^\pm \nu \tilde{\chi}_1^0)$ *(3-body decay) at* $\sqrt{s}$ = *189 GeV. The limit is obtained by combining the 183 and 189 GeV data-sets assuming a* β/s *dependence of the cross-section. The kinematically allowed region is indicated by the dashed line. The unshaded region at very low* Δm *is experimentally inaccessible in this search.*

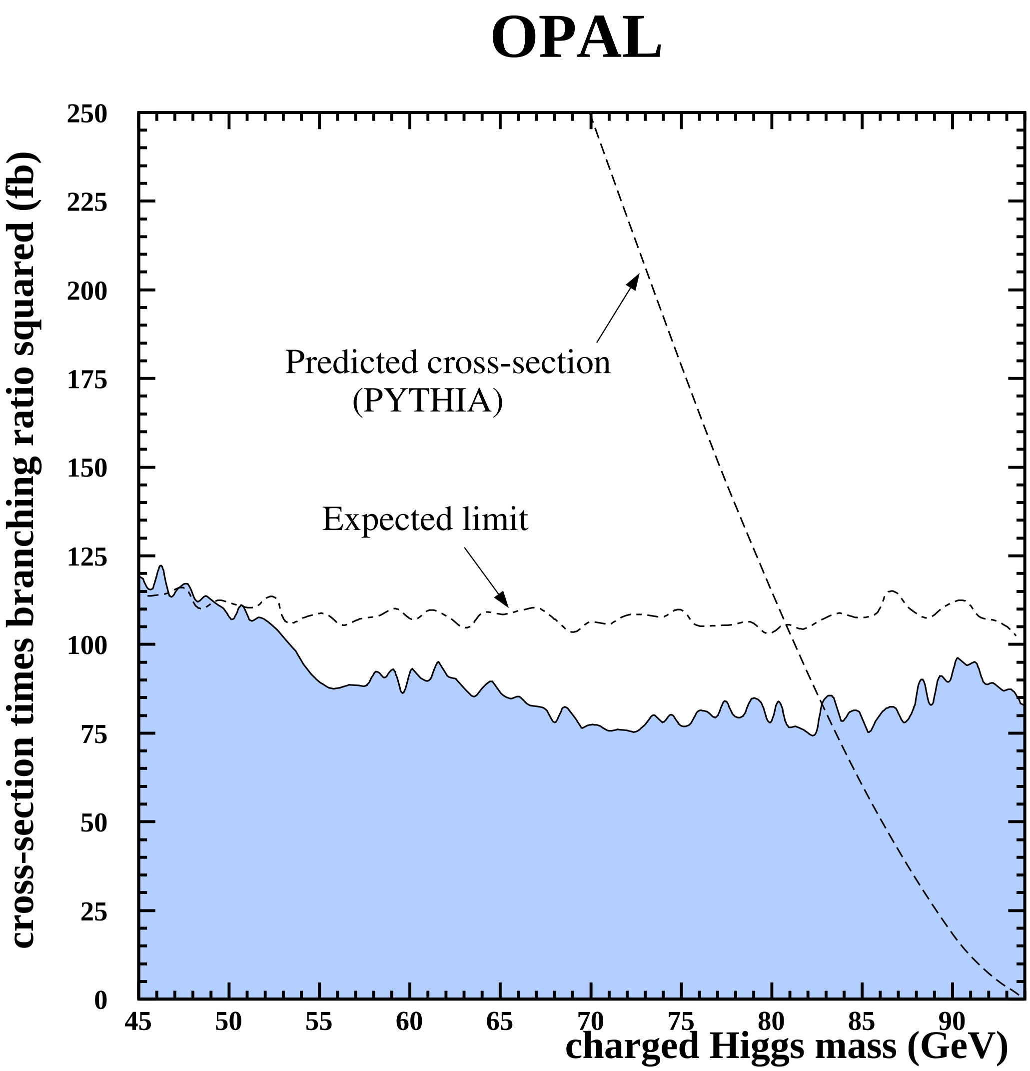

Figure 8.7: *The solid line shows the 95% CL upper limit on the charged Higgs boson pair production cross-section times* $BR^2(\mathrm{H}^\pm \to \tau^\pm\nu_\tau)$ *at* $\sqrt{s}$ = *189 GeV. The limit is obtained by combining the 183 and 189 GeV data-sets assuming the* m_{H^+} *and* $\sqrt{s}$ *dependence of the cross-section predicted by* PYTHIA. *For comparison, the dashed curve shows the prediction from* PYTHIA *at* $\sqrt{s}$ = *189 GeV for a 100% branching ratio for the decay* $\mathrm{H}^\pm \to \tau^\pm\nu_\tau$. *The expected limit calculated from Monte Carlo alone is indicated by the dash-dotted line.*

8.3 Expected Limits and Confidence Levels for Consistency with Expectation

Table 8.1 gives the values of the following quantities for a number of values of m and Δm in the search for selectrons:

1. The signal selection efficiency of the general selection at $\sqrt{s} = 189$ GeV (the efficiencies at $\sqrt{s} = 183$ GeV are similar).

2. The 95% CL upper limit on $\sigma.BR^2$ at $\sqrt{s} = 189$ GeV, obtained by combining the data at $\sqrt{s} = 189$ GeV and $\sqrt{s} = 183$ GeV.

3. The expected 95% CL upper limit on $\sigma.BR^2$ in the absence of signal $\langle\sigma_{95}\rangle$. This is calculated using an ensemble of 1000 toy Monte Carlo experiments to simulate the data, in which the total number of candidates for each experiment is drawn from a Poisson distribution with mean equal to the number of events expected from the Standard Model, and for each candidate, a value of L_R is assigned, chosen randomly according to the expected L_R distribution for Standard Model processes. The expected limit at a given point in m and Δm is the mean value of the limit for the ensemble of simulated experiments.

4. The confidence level for consistency with the Standard Model, calculated as the fraction of the simulated experiments for which the upper limit on $\sigma.BR^2$ is greater than or equal to the value calculated using the actual data. In the absence of signal, a CL of 50% is expected on average [1].

Tables 8.2, 8.3, 8.4, 8.5 and 8.6 show the same information for smuons, staus, charginos with two-body decay, charginos with three-body decay and charged Higgs

[1] Values of 100% correspond to points where there are no candidate events with non-zero L_R in the OPAL data. In this case, all toy Monte Carlo experiments will have a value of σ_{95} equal to or (if there are toy Monte Carlo candidates with non-zero L_R) greater than the value for the actual data.

bosons, respectively.

For some points in m and Δm in Tables 8.1 and 8.2, the confidence level for consistency with the Standard Model is small (around 1%). If the calculation at each (m, Δm) point for each search channel were independent, this would not be surprising. However, a given data event can have a high value of L_R over a considerable range of m and Δm and in several different search channels. There is therefore a significant amount of correlation among the different (m, Δm) points and among the different channels. The probability of getting a low confidence level for one or more points in m and Δm for one or more of the search channels depends on the degree of this correlation. The degree of correlation between adjacent points is strong when the momentum distributions for those points are similar. The momentum distributions vary slowly with both m and Δm when Δm is high (hence the clustering of low confidence level values in Table 8.2), but vary considerably with Δm when Δm is low.

The effect was investigated by calculating the cross-section limits for each of 1000 experiments in which the data are simulated by randomly selected Standard Model Monte Carlo events. For each simulated experiment, the number of events taken from a Monte Carlo sample simulating a given process is drawn from a Poisson distribution with mean equal to the number of events expected for that process. For each experiment, the confidence level at each (m, Δm) point at which signal Monte Carlo has been generated was calculated as already described, and the number of experiments for which a confidence level of 0.6% [2] or less is obtained for at least one point in m and Δm in at least one search channel was determined. This was found to be the case for 390 of the 1000 experiments.

As a cross-check, taking the mean of the ensemble of limits obtained at each (m, Δm) point for these simulated experiments was used as an alternative to the method described above to obtain $\langle \sigma_{95} \rangle$. The results were found to be consistent.

[2] This is the lowest value of the confidence level in Tables 8.1 to 8.6.

It can be concluded from Tables 8.1 to 8.6, together with the above discussion, that the observed data is in good agreement with the Standard Model at all of the (m, Δm) gridpoints at which signal Monte Carlo has been generated[3], for all search channels. Inspection of Figures 8.2 to 8.7 does not reveal any evidence for the existence of regions in between the grid points where the cross-section limit is anomalously high. It can therefore be concluded that there is no evidence for new physics for all values of m and Δm that are kinematically accessible.

[3]The mass grids presented in Tables 8.1 to 8.6 correspond to only part of the full Monte Carlo grids, defined in Section 5.3. Expected limits have been calculated and compared with observed limits for all points in the complete grid.

Δm (GeV)	$m_{\tilde{\mathrm{e}}^-}$ (GeV)					
	45	55	65	75	85	94
signal selection efficiency of the general selection at 189 GeV (%)						
2	13.0±1.1	10.5±1.0	7.8±0.8	4.2±0.6	1.4±0.4	0.4±0.2
2.5	25.1±1.4	21.4±1.3	22.1±1.3	18.5±1.2	12.9±1.1	7.4±0.8
5	56.6±1.6	59.5±1.6	59.0±1.6	60.5±1.5	60.2±1.5	55.9±1.6
10	71.0±1.4	74.4±1.4	76.7±1.3	76.3±1.3	77.5±1.3	76.0±1.4
20	78.8±1.3	81.6±1.2	85.2±1.1	85.2±1.1	84.6±1.1	85.9±1.1
$m/2$	78.5±1.3	84.8±1.1	87.4±1.0	90.6±0.9	90.4±0.9	92.1±0.9
$m-20$	79.0±1.3	85.6±1.1	88.8±1.0	90.4±0.9	91.8±0.9	93.1±0.8
$m-10$	78.9±1.3	84.9±1.1	89.3±1.0	90.3±0.9	91.1±0.9	92.5±0.8
m	77.4±1.3	84.1±1.2	88.7±1.0	90.1±0.9	91.3±0.9	93.2±0.8
95% CL upper limit on the cross-section times $BR^2(\tilde{\mathrm{e}} \to \mathrm{e}\tilde{\chi}_1^0)$ (fb)						
2	93.8	117.2	164.8	305.5	973.8	4138.6
2.5	49.2	56.5	56.1	67.7	106.1	223.7
5	36.7	25.7	24.3	21.9	23.3	29.6
10	63.1	50.2	43.8	30.8	26.8	22.0
20	64.8	50.9	44.7	48.9	54.7	25.6
$m/2$	92.3	73.2	79.4	54.5	35.3	20.0
m-20	97.8	101.5	93.3	87.8	63.4	23.5
m-10	91.5	76.9	73.8	89.9	70.4	29.6
m	81.4	84.6	85.8	86.8	64.0	34.5
expected upper limit on the cross-section times $BR^2(\tilde{\mathrm{e}} \to \mathrm{e}\tilde{\chi}_1^0)$ (fb)						
2	148.3	175.1	237.0	414.5	1325.7	4616.9
2.5	82.0	90.9	87.4	104.9	136.6	264.2
5	42.2	39.3	38.9	34.6	33.8	34.1
10	40.4	33.3	28.5	25.8	24.5	24.8
20	69.1	52.8	43.2	34.8	27.9	23.6
$m/2$	76.1	71.5	62.5	62.0	57.2	33.6
m-20	80.7	78.7	79.3	80.0	70.3	38.9
m-10	84.9	78.6	79.6	81.1	69.3	37.9
m	81.9	76.0	76.0	80.8	71.1	38.8
CL for consistency with SM (%)						
2	100.0	100.0	100.0	100.0	100.0	100.0
2.5	100.0	100.0	100.0	100.0	100.0	100.0
5	57.0	88.6	90.5	95.4	89.1	100.0
10	5.2	6.8	6.3	18.0	33.1	83.9
20	47.6	44.6	38.2	10.4	0.6	19.7
$m/2$	20.7	37.7	17.9	53.6	88.8	99.9
m-20	20.3	14.4	22.8	27.8	52.0	95.0
m-10	30.5	43.2	45.6	27.4	37.2	72.3
m	38.2	28.1	24.9	30.9	51.2	56.0

Table 8.1: Signal selection efficiency of the general selection at 189 GeV, 95% CL upper limit on the cross-section times $BR^2(\tilde{\mathrm{e}} \to \mathrm{e}\tilde{\chi}_1^0)$, expected upper limit on the cross-section times $BR^2(\tilde{\mathrm{e}} \to \mathrm{e}\tilde{\chi}_1^0)$, and the confidence level for consistency with the Standard Model in the search for $\tilde{\mathrm{e}}^+\tilde{\mathrm{e}}^-$ production for different values of $m_{\tilde{\mathrm{e}}^-}$ and Δm.

Δm (GeV)	$m_{\tilde{\mu}^-}$ (GeV) 45	55	65	75	85	94
signal selection efficiency of the general selection at 189 GeV (%)						
2	14.9±1.1	14.1±1.1	9.8±0.9	6.5±0.8	0.7±0.3	0.0±0.0
2.5	26.7±1.4	27.7±1.4	25.0±1.4	21.3±1.3	14.3±1.1	8.0±0.9
5	58.7±1.6	60.5±1.5	60.4±1.5	60.0±1.5	60.3±1.5	57.4±1.6
10	75.8±1.4	76.7±1.3	76.2±1.3	76.4±1.3	76.5±1.3	74.1±1.4
20	85.4±1.1	86.0±1.1	84.8±1.1	84.2±1.2	84.0±1.2	83.2±1.2
$m/2$	86.3±1.1	87.8±1.0	87.2±1.1	90.4±0.9	90.4±0.9	91.7±0.9
$m-20$	86.7±1.1	89.2±1.0	89.7±1.0	91.2±0.9	92.9±0.8	92.8±0.8
$m-10$	88.5±1.0	90.6±0.9	89.6±1.0	91.3±0.9	92.4±0.8	93.0±0.8
m	88.6±1.0	90.6±0.9	89.8±1.0	91.1±0.9	92.1±0.9	92.5±0.8
95% CL upper limit on the cross-section times $BR^2(\tilde{\mu} \to \mu\tilde{\chi}_1^0)$ (fb)						
2	105.6	119.3	177.3	300.8	2069.3	–
2.5	63.3	61.5	72.0	88.8	98.8	206.9
5	30.3	31.0	39.5	31.8	34.1	28.8
10	35.0	22.7	18.5	17.3	18.2	22.3
20	53.5	38.7	39.9	41.3	37.6	25.5
$m/2$	64.7	76.7	81.6	71.1	51.7	44.1
m-20	80.1	100.5	104.6	89.6	45.3	34.3
m-10	85.4	94.6	92.8	62.9	43.4	34.3
m	83.5	87.7	88.8	58.9	43.5	34.7
expected upper limit on the cross-section times $BR^2(\tilde{\mu} \to \mu\tilde{\chi}_1^0)$ (fb)						
2	112.8	116.1	169.0	286.8	2977.5	–
2.5	67.6	64.7	68.9	82.4	119.5	226.1
5	34.8	33.8	31.2	28.2	28.8	30.2
10	30.8	27.4	25.3	22.6	22.6	24.3
20	47.5	39.3	35.9	31.3	25.3	22.1
$m/2$	50.9	50.9	50.4	51.0	50.1	33.4
m-20	51.8	52.8	55.8	58.7	56.8	36.4
m-10	53.1	51.1	53.7	56.5	56.5	38.1
m	50.6	49.7	52.9	57.6	56.7	39.5
CL for consistency with SM (%)						
2	64.6	47.9	45.7	43.7	100.0	–
2.5	65.7	60.6	54.1	40.2	100.0	100.0
5	57.8	47.5	19.0	35.9	27.2	100.0
10	26.1	63.8	76.1	100.0	100.0	100.0
20	27.8	42.1	30.0	15.0	7.5	8.5
$m/2$	17.6	7.6	4.8	10.6	36.0	14.2
m-20	6.3	1.7	1.1	6.1	66.8	49.0
m-10	4.4	1.3	2.7	29.1	69.0	52.3
m	3.4	2.8	3.9	36.3	71.3	57.1

Table 8.2: Signal selection efficiency of the general selection at 189 GeV, 95% CL upper limit on the cross-section times $BR^2(\tilde{\mu} \to \mu\tilde{\chi}_1^0)$, expected upper limit on the cross-section times $BR^2(\tilde{\mu} \to \mu\tilde{\chi}_1^0)$, and the confidence level for consistency with the Standard Model in the search for $\tilde{\mu}^+\tilde{\mu}^-$ production for different values of $m_{\tilde{\mu}^-}$ and Δm.

Δm (GeV)	$m_{\tilde{\tau}^-}$ (GeV) 45	55	65	75	85	94
signal selection efficiency of the general selection at 189 GeV (%)						
2	0.2±0.0	0.1±0.0	0.1±0.0	0.0±0.0	0.0±0.0	0.0±0.0
2.5	0.7±0.1	0.5±0.1	0.3±0.0	0.3±0.0	0.1±0.0	0.0±0.0
5	15.6±0.3	14.0±0.3	13.1±0.3	11.6±0.3	10.3±0.3	9.1±0.3
10	38.3±0.4	39.1±0.4	39.5±0.4	38.8±0.4	39.4±0.4	38.8±0.4
20	57.4±0.4	59.4±0.4	59.9±0.4	60.9±0.4	60.9±0.4	62.2±0.4
$m/2$	59.3±0.4	64.8±0.4	69.6±0.4	71.8±0.4	73.7±0.4	74.5±0.4
$m-20$	60.6±0.4	69.1±0.4	73.4±0.4	74.4±0.4	77.5±0.4	78.3±0.4
$m-10$	65.2±0.4	71.1±0.4	73.9±0.4	76.2±0.4	77.7±0.4	79.2±0.4
m	66.2±0.4	71.3±0.4	74.5±0.4	76.1±0.4	77.7±0.4	79.0±0.4
95% CL upper limit on the cross-section times $BR^2(\tilde{\tau} \to \tau\tilde{\chi}_1^0)$ (fb)						
2	12180.7	32560.6	16554.6	–	–	–
2.5	2678.7	4145.1	5526.8	6808.6	19454.0	–
5	137.6	168.4	181.7	243.9	274.5	324.1
10	106.8	92.1	81.5	75.7	74.2	86.7
20	101.1	92.8	84.7	86.5	77.1	59.2
$m/2$	100.8	97.5	87.4	76.3	76.2	90.6
m-20	106.4	93.5	78.7	75.8	76.0	87.6
m-10	119.8	97.1	83.2	75.5	73.7	97.6
m	115.4	94.1	86.1	76.6	81.3	87.6
expected upper limit on the cross-section times $BR^2(\tilde{\tau} \to \tau\tilde{\chi}_1^0)$ (fb)						
2	11163.9	20013.4	19897.3	–	–	–
2.5	2916.5	4380.8	6850.2	7709.0	17774.8	–
5	189.5	209.3	221.8	237.2	262.6	284.6
10	107.0	103.4	97.4	98.2	94.2	92.1
20	103.4	95.8	89.7	82.9	79.1	74.3
$m/2$	106.9	104.7	99.5	95.1	93.8	96.1
m-20	108.3	107.1	108.3	107.5	108.1	112.2
m-10	113.9	112.1	114.4	109.7	114.4	111.6
m	118.2	114.1	112.4	110.6	113.7	114.0
CL for consistency with SM (%)						
2	37.4	7.4	100.0	–	–	–
2.5	56.8	41.2	77.2	65.5	45.3	–
5	75.5	66.6	62.8	38.6	32.8	23.0
10	40.7	56.8	61.3	70.0	66.6	50.3
20	43.5	44.0	46.9	37.7	42.5	67.2
$m/2$	46.1	47.5	54.7	64.4	64.1	47.5
m-20	41.4	54.3	74.1	76.0	75.0	67.0
m-10	33.0	56.0	72.9	79.0	83.2	54.0
m	40.6	59.7	67.4	79.0	73.3	69.6

Table 8.3: Signal selection efficiency of the general selection at 189 GeV, 95% CL upper limit on the cross-section times $BR^2(\tilde{\tau} \to \tau\tilde{\chi}_1^0)$, expected upper limit on the cross-section times $BR^2(\tilde{\tau} \to \tau\tilde{\chi}_1^0)$, and the confidence level for consistency with the Standard Model in the search for $\tilde{\tau}^+\tilde{\tau}^-$ production for different values of $m_{\tilde{\tau}^-}$ and Δm.

Δm (GeV)	$m_{\tilde{\chi}_1^\pm}$ (GeV) 50	60	70	80	90	94
signal selection efficiency of the general selection at 189 GeV (%)						
2	7.9±0.4	6.6±0.4	4.9±0.3	2.3±0.2	0.5±0.1	0.1±0.0
3	21.6±0.7	21.6±0.7	20.6±0.6	19.5±0.6	15.8±0.6	13.3±0.5
4	34.3±0.8	33.5±0.7	33.7±0.7	33.6±0.7	31.5±0.7	32.5±0.7
5	41.3±0.8	43.4±0.8	42.5±0.8	41.9±0.8	43.0±0.8	44.7±0.8
10	61.0±0.8	64.4±0.8	63.6±0.8	63.9±0.8	63.5±0.8	65.4±0.8
20	–	75.8±0.7	77.4±0.7	78.2±0.7	79.5±0.6	78.3±0.7
$(m-15)/2$	–	77.1±0.7	82.2±0.6	82.7±0.6	85.8±0.6	86.6±0.5
$m-35$	69.7±0.7	78.3±0.7	83.2±0.6	85.9±0.6	87.4±0.5	89.0±0.5
95% CL upper limit on the cross-section times $BR^2(\tilde{\chi}_1^\pm \to \ell^\pm \tilde{\nu})$ (fb)						
2	241.3	262.3	330.0	755.6	3368.0	20947.5
3	103.8	89.2	98.6	103.8	88.6	125.3
4	62.3	60.7	68.3	61.5	80.1	54.7
5	53.0	44.9	58.5	50.3	63.6	62.5
10	92.2	82.4	57.7	39.0	39.4	38.2
20	–	72.1	64.8	60.8	65.3	40.8
$(m-15)/2$	–	81.9	83.9	88.2	61.5	53.7
m-35	84.6	87.0	116.9	118.5	70.1	42.6
expected upper limit on the cross-section times $BR^2(\tilde{\chi}_1^\pm \to \ell^\pm \tilde{\nu})$ (fb)						
2	289.4	313.9	387.6	900.9	4055.8	22119.2
3	123.1	117.9	108.4	119.4	134.2	165.3
4	86.7	82.2	75.4	70.9	77.4	73.1
5	77.5	68.4	68.7	64.7	59.0	60.1
10	79.5	64.0	58.2	52.1	47.8	44.3
20	–	108.5	84.7	68.2	49.7	38.7
$(m-15)/2$	–	121.0	119.0	115.5	108.3	74.7
m-35	103.8	130.8	154.0	166.4	143.7	88.8
CL for consistency with SM (%)						
2	63.3	59.1	68.3	70.7	76.5	66.1
3	61.4	72.3	48.1	56.9	100.0	73.5
4	80.1	77.6	51.8	53.4	36.9	70.2
5	82.9	88.6	59.0	72.0	33.5	29.5
10	24.8	14.7	42.1	76.4	64.2	59.2
20	–	80.9	70.0	53.1	15.2	33.6
$(m-15)/2$	–	79.5	76.0	69.4	93.4	79.0
m-35	63.9	81.4	63.6	72.7	97.0	98.9

Table 8.4: Signal selection efficiency of the general selection at 189 GeV, 95% CL upper limit on the cross-section times $BR^2(\tilde{\chi}_1^\pm \to \ell^\pm \tilde{\nu})$, expected upper limit on the cross-section times $BR^2(\tilde{\chi}_1^\pm \to \ell^\pm \tilde{\nu})$, and the confidence level for consistency with the Standard Model in the search for $\tilde{\chi}_1^+\tilde{\chi}_1^-$(2-body decays) production for different values of $m_{\tilde{\chi}_1^\pm}$ and Δm. The bins without entries correspond to values of $m_{\tilde{\nu}} < 35$, which are excluded and therefore not considered in the analysis.

Δm (GeV)	$m_{\tilde{\chi}_1^\pm}$ (GeV) 50	60	70	80	90	94
signal selection efficiency of the general selection at 189 GeV (%)						
3	3.7±0.3	3.2±0.3	2.5±0.2	1.0±0.2	0.2±0.1	0.2±0.1
5	17.1±0.6	16.3±0.6	15.2±0.6	13.3±0.5	11.4±0.5	10.8±0.5
10	39.9±0.8	40.8±0.8	40.9±0.8	41.6±0.8	40.8±0.8	41.6±0.8
20	59.1±0.8	60.4±0.8	62.2±0.8	60.8±0.8	62.8±0.8	63.8±0.8
$m/2$	63.3±0.8	68.7±0.7	74.3±0.7	77.9±0.7	79.3±0.6	80.3±0.6
$m-20$	67.3±0.7	72.6±0.7	78.0±0.7	81.2±0.6	83.9±0.6	84.0±0.6
$m-10$	70.1±0.7	75.9±0.7	79.4±0.6	83.0±0.6	87.0±0.5	88.1±0.5
m	73.2±0.7	77.4±0.7	81.2±0.6	85.2±0.6	88.1±0.5	89.5±0.5
95% CL upper limit on the cross-section times $BR^2(\tilde{\chi}_1^\pm \to \ell^\pm\nu\tilde{\chi}_1^0)$ (fb)						
3	355.9	540.9	598.9	1578.0	5613.2	11457.9
5	111.0	116.1	134.6	114.5	156.9	272.9
10	74.7	60.4	66.5	61.0	56.2	65.5
20	91.3	78.4	68.0	64.3	51.0	52.8
$m/2$	105.8	99.7	82.9	69.9	88.0	121.6
m-20	118.5	85.2	91.4	91.8	89.2	89.4
m-10	111.6	103.7	104.2	101.6	88.1	60.6
m	133.7	132.4	117.3	117.2	99.6	57.6
expected upper limit on the cross-section times $BR^2(\tilde{\chi}_1^\pm \to \ell^\pm\nu\tilde{\chi}_1^0)$ (fb)						
3	563.5	668.8	791.2	2050.1	8303.3	10493.8
5	163.4	154.9	165.4	169.6	203.6	222.4
10	90.4	82.6	80.5	76.1	76.4	74.4
20	92.0	81.2	70.0	67.3	63.0	61.7
$m/2$	100.3	94.4	89.9	81.2	78.5	82.5
m-20	103.7	114.8	114.9	113.9	131.0	140.5
m-10	128.2	130.9	135.3	136.9	166.9	136.5
m	139.1	144.8	154.9	183.3	179.4	133.9
CL for consistency with SM (%)						
3	94.9	62.7	83.3	76.7	100.0	37.5
5	82.9	72.6	62.5	88.5	79.9	30.5
10	62.1	76.4	62.6	68.0	74.8	53.0
20	41.3	44.3	43.7	46.3	65.2	60.2
$m/2$	35.7	35.7	49.8	54.9	28.6	8.4
m-20	26.7	69.0	65.0	62.3	80.5	84.9
m-10	52.9	63.4	66.8	69.9	94.2	99.0
m	40.9	43.9	64.9	78.6	89.8	99.0

Table 8.5: Signal selection efficiency of the general selection at 189 GeV, 95% CL upper limit on the cross-section times $BR^2(\tilde{\chi}_1^\pm \to \ell^\pm\nu\tilde{\chi}_1^0)$, expected upper limit on the cross-section times $BR^2(\tilde{\chi}_1^\pm \to \ell^\pm\nu\tilde{\chi}_1^0)$, and the confidence level for consistency with the Standard Model in the search for $\tilde{\chi}_1^+\tilde{\chi}_1^-$(3-body decays) production for different values of $m_{\tilde{\chi}_1^\pm}$ and Δm.

m_{H^+} (GeV)					
45	55	65	75	85	94
signal selection efficiency of the general selection at 189 GeV (%)					
66.6±0.7	72.3±0.7	74.6±0.7	76.9±0.7	77.6±0.7	79.7±0.6
95% CL upper limit on the cross-section times $BR^2(H^\pm \to \tau^\pm\nu_\tau)$ (fb)					
113.6	84.8	81.5	73.2	77.0	80.1
expected upper limit on the cross-section times $BR^2(H^\pm \to \tau^\pm\nu_\tau)$ (fb)					
117.7	113.2	114.0	114.0	112.3	111.4
CL for consistency with SM (%)					
40.8	70.3	75.0	83.5	78.7	76.8

Table 8.6: Signal selection efficiency of the general selection at 189 GeV, 95% CL upper limit on the cross-section times $BR^2(H^\pm \to \tau^\pm\nu_\tau)$, expected upper limit on the cross-section times $BR^2(H^\pm \to \tau^\pm\nu_\tau)$, and the confidence level for consistency with the Standard Model in the search for H^+H^- production for different values of m_{H^+}.

8.4 Limits on the Masses of Charged Scalar Leptons

The data can be used to set limits on the masses of right-handed sleptons[4] based on the expected right-handed slepton pair cross-sections and branching ratios. Smuons and staus are produced in the s-channel only, and the cross-section depends only on the slepton mass. The branching ratio is model dependent, however, and the excluded masses are presented for several values of the branching ratio squared to $\ell^{\pm}\tilde{\chi}_1^0$. Selectrons are produced in both the s- and t-channels, and the cross-section and branching ratio are therefore both model dependent. Excluded masses for selectrons are presented for some specific values of μ and $\tan\beta$. The cross-sections have been calculated [46] using SUSYGEN at each centre-of-mass energy and take into account initial state radiation.

Figure 8.8 shows limits on right-handed smuons as a function of smuon mass and lightest neutralino mass for several assumed values of the branching ratio squared for $\tilde{\mu}_R^{\pm} \to \mu^{\pm}\tilde{\chi}_1^0$. The expected limit, calculated using Monte Carlo only, for a branching ratio of 100% is also shown. For a branching ratio $\tilde{\mu}_R^{\pm} \to \mu^{\pm}\tilde{\chi}_1^0$ of 100% and for a smuon-neutralino mass difference exceeding 3 GeV, right-handed smuons are excluded at 95% CL for masses below 82.3 GeV.

The 95% CL upper limit on the production of right-handed $\tilde{\tau}^+\tilde{\tau}^-$ times the branching ratio squared for $\tilde{\tau}_R^{\pm} \to \tau^{\pm}\tilde{\chi}_1^0$ is shown in Figure 8.9. The expected limit for a branching ratio of 100% is also shown. For a branching ratio $\tilde{\tau}_R^{\pm} \to \tau^{\pm}\tilde{\chi}_1^0$ of 100% and for a stau-neutralino mass difference exceeding 8 GeV, right-handed staus are excluded at 95% CL for masses below 81.0 GeV. These limits are calculated under the assumption that there is no mixing between $\tilde{\tau}_L$ and $\tilde{\tau}_R$. However, the

[4]The right-handed slepton is expected to be lighter than the left-handed slepton. The right-handed slepton tends (not generally valid for selectrons) to have a lower pair production cross-section, and so conventionally limits are given for this (usually) conservative case.

cross-section ratio $\sigma_{\tilde{\tau}_1^+\tilde{\tau}_1^-}/\sigma_{\tilde{\tau}_R^+\tilde{\tau}_R^-}$ at $\sqrt{s} = 189$ GeV varies between 0.89 and 1.20 [46], depending only on the mixing angle. Using this information, the limits shown in Figure 8.9 can be applied to any degree of stau mixing by multiplying the predicted cross-section for $\tilde{\tau}_R^+\tilde{\tau}_R^-$ by the value of $\sigma_{\tilde{\tau}_1^+\tilde{\tau}_1^-}/\sigma_{\tilde{\tau}_R^+\tilde{\tau}_R^-}$ corresponding to the mixing angle considered. The hatched region in Figure 8.9 shows the range of possible positions of the line defining the excluded region for a branching ratio $\tilde{\tau}_1^{\pm} \to \tau^{\pm}\tilde{\chi}_1^0$ of 100% for any degree of stau mixing.

For the case of a massless neutralino (or gravitino) and 100% branching ratio, right-handed smuons and staus are excluded at 95% CL for masses below 85.4 GeV and 81.1 GeV, respectively, and $\tilde{\tau}_1^{\pm}$ is excluded at 95% CL for masses below 80.0 GeV, for any degree of stau mixing.

An alternative approach is to set limits taking into account the predicted cross-section and branching ratio for specific choices of the parameters within the MSSM[5]. For $\mu < -100$ GeV and for two values of $\tan\beta$ (1.5 and 35), Figures 8.10, 8.11 and 8.12 show 95% CL exclusion regions in the $(m_{\tilde{\ell}_R^{\pm}}, m_{\tilde{\chi}_1^0})$ plane for right-handed selectrons, smuons and staus, respectively. For $\mu < -100$ GeV and $\tan\beta = 1.5$, right-handed sleptons are excluded at 95% CL as follows: selectrons with masses below 87.1 GeV for $m_{\tilde{\mathrm{e}}^-} - m_{\tilde{\chi}_1^0} > 5$ GeV; smuons with masses below 81.7 GeV for $m_{\tilde{\mu}^-} - m_{\tilde{\chi}_1^0} > 3$ GeV; and staus with masses below 75.9 GeV for $m_{\tilde{\tau}^-} - m_{\tilde{\chi}_1^0} > 7$ GeV.

[5]In particular regions of the MSSM parameter space, the branching ratio for $\tilde{\ell}^{\pm} \to \ell^{\pm}\tilde{\chi}_1^0$ can be essentially zero and so it is not possible to provide general limits on sleptons within the MSSM on the basis of this search alone. The predicted cross-sections and branching ratios within the MSSM are obtained using SUSYGEN and are calculated with the gauge unification relation, $M_1 = \frac{5}{3}\tan^2\theta_W M_2$ [56].

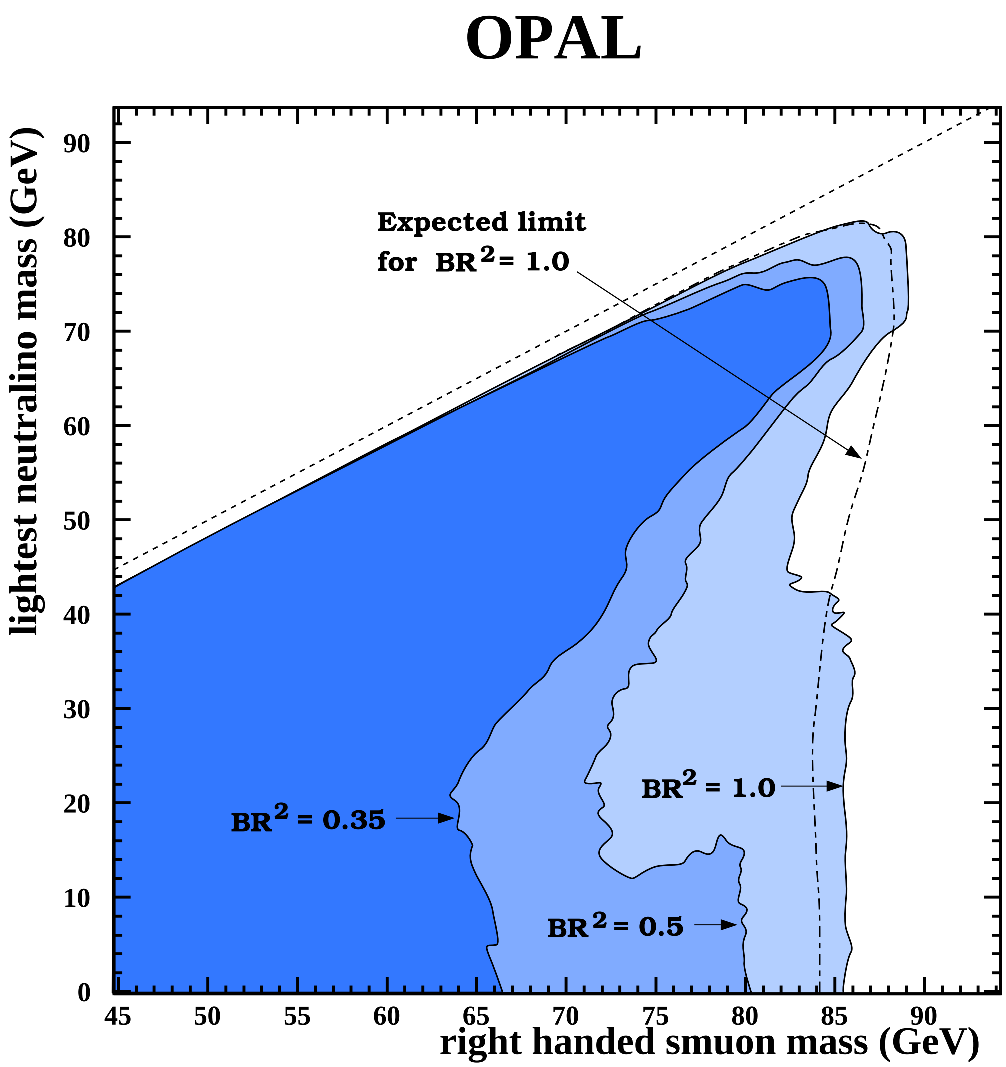

Figure 8.8: *95% CL exclusion region for right-handed smuon pair production obtained by combining the* $\sqrt{s} = 183$ *and 189 GeV data-sets. The limits are calculated for several values of the branching ratio squared for* $\tilde{\mu}^{\pm}_{R} \to \mu^{\pm}\tilde{\chi}^{0}_{1}$ *that are indicated in the figure. Otherwise they have no supersymmetry model assumptions. The kinematically allowed region is indicated by the dashed line. The expected limit for* $BR^2 = 1.0$*, calculated from Monte Carlo alone, is indicated by the dash-dotted line.*

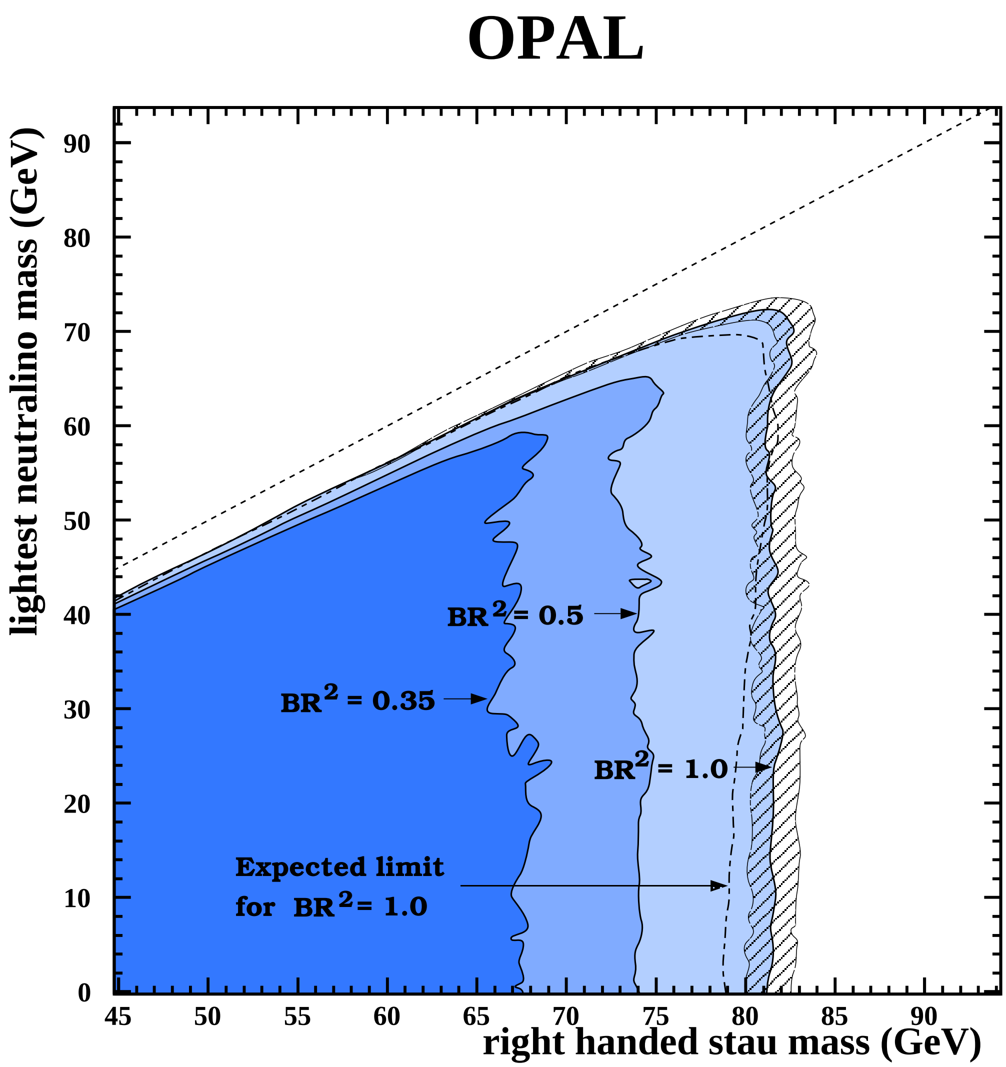

Figure 8.9: *95% CL exclusion region for right-handed stau pair production obtained by combining the* $\sqrt{s} = 183$ *and 189 GeV data-sets. The limits are calculated for several values of the branching ratio squared for* $\tilde{\tau}_R^\pm \to \tau^\pm \tilde{\chi}_1^0$*. The selection efficiency for* $\tilde{\tau}^+\tilde{\tau}^-$ *is calculated for the case that the decay* $\tilde{\tau}^- \to \tau^- \tilde{\chi}_1^0$ *produces unpolarized* $\tau^\pm$*. Otherwise the limits have no supersymmetry model assumptions. The hatched area shows the region in which the limit for* $BR^2 = 1.0$ *can vary if stau mixing occurs (see text). The kinematically allowed region is indicated by the dashed line. The expected limit for* $BR^2 = 1.0$*, calculated from Monte Carlo alone, is indicated by the dash-dotted line.*

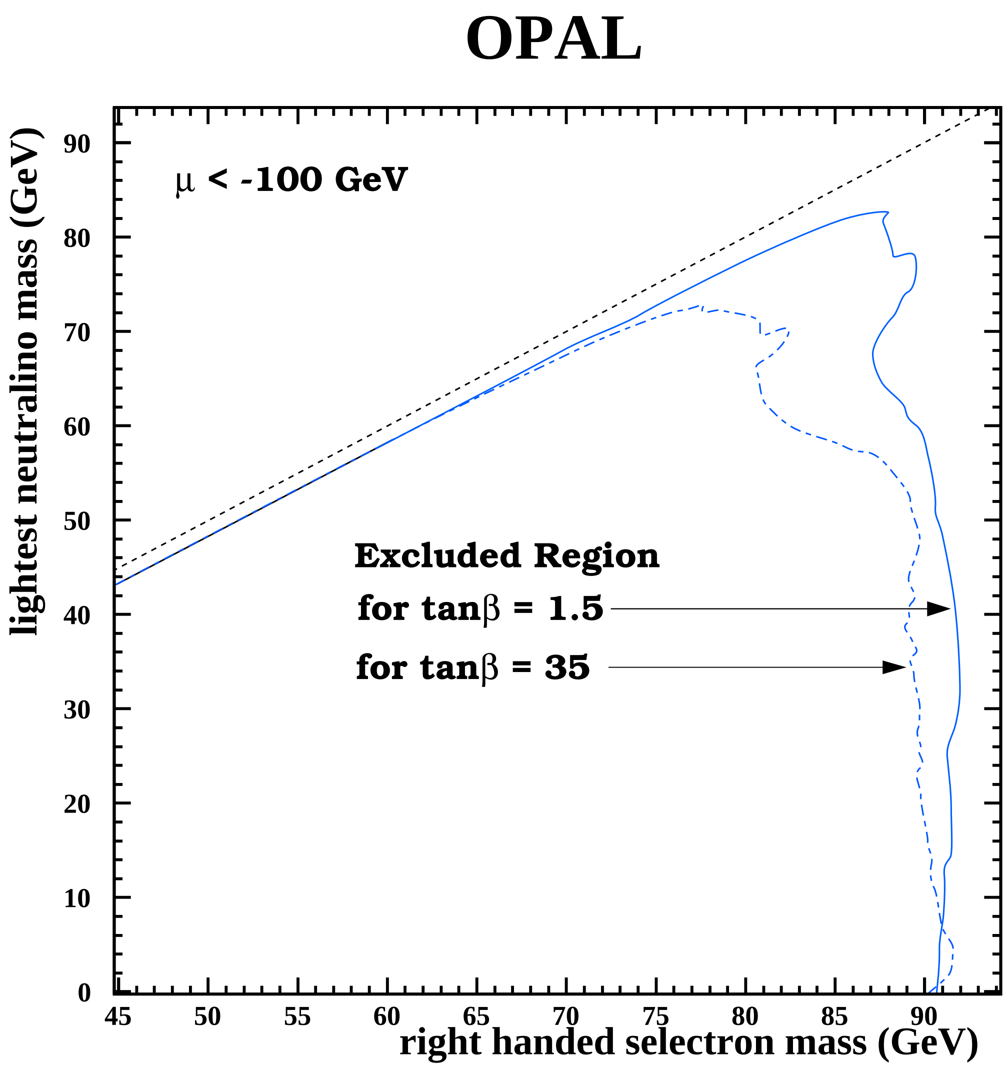

Figure 8.10: *For two values of* $\tan\beta$ *and* $\mu < -100$ *GeV, 95% CL exclusion regions for right-handed selectron pairs within the MSSM, obtained by combining the* $\sqrt{s} = 183$ *and 189 GeV data-sets. The excluded regions are calculated taking into account the predicted branching ratio for* $\tilde{e}^{\pm}_{R} \rightarrow e^{\pm}\tilde{\chi}^{0}_{1}$*. The gauge unification relation,* $M_1 = \frac{5}{3}\tan^2\theta_W M_2$*, is assumed in calculating the MSSM cross-sections and branching ratios. The kinematically allowed region is indicated by the dashed line.*

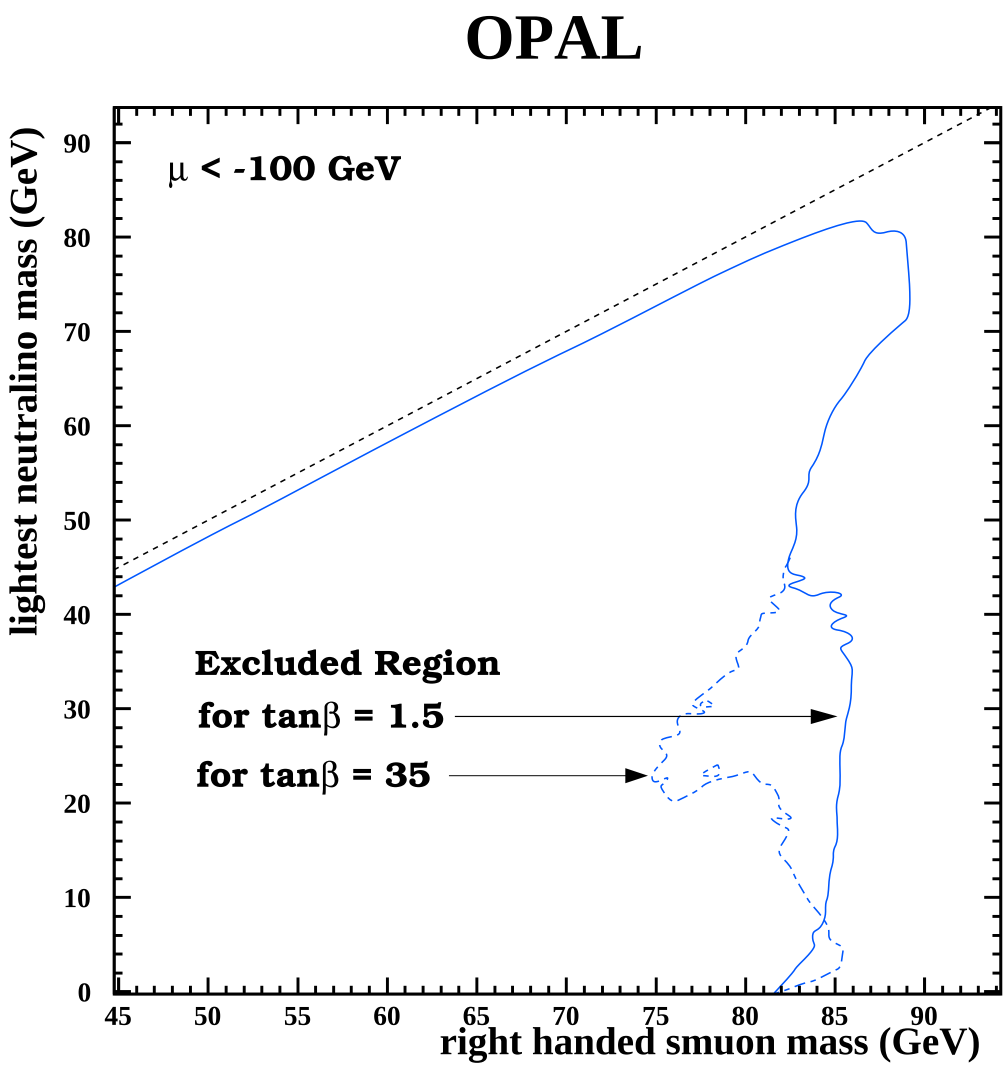

Figure 8.11: *For two values of* $\tan\beta$ *and* $\mu < -100$ *GeV, 95% CL exclusion regions for right-handed smuon pairs within the MSSM, obtained by combining the* $\sqrt{s} = 183$ *and 189 GeV data-sets. The excluded regions are calculated taking into account the predicted branching ratio for* $\tilde{\mu}^{\pm}_{R} \to \mu^{\pm}\tilde{\chi}^{0}_{1}$*. The gauge unification relation,* $M_1 = \frac{5}{3}\tan^2\theta_W M_2$*, is assumed in calculating the MSSM branching ratios. The kinematically allowed region is indicated by the dashed line.*

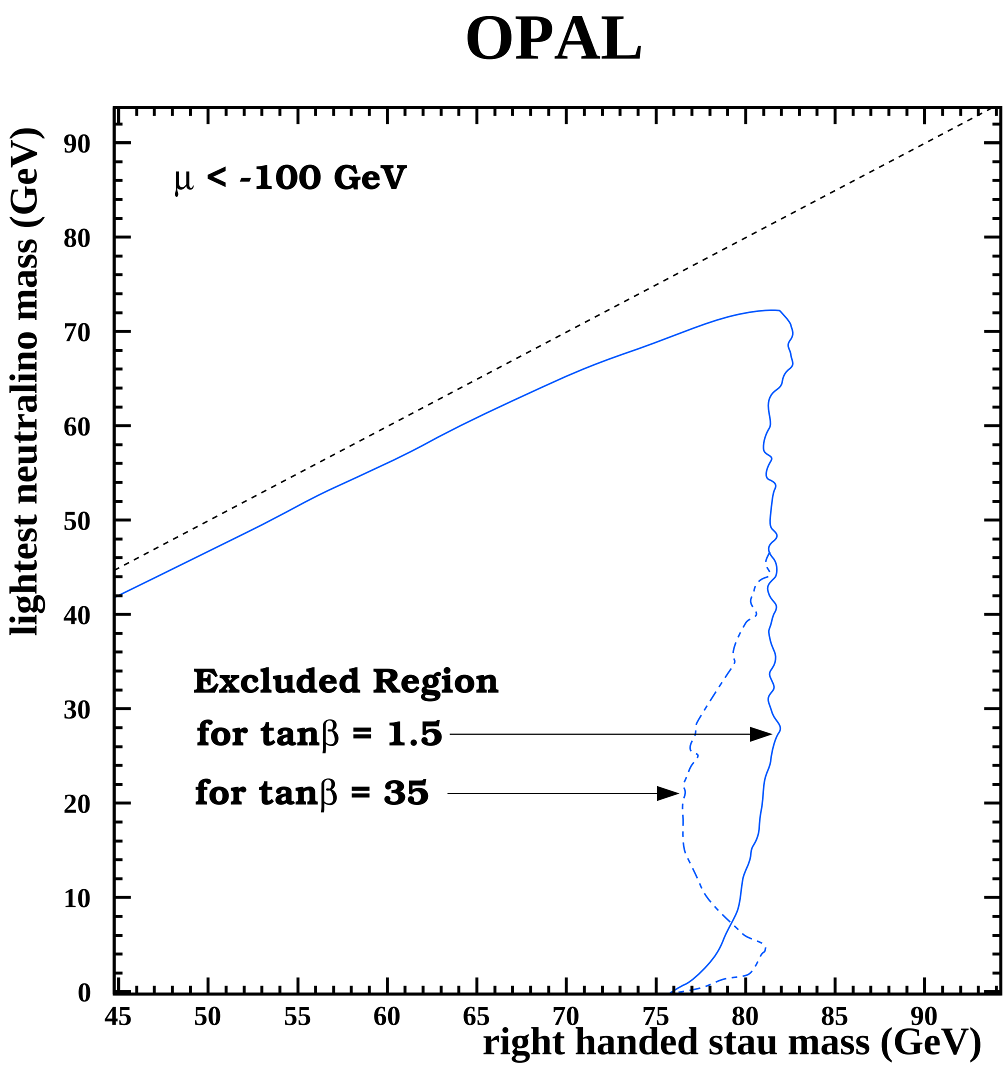

Figure 8.12: *For two values of* $\tan\beta$ *and* $\mu < -100$ *GeV, 95% CL exclusion regions for right-handed stau pairs within the MSSM, obtained by combining the* $\sqrt{s} = 183$ *and 189 GeV data-sets. The excluded regions are calculated taking into account the predicted branching ratio for* $\tilde{\tau}_R^{\pm} \to \tau^{\pm}\tilde{\chi}_1^0$*. The gauge unification relation,* $M_1 = \frac{5}{3}\tan^2\theta_W M_2$*, is assumed in calculating the MSSM branching ratios. The selection efficiency for* $\tilde{\tau}^+\tilde{\tau}^-$ *is calculated for the case that the decay* $\tilde{\tau}^- \to \tau^-\tilde{\chi}_1^0$ *produces unpolarized* $\tau^{\pm}$*. The kinematically allowed region is indicated by the dashed line.*

Chapter 9

Summary and Conclusions

A selection of di-lepton events with significant missing transverse momentum has been performed using a total data sample of 237.4 pb^{-1} at e^+e^- centre-of-mass energies of 183 and 189 GeV. The observed numbers of events, 78 at 183 GeV and 301 at 189 GeV, are consistent with the numbers expected from Standard Model processes, dominantly arising from W^+W^- production with each W decaying leptonically.

Further discrimination techniques have been employed to search for the pair production of charged scalar leptons, leptonically decaying charged Higgs bosons and charginos that decay to produce a charged lepton and invisible particles. No evidence for new phenomena is apparent and model independent limits on the production cross-section times branching ratio squared for each new physics process are presented.

The following limits have been set at 95% CL on the masses of charged scalar leptons and charged Higgs bosons:

- $m_{\tilde{e}^-} > 87.1$ GeV, for $m_{\tilde{e}^-} - m_{\tilde{\chi}_1^0} > 5$ GeV, within the framework of the MSSM, for $\mu < -100$ GeV and $\tan\beta = 1.5$.
- $m_{\tilde{\mu}^-} > 82.3$ GeV, for $m_{\tilde{\mu}^-} - m_{\tilde{\chi}_1^0} > 3$ GeV, for a 100% branching ratio for

the decay ($\tilde{\mu} \to \mu\tilde{\chi}_1^0$).

- $m_{\tilde{\tau}^-} >$ 81.0 GeV, for $m_{\tilde{\tau}^-} - m_{\tilde{\chi}_1^0} > 8$ GeV, for a 100% branching ratio for the decay ($\tilde{\tau} \to \tau\tilde{\chi}_1^0$).

- $m_{\mathrm{H}^+} > 82.8$ GeV, for a 100% branching ratio for the decay $\mathrm{H}^\pm \to \tau^\pm\nu_\tau$.

The results presented in this thesis have been published by OPAL in [46]. The results of the cut based analysis applied by the author to the data taken at 161, 172 and 183 GeV have been previously published in [50]. The author also made a significant contribution to the analysis of the data taken in 1996 at 161 at 172 GeV, published in [49]. In the publication preceding this [57], the excluded masses for sleptons were presented as follows: $m_{\tilde{\mathrm{e}}^-} > 67$ GeV, for $m_{\tilde{\mathrm{e}}^-} - m_{\tilde{\chi}_1^0} > 19$ GeV, for $\mu < -100$ GeV and $\tan\beta = 1.5$; $m_{\tilde{\mu}^-} > 49$ GeV, for $m_{\tilde{\mu}^-} - m_{\tilde{\chi}_1^0} > 4$ GeV, for a 100% branching ratio for the decay ($\tilde{\mu} \to \mu\tilde{\chi}_1^0$). No improvement over the LEP1 limit for staus was obtained. The increased integrated luminosity of high energy data and the improved sensitivity of the analysis as described in this thesis have together resulted in the significant increase in the range of excluded masses for sleptons. The limits on slepton masses presented here are currently the most stringent for any single experiment worldwide. Searches for sleptons at LEP2 using this topology have been presented also by the other LEP collaborations [58]. The combined limits from the four LEP experiments form the strongest limits on slepton masses currently available.

The results of the cut based analysis for charged Higgs bosons have been used by the OPAL collaboration as input to a general search for $\mathrm{H}^+\mathrm{H}^-$ that sets limits on the mass of the charged Higgs boson independent of the branching ratio for the decay $\mathrm{H}^\pm \to \tau^\pm\nu_\tau$, presented in [59].

The upper limits on $\sigma.BR^2$ for sleptons are relevant to interpreting the results of searches for chargino and neutralino production, presented in [60]. Here, regions of the parameter space of the constrained MSSM (CMSSM) [20, 21] excluded by chargino and neutralino searches are presented. The slepton results are used in conjunction with limits on the sneutrino mass [61] to reduce this parameter space by excluding values of the CMSSM parameter m_0 [1]. In addition, in determining whether or not a point in the parameter space is excluded, the upper limits on $\sigma.BR^2$ for the production of charginos undergoing two-body decay, $\tilde{\chi}_1^{\pm} \rightarrow \ell^{\pm}\tilde{\nu}_{\ell}$, as presented in this thesis, are used if $m_{\tilde{\nu}} \leq m_{\tilde{\chi}_1^{\pm}}$ for that point, in which case the decay $\tilde{\chi}_1^{\pm} \rightarrow \ell^{\pm}\tilde{\nu}_{\ell}$ is dominant.

[1] The CMSSM assumes a universal scalar mass at the Planck scale, of value m_0.

Appendix A

Alternative Cut Based Analysis

An alternative approach to the extended maximum likelihood technique described in Chapter 7 to calculate cross-section limits for new particle production is a cut based analysis. A cut is applied on L_R and the resulting efficiencies, expected backgrounds and numbers of observed candidates at each centre-of-mass energy are used as input to the limit calculation. For reasons discussed in Section 7.1, the limits calculated using this method are not as stringent as those calculated using the likelihood technique, but the procedure for determining the cut values is described here because the method provides a useful cross-check of the more powerful method described in Chapter 7, and because the numbers of events passing a cut on L_R provide a direct comparison between the observed data and the Standard Model.

A.1 Optimization of the Cut Values

The value of the cut on L_R, for a given centre-of-mass energy and at a particular point in m and Δm, is chosen such that the expected upper limit on the cross-section times branching ratio squared at 95% confidence, $\langle\sigma_{95}\rangle$, calculated using

Monte Carlo only, is minimized. $\langle\sigma_{95}\rangle$ is given by:

$$\langle\sigma_{95}\rangle = \frac{\langle N^{95}\rangle}{\epsilon\mathcal{L}}, \tag{A.1}$$

where ϵ is the selection efficiency, $\mathcal{L}$ is the integrated luminosity at that centre-of-mass energy and $\langle N^{95}\rangle$ is the expectation value on the upper limit on the number of signal events at 95% CL, N^{95}, given by:

$$\langle N^{95}\rangle \; = \sum_{N=0}^{\infty} P(N,\mu_B) N^{95}(N,\mu_B), \tag{A.2}$$

where $P(N,\mu_B)$ is the Poisson probability of observing N events when μ_B events are expected, $P(N,\mu_B) = \mu^N e^{-\mu}/N!$, and $N^{95}(N,\mu_B)$ is calculated using the method advocated by the PDG [62], in which N^{95} is given by:

$$0.95 = 1 - \frac{\sum_{I=0}^{N} P(I,\mu_B + N^{95})}{\sum_{I=0}^{N} P(I,\mu_B)}. \tag{A.3}$$

The cut values are optimized independently for all m and Δm for which signal Monte Carlo has been generated, and at each centre-of-mass energy, using signal and Standard Model Monte Carlo. The cut values at each centre-of-mass energy are then parameterized as third order polynomial functions of m and Δm.

A.2 Selection Efficiencies, Numbers of Candidates and Expected Backgrounds

Table A.1 gives the selection efficiencies, the numbers of selected events and the numbers of events expected from Standard Model processes at $\sqrt{s} = 189$ GeV for a number of values of m and Δm in the search for $\tilde{e}^+\tilde{e}^-$ production. Tables A.2, A.3, A.4, A.5 and A.6 show the same information for smuons, staus, charginos with two-body decay, charginos with three-body decay and charged Higgs bosons, respectively. The Monte Carlo statistical errors are given.

A.3 Limit Calculation

The parameterized cuts can be used to calculate the number of candidates and the expected background passing the cut for any value of m and Δm. The selection efficiency at any point is found by 2-dimensional linear interpolation. The value of σ_{95} at a given point in m and Δm, found by combining the information at $\sqrt{s} = 183$ GeV and $\sqrt{s} = 189$ GeV is calculated using the likelihood ratio method [63]. The results are consistent with those given in Section 8.2.

Δm (GeV)	$m_{\tilde{e}^-}$ (GeV) 45	55	65	75	85	94
selection efficiency (%)						
2	12.6±1.0	10.1±1.0	7.4±0.8	3.9±0.6	1.3±0.4	0.2±0.1
2.5	24.0±1.4	20.6±1.3	21.6±1.3	18.2±1.2	12.6±1.0	7.1±0.8
5	52.3±1.6	55.7±1.6	56.0±1.6	57.8±1.6	58.5±1.6	54.3±1.6
10	57.3±1.6	63.1±1.5	65.5±1.5	70.3±1.4	72.3±1.4	72.7±1.4
20	48.4±1.6	56.8±1.6	63.3±1.5	68.4±1.5	68.3±1.5	75.6±1.4
$m/2$	48.7±1.6	54.0±1.6	64.6±1.5	64.6±1.5	65.0±1.5	67.7±1.5
m-20	50.7±1.6	58.0±1.6	68.7±1.5	70.0±1.4	67.6±1.5	58.0±1.6
m-10	57.1±1.6	60.6±1.5	72.8±1.4	69.8±1.5	67.4±1.5	59.0±1.6
m	52.1±1.6	56.1±1.6	67.2±1.5	65.9±1.5	67.8±1.5	70.6±1.4
number of selected events						
2	0	0	0	0	0	0
2.5	0	0	0	0	0	0
5	3	1	0	0	0	0
10	9	3	3	1	0	0
20	10	7	6	6	5	1
$m/2$	19	16	17	9	4	0
m-20	18	24	36	34	15	0
m-10	30	33	41	32	20	1
m	28	22	30	26	15	3
number of events expected from Standard Model processes						
2	1.4± 0.5	1.3± 0.5	1.1± 0.4	0.7± 0.3	0.4± 0.3	0.2± 0.2
2.5	1.5± 0.5	1.4± 0.5	1.2± 0.4	1.1± 0.4	0.5± 0.3	0.4± 0.3
5	2.3± 0.5	2.2± 0.5	2.3± 0.6	1.5± 0.5	1.0± 0.4	0.4± 0.2
10	4.3± 0.3	2.6± 0.2	1.4± 0.3	1.3± 0.3	1.1± 0.3	0.4± 0.1
20	10.4± 0.4	6.8± 0.3	5.0± 0.2	3.1± 0.2	1.3± 0.1	0.3± 0.1
$m/2$	13.0± 0.4	13.9± 0.4	15.6± 0.4	14.0± 0.4	10.2± 0.3	1.6± 0.1
m-20	15.2± 0.4	22.2± 0.5	33.0± 0.5	32.9± 0.6	19.2± 0.4	1.8± 0.1
m-10	26.8± 0.5	30.4± 0.5	39.5± 0.6	32.1± 0.5	20.6± 0.4	2.2± 0.1
m	24.6± 0.5	25.7± 0.5	33.9± 0.6	28.7± 0.5	19.4± 0.4	3.3± 0.2

Table A.1: *Selection efficiency, number of selected events and number of events expected from Standard Model processes in the search for* $\tilde{e}^+\tilde{e}^-$ *production at* $\sqrt{s}$ = *189 GeV for different values of* $m_{\tilde{e}^-}$ *and* Δm.

Δm (GeV)	$m_{\tilde{\mu}^-}$ (GeV) 45	55	65	75	85	94
selection efficiency (%)						
2	14.7±1.1	14.0±1.1	9.5±0.9	6.2±0.8	0.7±0.3	0.0±0.0
2.5	26.5±1.4	27.3±1.4	24.7±1.4	20.9±1.3	14.1±1.1	8.0±0.9
5	55.7±1.6	58.6±1.6	59.1±1.6	59.3±1.6	59.5±1.6	57.1±1.6
10	69.7±1.5	70.7±1.4	70.2±1.4	72.9±1.4	74.2±1.4	72.4±1.4
20	61.1±1.5	66.5±1.5	66.2±1.5	67.6±1.5	72.0±1.4	76.8±1.3
$m/2$	60.4±1.5	58.9±1.6	56.7±1.6	58.3±1.6	62.0±1.5	70.0±1.4
m-20	60.7±1.5	59.7±1.6	58.0±1.6	59.4±1.6	57.1±1.6	52.3±1.6
m-10	62.7±1.5	61.1±1.5	57.7±1.6	58.3±1.6	55.9±1.6	50.5±1.6
m	58.2±1.6	51.4±1.6	51.5±1.6	54.9±1.6	57.3±1.6	63.1±1.5
number of selected events						
2	1	1	1	1	0	0
2.5	1	1	1	1	0	0
5	2	2	2	1	1	0
10	4	2	0	0	0	0
20	6	4	3	4	2	0
$m/2$	7	11	11	9	6	3
m-20	10	14	13	16	5	1
m-10	13	14	14	13	4	1
m	11	13	11	7	6	1
number of events expected from Standard Model processes						
2	0.8± 0.3	0.5± 0.3	0.5± 0.3	0.5± 0.3	0.4± 0.3	0.0± 0.0
2.5	0.9± 0.3	0.8± 0.3	0.6± 0.3	0.6± 0.3	0.4± 0.3	0.2± 0.2
5	1.6± 0.4	1.4± 0.4	1.3± 0.4	0.6± 0.2	0.4± 0.2	0.1± 0.0
10	2.2± 0.2	1.3± 0.1	0.7± 0.1	0.5± 0.1	0.5± 0.1	0.2± 0.0
20	6.3± 0.2	4.6± 0.2	3.2± 0.2	2.0± 0.1	1.0± 0.1	0.2± 0.0
$m/2$	6.8± 0.3	6.9± 0.3	7.1± 0.3	7.4± 0.3	6.7± 0.2	1.9± 0.1
m-20	7.4± 0.3	8.4± 0.3	9.5± 0.3	11.0± 0.3	8.3± 0.3	1.1± 0.1
m-10	8.9± 0.3	8.8± 0.3	9.4± 0.3	10.4± 0.3	7.4± 0.3	1.0± 0.1
m	7.2± 0.3	5.9± 0.2	6.6± 0.2	8.7± 0.3	7.8± 0.3	2.3± 0.1

Table A.2: *Selection efficiency, number of selected events and number of events expected from Standard Model processes in the search for $\tilde{\mu}^+\tilde{\mu}^-$ production at $\sqrt{s}$ = 189 GeV for different values of $m_{\tilde{\mu}^-}$ and Δm.*

Δm	$m_{\tilde{\tau}^-}$ (GeV)					
(GeV)	45	55	65	75	85	94
selection efficiency (%)						
2	0.2±0.0	0.1±0.0	0.1±0.0	0.0±0.0	0.0±0.0	0.0±0.0
2.5	0.7±0.1	0.5±0.1	0.3±0.0	0.3±0.0	0.0±0.0	0.0±0.0
5	14.6±0.3	13.4±0.3	12.7±0.3	11.4±0.3	10.2±0.3	9.0±0.3
10	32.6±0.4	34.2±0.4	35.3±0.4	35.5±0.4	37.0±0.4	37.1±0.4
20	42.6±0.4	45.4±0.4	46.6±0.4	48.4±0.4	50.2±0.4	55.2±0.4
$m/2$	43.1±0.4	45.9±0.4	48.6±0.4	49.6±0.4	51.4±0.4	54.2±0.4
m-20	43.5±0.4	47.9±0.4	49.3±0.4	49.0±0.4	51.1±0.4	52.5±0.4
m-10	45.1±0.4	47.3±0.4	48.6±0.4	49.4±0.4	50.1±0.4	53.9±0.4
m	45.6±0.4	47.5±0.4	47.6±0.4	47.3±0.4	48.2±0.4	51.3±0.4
number of selected events						
2	2	3	2	0	0	0
2.5	3	2	1	1	1	0
5	3	3	3	3	4	3
10	8	8	6	5	4	4
20	18	17	15	13	9	8
$m/2$	20	21	21	19	21	21
m-20	21	26	29	31	30	23
m-10	30	31	33	32	28	25
m	31	32	33	30	29	21
number of events expected from Standard Model processes						
2	1.8± 0.5	0.6± 0.2	0.6± 0.2	0.1± 0.0	0.0± 0.0	0.0± 0.0
2.5	2.6± 0.6	2.3± 0.5	1.5± 0.5	1.3± 0.4	0.6± 0.3	0.0± 0.0
5	4.1± 0.6	3.9± 0.7	3.9± 0.7	3.2± 0.6	2.4± 0.6	1.7± 0.5
10	8.4± 0.7	7.7± 0.7	6.9± 0.8	6.2± 0.8	5.4± 0.8	4.6± 0.7
20	15.8± 0.8	14.2± 0.8	13.1± 0.8	11.2± 0.8	9.7± 0.8	8.6± 0.8
$m/2$	17.8± 0.8	19.4± 0.8	20.0± 0.8	19.3± 0.8	18.0± 0.7	18.2± 0.7
m-20	19.0± 0.8	23.6± 0.9	25.2± 0.8	25.3± 0.8	24.9± 0.6	25.8± 0.6
m-10	25.1± 0.9	27.0± 0.9	28.7± 0.9	27.0± 0.7	26.2± 0.7	26.8± 0.7
m	27.7± 0.9	28.2± 0.9	26.8± 0.8	25.4± 0.7	24.0± 0.6	25.2± 0.6

Table A.3: *Selection efficiency, number of selected events and number of events expected from Standard Model processes in the search for $\tilde{\tau}^+\tilde{\tau}^-$ production at $\sqrt{s}$ = 189 GeV for different values of $m_{\tilde{\tau}^-}$ and Δm.*

Δm (GeV)	$m_{\tilde{\chi}_1^\pm}$ (GeV) 50	60	70	80	90	94
selection efficiency (%)						
2	7.5±0.4	6.4±0.4	4.8±0.3	2.2±0.2	0.4±0.1	0.0±0.0
3	21.0±0.6	21.1±0.6	20.2±0.6	19.1±0.6	15.7±0.6	13.2±0.5
4	32.6±0.7	32.8±0.7	33.0±0.7	33.0±0.7	31.4±0.7	32.5±0.7
5	38.9±0.8	41.9±0.8	41.6±0.8	41.4±0.8	42.5±0.8	44.1±0.8
10	52.7±0.8	56.2±0.8	54.7±0.8	58.6±0.8	60.0±0.8	62.1±0.8
20	–	57.0±0.8	60.6±0.8	62.5±0.8	56.9±0.8	64.2±0.8
$(m-15)/2$	–	48.9±0.8	62.7±0.8	66.0±0.7	65.9±0.7	60.9±0.8
m-35	54.4±0.8	54.4±0.8	63.6±0.8	71.9±0.7	63.7±0.8	53.3±0.8
number of selected events						
2	2	2	1	1	1	1
3	2	2	2	2	0	0
4	4	3	3	3	3	1
5	5	4	4	3	3	3
10	15	11	6	4	4	4
20	–	36	29	18	8	4
$(m-15)/2$	–	45	56	55	33	10
m-35	29	53	88	119	52	8
number of events expected from Standard Model processes						
2	2.6± 0.6	2.1± 0.5	1.0± 0.4	1.1± 0.4	1.3± 0.5	1.1± 0.4
3	3.1± 0.6	2.8± 0.6	1.8± 0.5	2.0± 0.5	1.0± 0.4	0.8± 0.3
4	4.5± 0.7	3.6± 0.6	3.0± 0.6	2.3± 0.6	1.8± 0.5	1.4± 0.5
5	5.5± 0.7	4.7± 0.7	4.0± 0.7	3.4± 0.6	2.1± 0.5	1.9± 0.5
10	13.6± 0.7	8.4± 0.6	5.5± 0.5	4.9± 0.5	4.0± 0.5	2.9± 0.5
20	–	36.7± 0.8	26.4± 0.6	16.1± 0.4	4.2± 0.2	2.2± 0.1
$(m-15)/2$	–	45.3± 0.8	56.0± 0.8	60.8± 0.8	41.9± 0.6	13.6± 0.4
m-35	28.6± 0.8	53.3± 0.8	98.5± 1.0	133.0± 1.1	74.7± 0.8	17.6± 0.4

Table A.4: *Selection efficiency, number of selected events and number of events expected from Standard Model processes in the search for $\tilde{\chi}_1^+\tilde{\chi}_1^-$ (2-body decays) at $\sqrt{s}$ = 189 GeV for different values of $m_{\tilde{\chi}_1^\pm}$ and Δm.*

Δm (GeV)	$m_{\tilde{\chi}_1^\pm}$ (GeV) 50	60	70	80	90	94
selection efficiency (%)						
3	3.6±0.3	3.0±0.3	2.5±0.2	1.0±0.2	0.2±0.1	0.2±0.1
5	16.6±0.6	15.8±0.6	14.8±0.6	13.1±0.5	11.3±0.5	10.7±0.5
10	36.3±0.8	38.1±0.8	38.7±0.8	39.9±0.8	39.5±0.8	40.5±0.8
20	44.0±0.8	47.8±0.8	50.9±0.8	50.6±0.8	55.5±0.8	58.3±0.8
$m/2$	42.0±0.8	43.4±0.8	46.3±0.8	52.5±0.8	58.2±0.8	61.8±0.8
m-20	40.3±0.8	41.3±0.8	49.6±0.8	54.4±0.8	61.3±0.8	65.3±0.8
m-10	40.0±0.8	44.4±0.8	51.3±0.8	57.6±0.8	63.3±0.8	62.8±0.8
m	42.9±0.8	50.4±0.8	57.7±0.8	63.2±0.8	69.3±0.7	68.6±0.7
number of selected events						
3	1	2	1	1	0	1
5	2	2	2	1	1	2
10	6	6	5	4	4	3
20	15	12	10	7	6	5
$m/2$	18	18	19	19	21	19
m-20	20	24	35	42	44	44
m-10	28	37	53	65	68	40
m	42	60	86	110	100	51
number of events expected from Standard Model processes						
3	2.4± 0.6	2.1± 0.5	1.7± 0.5	1.4± 0.5	0.5± 0.3	0.5± 0.3
5	4.2± 0.7	3.1± 0.6	2.6± 0.6	1.9± 0.5	1.5± 0.5	1.4± 0.5
10	6.8± 0.7	5.4± 0.7	5.1± 0.7	4.6± 0.7	3.8± 0.7	3.4± 0.7
20	13.6± 0.8	10.6± 0.7	8.7± 0.7	7.0± 0.7	5.8± 0.6	5.2± 0.6
$m/2$	15.5± 0.7	15.1± 0.7	15.5± 0.6	16.2± 0.6	16.6± 0.5	18.1± 0.5
m-20	17.3± 0.7	22.5± 0.7	31.2± 0.8	40.3± 0.7	49.5± 0.7	52.6± 0.7
m-10	25.5± 0.8	35.4± 0.8	51.6± 0.9	65.0± 0.9	80.0± 0.9	55.7± 0.7
m	40.6± 0.9	60.1± 1.0	89.8± 1.1	122.7± 1.1	117.4± 1.1	67.3± 0.8

Table A.5: *Selection efficiency, number of selected events and number of events expected from Standard Model processes in the search for* $\tilde{\chi}_1^+\tilde{\chi}_1^-$ *(3-body decays) at* $\sqrt{s}$ *= 189 GeV for different values of* $m_{\tilde{\chi}_1^\pm}$ *and* Δm*.*

m_{H^+} (GeV)					
45	55	65	75	85	94
selection efficiency (%)					
46.5±0.8	50.8±0.8	49.9±0.8	48.2±0.8	46.7±0.8	48.5±0.8
number of selected events					
34	34	35	30	22	22
number of events expected from Standard Model processes					
29.0± 0.9	30.9± 0.9	29.7± 0.8	26.7± 0.8	22.6± 0.6	20.7± 0.6

Table A.6: *Selection efficiency, number of selected events and number of events expected from Standard Model processes in the search for* $\mathrm{H}^+\mathrm{H}^-$ *production at* $\sqrt{s}$ *= 189 GeV for different values of* m_{H^+}.

Appendix B

Interpolation of the Reference Histograms

B.1 Interpolation in One Dimension

To construct histogram H at mass m, by an interpolation between smoothed single peaked histograms H_1 and H_2 at masses m_1 and m_2, the following steps are performed:

1. Calculate
$$q = q_1 + (q_2 - q_1)\frac{m}{m_2 - m_1}, \tag{B.1}$$
where q_1 and q_2 are the contents of the first non-zero bin of histograms H_1 and H_2, respectively.

2. Subtract q from both H_1 and H_2, from the left, as represented by the shaded areas in Figure B.1.

3. Calculate
$$x = x_1 + (x_2 - x_1)\frac{m}{m_2 - m_1}, \tag{B.2}$$

where x_1 and x_2 are the mean positions of the events removed in step 2 from histograms H_1 and H_2, respectively.

4. Add amount q to the two bins of histogram H that are nearest to position x, sharing between the two bins according to the proximity of x to the bin edge separating them.

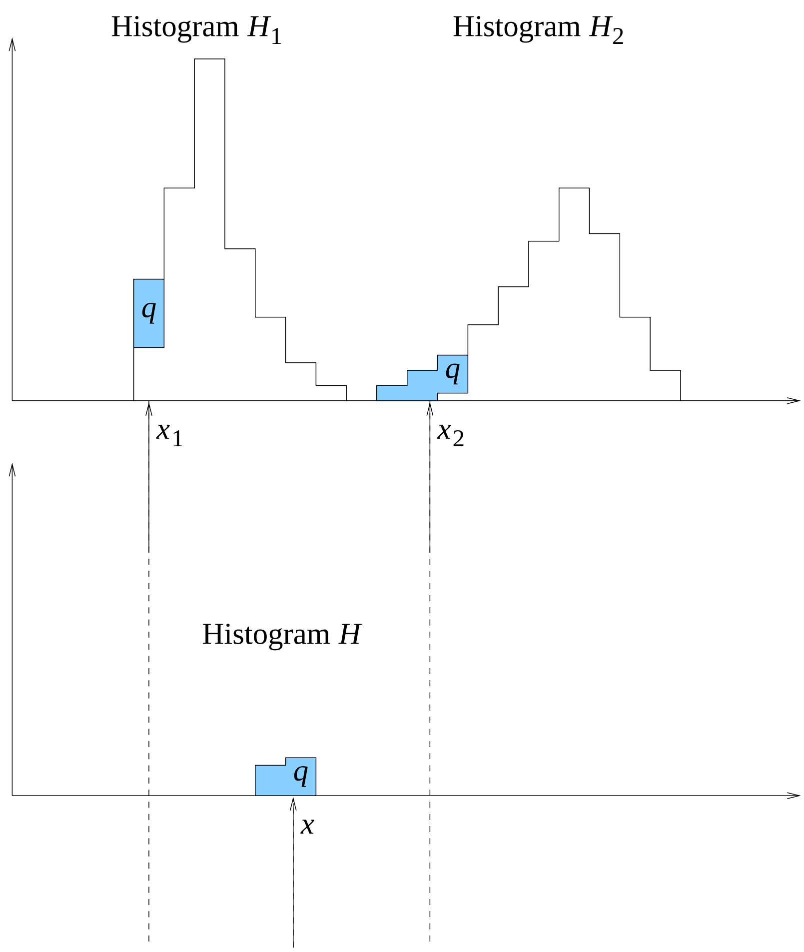

Figure B.1: *Interpolation of the reference histograms.*

Steps 1 to 4 are repeated until histograms H_1 and H_2 are empty.

B.2 Interpolation in Two Dimensions

The two dimensional interpolation is done by performing three consecutive one-dimensional interpolations (two in m followed by one in Δm) as illustrated in Figure B.2.

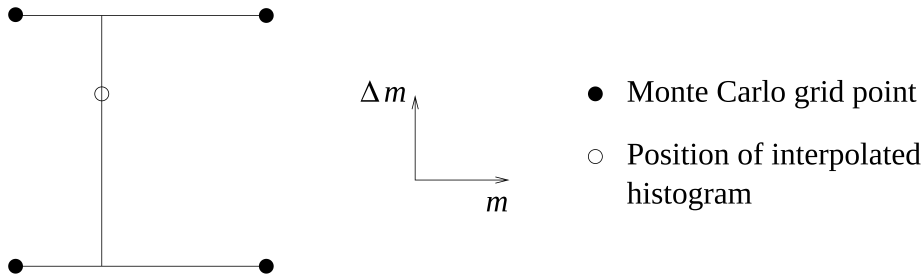

Figure B.2: *Illustration of 2-dimensional interpolation.*

Appendix C

Simulation of Signal Monte Carlo at intermediate values of m and Δm

Signal Monte Carlo at an arbitrary point (m, Δm), required for the construction of the signal L_R distribution for that point, is simulated using the signal Monte Carlo events at the nearest Monte Carlo grid point, (m_1, Δm_1). For each signal Monte Carlo event at (m_1, Δm_1), the fraction, F_i, of each likelihood variable reference histogram at (m_1, Δm_1), which lies below the value of the variable, x_i, is found (Figure C.1). The simulated event at (m, Δm) is assigned a value for each variable, x'_i, such that the fraction of the interpolated reference histogram at (m, Δm) which lies below x'_i is equal to F_i.

Using real Monte Carlo events to construct the simulated Monte Carlo events allows the correlations between the different variables to be taken approximately into account. This would not be the case for an alternative method in which the values of each likelihood variable are generated randomly according to the distribution defined by the interpolated reference histogram for that variable.

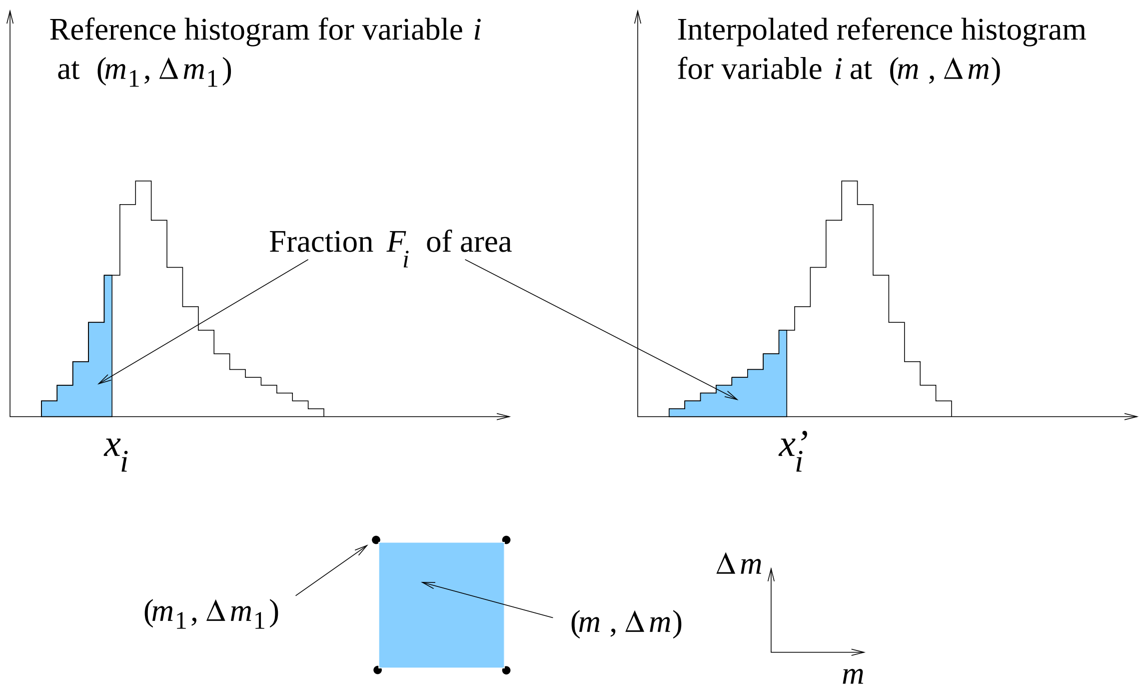

Figure C.1: *Simulation of signal Monte Carlo at arbitrary* m *and* Δm.

Bibliography

[1] S. Myers and E. Picasso, Contemp. Phys. **31** (1990) 387;
W. Schnell, IEEE Trans. Nucl. Sci. **26** (1979) 3130.

[2] ALEPH Collaboration, Nucl. Inst. Meth. **A294** (1990) 127.

[3] DEPHI Collaboration, Nucl. Inst. Meth. **A303** (1991) 233.

[4] L3 Collaboration, Nucl. Inst. Meth. **A289** (1990) 35.

[5] OPAL Collab., K. Ahmet *et al.*, Nucl. Instr. Meth. **A305** (1991) 275.

[6] P. P. Allport *et al.*, Nucl. Instr. Meth. **A386** (1997) 23;
P. P. Allport *et al.*, Nucl. Instr. Meth. **A346** (1994) 476;
P. P. Allport *et al.*, Nucl. Instr. Meth. **A324** (1993) 34.

[7] G. Aguillion *et al.*, Nucl. Instr. Meth. **A417** (1998) 266.

[8] M. Arignon *et al.*, Nucl. Instr. Meth. **A313** (1992) 103.

[9] C. Hawkes *et al.*, "*ROPE User Guide (version 4.09)*", OPAL Offline Note OFFL-0487 (1995).

[10] J. Allison *et al.*, Nucl. Instr. Meth. **A317** (1992) 47.

[11] J. Allison *et al.*, Nucl. Instr. Meth. **A294** (1990) 431.

[12] For example, F. Halzen and A.D. Martin, "*Quarks and Leptons*", John Wiley and Sons (1984);

I.J.R. Aitchison and A.J.G. Hey, "*Gauge Theories in Particle Physics*", IOP Publishing (1989).

[13] ALEPH, DELPHI, L3 and OPAL Collaborations, "*Searches for Higgs Bosons: Preliminary combined results from the four LEP experiments at* $\sqrt{s}$ *= 189 GeV*", submitted to the international Europhysics Conference on High Energy Physics, Tampere, Finland (1999), available at http://www.cern.ch/LEPHIGGS/papers/tampere.

[14] J. Ellis, "*Beyond the Standard Model for Hillwalkers*", hep-ph/9812235 (1998).

[15] The Super-Kamiokande Collab., Phys. Rev. Lett. **81** (1998) 1562.

[16] C. Caso *et al.*, Eur. Phys. J. **C3**. (1998) 125;

G. Jungman, M. Kamionkowski, K. Griest, Phys. Rep. **267** (1996) 195.

[17] M. Drees, "*An Introduction to Supersymmetry*", hep-ph/9611409 (1996).

[18] S.P. Martin, "*A supersymmetry Primer*"hep-ph/9709356 (1997).

[19] S. Coleman and J. Mandula, Phys. Rev. **159** (1967) 1251;

R. Haag, J.T. Lopuszanski and M. Sohnius, Nucl. Phys. **B88** (1975) 257.

[20] H.P. Nilles, Phys. Rep. **110** (1984) 1.

[21] H.E. Haber and G.L. Kane, Phys. Rep. **117** (1985).

[22] S. Deser and B. Zumino, Phys. Rev. Lett. **38** (1977) 1433.

[23] H. Dreiner, "*An Introduction to Explicit R-parity Violation*", in "*Perspectives on Supersymmetry*", edited by G.L. Kane (1997) 462, hep-ph/9707435.

[24] P. Fayet, Phys. Lett. **B69** (1977) 489;

G. Farrar and P. Fayet, Phys. Lett. **B76** (1978) 575.

[25] M.B. Green, J.S. Schwarz and E. Witten, "*Superstring Theory*", Cambridge University Press (1987).

[26] For example, P. Langacker, Phys. Rep. **72** (1981) 185.

[27] H. Georgi, H. Quinn and S. Weinberg, Phys. Rev. Lett. **33** (1974) 451.

[28] S. Dimopoulos and H. Georgi, Nucl. Phys. **B193** (1981) 50.

[29] L.J. Hall, J.Lykken and S. Weinberg, Phys. Lett. **D27** (1983) 2359.

[30] M. Dine *et al.*, Phys. Rev. **D53** (1996) 2658.

[31] S. Dimopoulos and D. Sutter, Nucl. Phys. **B452** (1995) 496.

[32] H.E. Haber and R. Hempfling, Phys. Rev. Lett. **66** (1991) 1815.

[33] *"Review of Particle Properties"*, Phys. Rev. **C3** (1998), 746.

[34] J. Ellis *et al.*, Nucl. Phys. **B238** (1984) 453.

[35] grc4f 1.0 generator: J. Fujimoto *et al.*, Comp. Phys. Comm. **100** (1997) 128; J. Fujimoto *et al.*, in "*Physics at LEP2*", edited by G. Altarelli, T. Sjöstrand and F. Zwirner, CERN 96-01, Vol. 2 (1996) p. 30.

[36] S. Jadach *et al.*, "*Monte Carlo program KORALW 1.42 for All Four-Fermion Final States in* e^+e^- *Collision*", CERN-TH/98-242 (1998).

[37] J.A.M. Vermaseren, Nucl. Phys. **B229** (1983) 347.

[38] Phojet 1.05 generator: E. Budinov *et al.*, in "*Physics at LEP2*", edited by G. Altarelli, T. Sjöstrand and F. Zwirner, CERN 96-01, Vol. 2 (1996) p. 216; R. Engel and J. Ranft, Phys. Rev. **D54** (1996) 4244.

[39] G. Marchesini *et al.*, Comp. Phys. Comm. **67** (1992) 465.

[40] Bhwide generator: S. Jadach, W. Płaczek, B.F.L. Ward, Phys. Lett. **390** (1997) 298.

[41] TEEGG generator: D. Karlen, Nucl. Phys. **B289** (1987) 23.

[42] KORALZ 4.0 generator: S. Jadach, B.F.L. Ward, Z. Wąs, Comp. Phys. Comm. **79** (1994) 503.

[43] PYTHIA 5.721 and JETSET 7.408 generators: T. Sjöstrand, Comp. Phys. Comm. **82** (1994) 74; LU TP 95-20.

[44] NUNUGPV98 generator: G. Montagna, M. Moretti, O. Nicrosini and F. Piccinini, CERN-TH/98-238 (1998).

[45] SUSYGEN generator: S. Katsanevas and S. Melachroinos, in "*Physics at LEP2*", edited by G. Altarelli, T. Sjöstrand and F. Zwirner, CERN 96-01, Vol. 2 (1996) p. 216;
S. Katsanevas and P. Morawitz, Comp. Phys. Comm. **112** (1998) 227.

[46] OPAL Collab., "*Search for Anomalous Production of Acoplanar Di-Lepton Events in* e^+e^- *collisions at* $\sqrt{s}$ *= 183 and 189 GeV*", CERN-EP/99-122 (1999), submitted to Eur. Phys. J. **C**.

[47] DFGT generator: C. Dionisi *et al.*, in *"Physics at LEP2"*, edited by G. Altarelli, T. Sjöstrand and F. Zwirner, CERN 96-01, Vol. 2 (1996) p. 337.

[48] HZHA generator: P. Janot, in *"Physics at LEP2"*, edited by G. Altarelli, T. Sjöstrand and F. Zwirner, CERN 96-01, Vol. 2 (1996) p. 309.

[49] OPAL Collab., K. Ackerstaff *et al.*, Eur. Phys. J. **C4** (1998) 47.

[50] OPAL Collab., "*Search for Acoplanar Lepton Pair Events at* $\sqrt{s}$ *= 161, 172 and 183 GeV*", CERN-EP/98-122 (1998), accepted by Eur. Phys. J. **C**.

[51] J. Allison, Comp. Phys. Comm. **77** (1993) 377.

[52] R.D. Cousins and V.L. Highland, Nucl. Instr. Meth. **A320** (1992) 331.

[53] OPAL Collab., "*Tests of the Standard Model and Constraints on New Physics from Measurements of Fermion-pair Production at 189 GeV at LEP*", CERN-EP/99-097 (1997), accepted by Eur. Phys J. **C**.

[54] OPAL Collab., G. Abbiendi *et al.*, Eur. Phys. J. **C8** (1999) 191.

[55] M.M. Nojiri, Phys. Rev. **D51** (1995) 6281.

[56] *"Review of Particle Properties"*, Phys. Rev. **C3** (1998), 747.

[57] OPAL Collab., K. Ackerstaff *et al.*, Phys. Lett. **B396** (1997) 301-314.

[58] ALEPH Collaboration, R. Barate *et al.*, Phys. Lett. **B433** (1998) 176.
DELPHI Collaboration, P. Abreu *et al.*, Eur. Phys. J. **C6** (1999) 385.
L3 Collaboration, M. Acciarri *et al.*, CERN-EP/99-128, (1999), submitted to Phys. Lett. **B**.

[59] OPAL Collab., G. Abbiendi *et al.*, Eur. Phys. J. **C7** (1999) 407-435

[60] OPAL Collab., G. Abbiendi *et al.*, "*Search for Chargino and Neutralino Production at $\sqrt{s}$ = 189GeV at LEP*", CERN-EP/99-123 (1999), to be submitted to Phys. Lett. **B**.

[61] C. Caso *et al.* (Particle Data Group), Eur. Phys. J. **C3** (1998) 760.

[62] *"Review of Particle Properties"*, Phys. Rev. **D54** (1996), p166 formula 28.40.

[63] A. G. Frodesen, O. Skjeggestad, and H. Tøfte, *"Probability and Statistics in Particle Physics"*, Universitetsforlaget, 1979, ISBN 82-00-01-01906-3;
S.L. Meyer, *"Data Analysis for Scientists and Engineers"*, John Wiley and Sons, 1975, ISBN 0-471-59995-6.